2022

# THE DESIGN AND SYNTHESIS OF NEW ORGANIC DITHIOLS FOR ENVIRONMENTAL APPLICATIONS

Shashika Nadishani Bandara
*University of Kentucky*, shashikanb@gmail.com
Author ORCID Identifier:
🆔 https://orcid.org/0000-0002-4191-4015
Digital Object Identifier: https://doi.org/10.10323/etd.2022.165

STUDENT AGREEMENT:

I represent that my thesis or dissertation and abstract are my original work. Proper attribution has been given to all outside sources. I understand that I am solely responsible for obtaining any needed copyright permissions. I have obtained needed written permission statement(s) from the owner(s) of each third-party copyrighted matter to be included in my work, allowing electronic distribution (if such use is not permitted by the fair use doctrine) which will be submitted to UKnowledge as Additional File.

I hereby grant to The University of Kentucky and its agents the irrevocable, non-exclusive, and royalty-free license to archive and make accessible my work in whole or in part in all forms of media, now or hereafter known. I agree that the document mentioned above may be made available immediately for worldwide access unless an embargo applies.

I retain all other ownership rights to the copyright of my work. I also retain the right to use in future works (such as articles or books) all or part of my work. I understand that I am free to register the copyright to my work.

REVIEW, APPROVAL AND ACCEPTANCE

The document mentioned above has been reviewed and accepted by the student's advisor, on behalf of the advisory committee, and by the Director of Graduate Studies (DGS), on behalf of the program; we verify that this is the final, approved version of the student's thesis including all changes required by the advisory committee. The undersigned agree to abide by the statements above.

<div align="right">

Shashika Nadishani Bandara, Student

Dr. David A. Atwood, Major Professor

Dr. Dong-Sheng Yang, Director of Graduate Studies

</div>

THE DESIGN AND SYNTHESIS OF NEW ORGANIC DITHIOLS FOR
ENVIRONMENTAL APPLICATIONS

_____

DISSERTATION
_____

A dissertation submitted in partial fulfillment of the
requirements for the degree of Doctor of Philosophy in the
College of Arts and Sciences
at the University of Kentucky

By
Shashika Nadishani Bandara
Lexington, Kentucky
Director: Dr. David A. Atwood, Professor of Chemistry
Lexington, Kentucky
2022

THE DESIGN AND SYNTHESIS OF NEW ORGANIC DITHIOLS FOR
ENVIRONMENTAL APPLICATIONS

A thiol molecule, 2,6-pyridinediamidoethanethiol (PB9), was synthesized based on the pyridine-2,6-dicarboxamide scaffold with appended cysteamine groups. PB9 acts as an effective chelator for Pb(II) due to multiple binding sites ($N_3S_2$) through irreversible binding precipitating Pb(II). Removal of aqueous Pb(II) from solution was demonstrated by exploring the effects of time, initial PB9:Pb(II) ratios, pH, exposure time, and solution temperature. After 15 min the Pb(II) concentrations were reduced from 50.00 ppm to 0.30 ppm (99.4%) and 0.25 ppm (99.5%) for PB9:Pb ratios of 1:1 and 2:1, respectively. Removal of >93% Pb(II) was observed over multiple pH values with negligible susceptibility for leaching over time. The thermodynamic studies reveal that the removal of Pb(II) from solution is an entropically driven, spontaneous process. Solution-state (UV−vis, $^1$H-NMR, $^{13}$C- NMR) along with solid-state (IR, Raman, and thermal) studies of PB9/Pb(II) compounds were performed. UV-vis displays a global maximum at 274 nm and a local maximum at 327 nm for ligand-to-metal charge transfer S$^-$ 3p to $Pb^{2+}$ 6p, and intraatomic $Pb^{2+}$ 6s to $Pb^{2+}$ 6p transitions. FT-IR absorption spectra show significant absorption bands corresponding to amide I (C=O stretching) and amide II bands (C-N stretching, NH bending). The spectral shifting due to coordination of the amidic and pyridinic N to Pb(II) and further covalent bonding with sulfur was observed. Probable PB9 + Pb(II) interactions are proposed based on the techniques above mentioned. The molecular structure was designed as PB9 behaving like a bis-deprotonated ligand with an $N_3S_2$ donor set to give Pb(II) a trigonal bipyramidal environment with non-stereochemically active s electrons. The existence of a cyclic oligomeric $(PB9)_4(Pb)_4$ or polymeric $(PB9)_\infty(Pb)_\infty$ structure is evidenced by broad melting point, insolubility in most common solvents, and amorphous powder XRD.

Moreover, PB9 also exhibits high sensitivity and selectivity towards Fe(III) over other metal ions by fluorescent quenching. Theoretical studies comprising Benesi-Hildebrand, and studies such as Job's plot, Stern-Volmer (S-V), and detection limits illustrate higher sensing abilities, possible dynamic and static quenching, and reversibility of binding. The quenching efficiency found by S-V is $7.42 \pm 0.03 \times 10^3$ M$^{-1}$. Job's plot indicates the molar binding ratio of PB9: Fe(III) as 1:1 with a higher apparent association

constant of $9.537 \times 10^3$ M$^{-1}$ from the Benesi- Hildebrand plot. A linear range of Fe(III) (0 – 80 µM) with a detection limit of 0.59 µM (0.003 ppm) was found. The obtained detection limit was much lower than the maximum allowable limit of Fe(III) (0.3 ppm) regulated by EPA in drinking water. PB9-sensor exhibits visible color change from colorless to yellow acting like a naked-eye detector for Fe(III).

In a separate study, 2,2'-(isophthalolybis(azanediyl))bis-3-mercaptopropanoic acid (AB9) was coupled to amine-functionalized silica and silica-coated magnetic nanoparticles (with magnetite, $Fe_3O_4$, core). This exploration was conducted for achieving >15 ppb (EPA level in drinking water) by a previously established method in the lab. The impact of initial concentration, pH, exposure time, and adsorbent dosage on the adsorption properties of Pb(II) from an aqueous solution was studied and optimized. Characterization was performed with ICP, FT-IR, Raman, XRD, TEM, and SEM. Results revealed successful fabrication of AB9 on mesoporous silica and MNP surfaces without introducing crystalline impurities. Indeed, an added advantage for AB9-MNP over AB9-silica is its magnetic nature, whereby a magnet was used to isolate the Pb(II)-containing (solid) composite from the treated water. The > 99.9% removal of Pb(II) was obtained by AB9-MNP with detectable Pb(II) dropping below 15 ppb EPA level. The obtained equilibrium results were inserted in various adsorption isotherm models, including Langmuir, Freundlich, Temkin, and Dubinin-Radushkevich. The data was in agreement with the Langmuir model, suggesting a dominant chemical adsorption mechanism on mesoporous AB9- silica and AB9-MNP with monolayer coverage. Maximum adsorption capacities were 22.05, 24.80, 35.57, and 56.40 mg/g, respectively, for silica, AB9-silica, MNP, and AB9-MNP. This demonstrates that a thiol group improves the adsorption capacity of Pb(II). This is an eco-friendly modification with rapid magnetic separation and chemicals utilizing HSAB to form stable compounds. Lack of complicated operations, extensive reaction times, high temperatures or high pressures, and toxic/ harmful reaction media make these AB9-MNP a good candidate for aqueous Pb(II) removal.

KEYWORDS: Thiol, irreversible binding, quenching, selective, magnetic

Shashika Nadishani Bandara

04/13/2022

THE DESIGN AND SYNTHESIS OF NEW ORGANIC DITHIOLS FOR
ENVIRONMENTAL APPLICATIONS

By

Shashika Nadishani Bandara

David A. Atwood
Director of Dissertation

Dong-Sheng Yang
Director of Graduate Studies

04/13/2022
Date

ACKNOWLEDGMENTS

It is a great pleasure that I acknowledge the several individuals who supported me with immense guidance to complete my Ph. D. research work.

First of all, I express my sincere gratitude for my Ph. D advisor, Dr. David A. Atwood, for his continuous support and motivation. I am forever grateful to him for letting me grow as an independent researcher.

Second of all, I would like to express my sincere gratitude to my Ph.D. dissertation committee members: Dr. John Selegue, Dr. Beth Guiton, and Dr. Chris Matocha for offering encouragement, guidance, suggestions, and corrections and paving the way for the successful completion of my Ph.D. research work. Also Dr. Young-Sam Lee for serving as my outside examiner.

I would like to express heartfelt gratitude to Dr. John Walrod and Dr. Daniel Burriss for all the guidance and support they gave me when I first joined the group. Their guidance was an immense help for me to learn laboratory as well techniques and methods. I also would like to convey my special thanks to current graduate student, Michael Moore, for his continuous help throughout the preparation of this dissertation and for making a friendly laboratory environment.

My most sincere thanks also go out to Dr. Sean Parkin for lending his expertise in X-Ray crystallography, Dr. Jason Unrine, Tonya Morgan, Hopps Shelly, and Megan Combs for providing me with ICP data, and Dali Qian for helping me with SEM, and TEM.

Words cannot express my deepest gratitude to my family members, my lovely husband, my wonderful parents, and my family members. Not only their continued support throughout the Ph.D. process but also provided me with heartfelt affection to overcome lots of ups and downs I had throughout the past few years. Thank you for being with me throughout this tough time.

Last but not least, I am grateful to all my friends and colleagues specially Srilankan friends here in Lexington for making a home away from home.

TABLE OF CONTENTS

LIST OF TABLES

# LIST OF FIGURES

# LIST OF SCHEMES

CHAPTER 1.  INTRODUCTION TO LEAD CHEMISTRY

## 1.1    Statement of purpose

The focus of this dissertation research work was to design, synthesize, and characterize a dithiol ligand, PB9, 2,6-pyridinediamidoethanethiol, which may play an important role in environmental applications. This dithiol molecule binds with Pb(II) in aqueous environments. The resulting precipitate was fully characterized, with a related study of basic chemistry behind the metal compounds that formed.  As Pb(II) is a borderline metal when considering Hard-Soft Acid-Base theory (HSAB), it was hypothesized that the PB9 sulfhydryl functional group covalently binds with a divalent metal cation, thereby allowing effective sequestration of Pb(II) from aqueous samples. PB9 displays a similar reactivity to another dithiol ligand called B9, benzene-1,3-diamidoethanethiol.

In the subsequent work, PB9 was used as a highly sensitive, selective, and naked-eye detector for Fe(III). Theoretical studies comprising Benesi- Hildebrand, Stern- Volmer (S-V), and Job's plot and detection limits were applied to illustrate higher sensing abilities, possible quenching mechanisms, and binding mechanisms. The determination of the detection limit was established for achieving the maximum allowance limit of Fe(III) regulated by EPA in drinking water.

Moreover, the dithiol molecule AB9, 2,2'-(isophthalolybis(azanediyl))bis-3-mercaptopropanoic acid, was coupled to amine-functionalized silica (AB9- silica) and silica-coated magnetic nanoparticles (AB9- MNP having magnetite, $Fe_3O_4$ core). These composites were used in a preliminary study exploration for achieving Pb(II) EPA level in drinking water by a previously established method in the lab.

1

## 1.2    Lead as a Heavy Metal

Heavy metals are naturally occurring elements, having relatively higher atomic weights. They have a density of at least five times greater than that of water. Owing to their high degree of toxicity several elements such as cadmium, lead, arsenic, mercury, and chromium are ranked top-heavy metals which cause severe effects on public health such as cancers. Thus, classified as human carcinogens by the U.S. Environmental Protection Agency (EPA). However, their toxicity depends not only on factors like chemical species, dose, duration of exposure, and route of exposure but also the age, genetics, nutritional status, and gender.[1] [2, 3] Due to these factors lead, mercury, and cadmium were identified as the three toxic metals in the top 10 chemicals of major public health concern by WHO.[4]

Lead is a naturally occurring metal although it is rare. It is a metallic amphoteric (functioning either as an acid or as a base) element commonly found in ore with zinc, silver, and copper. Lead is extremely toxic, especially in its ionic form or as certain compounds. It can enter living systems and compete with important substrates inhibiting the functioning of enzymes. There is no safe limit for lead exposure.

The most common natural form of lead is galena (PbS), but other forms encountered are cerussite ($PbCO_3$) and anglesite ($PbSO_4$). However anthropogenic activities such as mining and fossil fuel burning (airborne lead in smoke from smelters) contribute to higher lead amounts in the environment. As an example, lead has been used for lead-acid batteries for several decades, organic Pb compounds were exposed to the environment thereby humans due to Pb-containing gasoline. It is known that since the 1920s, Pb has been added to gasoline as tetraethyl lead (TEL) which later causes significant exposure through car exhaust.[5, 6]  X-ray shields, and metal products. In 2004, an estimate

of 1.52 million metric tons of lead was used.[2] Also, solders used before 1986 typically contained about 50 percent lead, solders, and flux that are considered "lead-free" can still contain lead (no more than 0.2%). Recent trends in policies such as reducing the lead level in paints and an outright ban on lead in new paints in 1987, pipe solder, ceramic products, and banning lead gasoline in 1996 remarkably reduced the release of lead. Unfortunately, of the 16.4 million homes in the United States, 25% of those still have significant amounts of lead paint. The primary sources of lead in water are by dissolving or particulates of lead service lines, lead solder, and brass fittings which contain a high concentration of lead.[7, 8] Additionally, lead is used in some traditional medicines and cosmetics. Exposure mainly occurs through inhalation of aerosols or dust and ingestion.

This makes lead one of the most pervasive environmental health threats. Lead can enter the human body in different ways oftentimes, lead poisoning shows no symptoms. However, lead affects many vital organs such as the kidney, liver, and soft tissues such as the heart and brain with only the most acute cases of lead poisoning causing death. In addition to these, the nervous system is the most vulnerable target of lead poisoning, leading to headaches, irritability, memory loss, dullness, kidney disease, high blood pressure, and cancer.

The US EPA has set drinking water standards with two levels of protection (EPA 1991, EPA 2000b). Accordingly, the action level (the level for enforcement) and the Maximum Contaminant Level Goal (MCLG)- the level of the contaminant in drinking water below which there is no known or expected risk of health) for lead is 15 ppb (0.015 ppm) and 0.00 mg/L for lead in water. That means no known or anticipated adverse effects on human health occur and would be desirable to consume lead-free water. Despite this,

this economic consideration of USEPA has set an action level of lead in drinking water as 15 ppb (15 g/L) depicting that any utility must ensure that water to the customer does not exceed this level in at least 90 percent of the homes sampled.

### 1.2.1 Lead Current Remediation.

Lead can exist in water in a broad array of forms, where speciation in water explains this. Whilst ample data is available on lead concertation, very little is known about the physical and chemical forms of lead present. This physiochemical speciation is important, as it influences the efficiency of adsorption, distribution, mobility and biological availability depends not only on their concentration but also on the chemical and physical association. Some factors like pH, redox potential, and availability of "reactive species" are the most important.[9] The chemistry of lead is complex due to lead presenting in a monovalent and divalent ion, a complexion, $OH^-$, $O^{2-}$, $CO_3^{2-}$.

Since lead can exist in many forms, a broad array of methods is needed for adequate removal. Nevertheless, there are several technologies to remove lead that has gained a huge attraction among researchers for quite a long time. Dissolved (soluble) lead may be removed by ion exchange, adsorption, distillation, or reverse osmosis.[3, 6, 10-13] On the other hand, insoluble (particulate) lead may be removed by filtration or adsorption. However, there are some drawbacks such as sulfide precipitation involving toxic $H_2S$ gas formation.[14]

### 1.2.2 Chemistry of lead-Sulfur compounds.

As many commercially and commonly available agents do not meet low EPA level guidelines and produce toxic byproducts, there is a clear need to develop new ligands that can effectively bind with lead.

Lead belongs to group 14 in the periodic table, classified as a borderline metal cation according to Hard-Soft-Acid-Base (HSAB) theory. This indicates lead will be coordinated by amino acids, even harder interactions with oxygen, and soft thiol groups. The sulfur atom is nucleophilic, and in the thiol, the typical thiol $pK_a$ is around 10- 11.

The concentration of lead in river water is low under neutral conditions. Moreover, the low solubility of lead in water that contains dissolved $CO_2$ species and neutral pH values generally will remain very low and constant concentration. The median concentration in river and lake water is estimated in the US as 2 µg/L.[15] Lead tends to bind with major anions in water such as carbonate, sulfide, hydroxide, and rarely sulfate.

Lead is only released slowly by weathering processes. Lead in water systems presents complicated by the pH and the redox potential of the water. In addition to this, aquatic toxicity is complicated due to the involvement of interactions between the environment and the metal pollutant. For this reason, one should consider the treatment carefully.  The thiophilic nature of lead allows for binding with thiol molecules allowing their subsequent removal. Therefore, to understand the transport and effects of lead on a given system, its forms and species must be identified. Consideration of total metal concentration will be misleading, as the uncomplexed ions tend to be readily assimilated by organisms. Therefore, the effect of chemical speciation such as chelation, precipitation, adsorption, and complexation (inorganic; carbonates) should be considered. The differing toxicity arises, as the organolead compounds are more toxic than an inorganic compound of lead.[16] Although metallic Pb and mineral lead are nearly insoluble in pure water, they are highly soluble in organic acids.
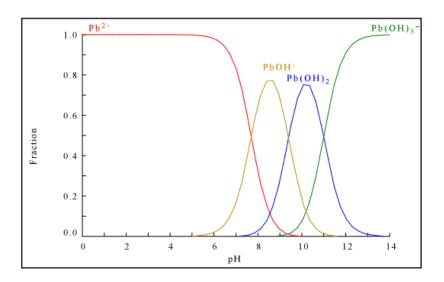
Figure 1-1. Speciation of Pb(II) as a function of pH.

As shown in Figure 1-1, over most of its region, in which water is at 25 °C, and at 1 atm pressure, below a pH of 5.5, the predominant and stable species is $Pb^{2+}$. The $Pb^{+2}$ predominant oxidation state of lead undergoes partial hydrolysis according to equation 1.[17]

$$Pb^{2+} + H_2O \rightarrow Pb(OH)^+ + H^+ \quad pK_a = 7.9 \qquad (1)$$

Several hydroxide complexes, such as $Pb(OH)_2$ and $Pb(OH)^+$ soluble species, can form in aqueous environments. $PbO_2$ on the other hand is stable only in a highly oxidized environment, making $Pb^{4+}$ contribute very little to aqueous geological systems. Between pH of 7 to 12, the predominant culminating species is the $Pb(OH)_2(s)$ sequence appearing due to the formation of $Pb_4(OH)_4^{4+}$, $Pb_6(OH)_8^{4+}$, and $Pb_3(OH)_4^{2+}$.[18]

### 1.2.3 Thiol (B9, AB9, MB9, EB9, and PB9) compounds for Pb(II) removal.

The main group (like lead) thiolates display a large variety of coordination numbers, with geometries displaying a lack of ligand field stabilization energy. Thus, they

6

tend to form polynuclear aggregates of tetrahedral building blocks. Reactivity of lead is largely influenced by the "relativistic effect", which is due to the high speeds of electrons when they are moving near the nucleus. This movement results in the separation of $6s$- $5d$ orbital energies and the stabilization of s orbitals while destabilizing $d$ orbitals.[19, 20]

In the theory, especially in heavier elements having a higher effective nuclear charge, as electron velocity approaches the speed of light, the mass of inner electrons increases substantially. This leads to a relativistic contraction of $s$-orbitals resulting thereby, in increased shielding of the nucleus and expansion of d and $f$-orbitals, as well as $p$-orbitals to a lesser extent.

The inert pair effect is attributed to the relativistic effect and due to this effect, lead in its thiolate complexes is only found as a $Pb^{2+}$ state with the coordination around Pb as tetra, penta, and hexa. Some of the examples are tetra-coordinate $Pb(SCH_2CH_2NH_2)_2$ synthesized using PbO and $[HSCH_2CH_2NH_3]Cl$ and NaOH. Here the presence of intermolecular N-H···S hydrogen bonds was observed. The Pb atom forms two covalent Pb-S bonds and two intramolecular dative Pb···N bonds with a stereochemically active lone pair. There are no intermolecular Pb···Pb contacts, and no molecular symmetry.[21] (Figure 1-2)
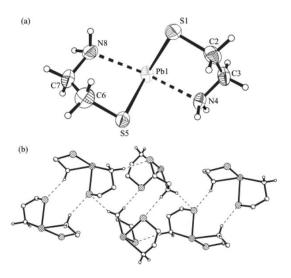
Figure 1-2(a) Crystal structure of $Pb(SCH_2CH_2NH_2)_2$, (b) packing diagram showing N-H…S hydrogen bonds. Reprinted with permission from[21] copyright {2004} American Chemical Society.

$[Pb_2Cl(SCH_2CH_2NH_2)_3]$ is another example of the lead having two different coordination. as four and five-coordinate Pb(II) metal centers (Figure 1-3). The precursors were cysteamine·HCl with $Pb(CH_3COO)_2 \cdot 3H_2O$ in the NaOH medium. The stereochemically active lone pair gives the four-coordinate a distorted square pyramidal geometry, while five-coordinate metal centers have octahedral geometry. [22]
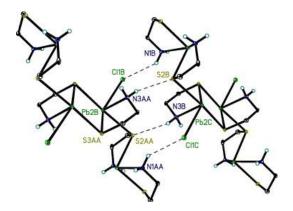


Figure 1-3. Molecular structure of $[Pb_2Cl(SCH_2CH_2NH_2)_3]$.[22]

Lead is a soft Lewis acid and has an affinity toward sulfhydryl groups. This is part of the reason that it binds to the cysteine residues in proteins. Moreover, for decades, bidentate 2- aminothiols are known to have higher affinities towards "soft" and "hard" ions, owing to the presence of sulfhydryl and amine groups respectively.[23, 24] Reagents such as sodium-methylcarbamate SDTC, sodium trithiocarbonate (STC), 2,4,6-trimercaptotriazine (TMT)[25] are used reagents for Pb(II) removal, but they are suffering from their decomposition in the presence of other hazardous materials, and require elevated doses.[13, 25]

Our group has extensively worked on designing and synthesizing various dithiol molecules to explore preferential binding to Pb(II), and related heavy metals. Herein, B9, (N, N'-bis(2-mercaptoethyl)isophthalamide), previous trade names MetX, BDETH$_2$, and BDTH$_2$), AB9 (2,2'-(isophthaloybis(azanediyl))bis-3-mercaptopropanoic acid), MB9, and EB9 are shown in Figure 1-4. It was found that these molecules are stable and do not form disulfide linkages, making them ideal for the covalent bonding to the heavy metal. B9 uses the unique feature of binding with "soft" heavy metals such as lead, cadmium, and mercury in gold mining effluent, lead battery recycling effluent, acid mine drainage, coal refuse, and contaminated soil.[12, 13, 26-30] All molecules were designed to have preferential interactions of the thiol "soft" interactions.
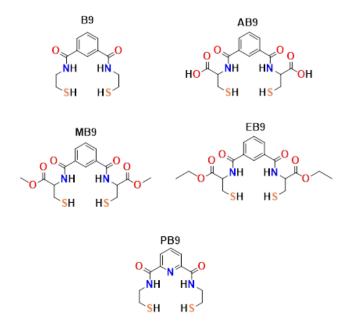
Figure 1-4. Structures of thiol ligands designed, B9, AB9, MB9, EB9, and this work (PB9).

This research work is mainly focused on PB9, which has two cysteamine groups linked to the pyridine core via amide bond formation via the N of the cysteamine. PB9 has been used as an efficient and selective binder for inorganic anions.[31]

PB9 was capable of reacting with heavy metals such as Cu(II) and Cd(II) from aqueous solutions over a wide pH range, without producing secondary byproducts. Cu(II) was reduced by >99.99% starting from 50.00 ppm at pH of 4.5, and 99.88% starting from 50.00 ppm at pH 6.0.[32] The following reaction equation is showing how the reaction takes place when an aqueous salt solution of metal was added to methanolic PB9 solution.

$$C_{11}H_{15}N_3O_2S_2(aq) + M^{2+}(aq) + 2H_2O(l)$$

$$\rightarrow C_{11}H_{13}N_3O_2S_2M(s) + 2H_3O^+(l) \quad (1)$$

M= Cu, Cd, Hg, Ni, Zn, Pb, etc.

The design involves the thiol ligands following Hard-Soft Acid-Base (HSAB) theory which states that hard acids preferentially bond with hard bases and soft acids with soft bases. Thus, small size, higher oxidation state, high electronegativity, low polarizability, low HOMO, or high energy LUMO are characteristics of these hard acids and hard bases, and the reverse is applicable for soft acids and soft bases.[24]

Moreover, in this research study, AB9 was used in solid support via the formation of amine functional groups through the amide/ ester bond formation. 14-Membered ring structures are predicted to be formed by these molecules, however, obtaining an X-ray single-crystal structure is a drawback. However, in subsequent chapters, PB9 and AB9 are used focusing on their synthesis and utilization as sulfhydryl ligands for binding to lead. The following table 1-1 shows the precipitated Pb(II) metal from water with thiol ligands using laboratory stock solutions and industrial effluents using B9. Initial and final concentrations are in ppm.

Table 1-1. Summary for Pb(II) removal from previous syntheses dithiol B9

| Ligand | L: M stoichiometry | Initial conc. (ppm) | pH | Time (h) | Final conc. (ppm), Removal % | Ref. |
|---|---|---|---|---|---|---|
| B9 | 1:1 (source: lab) | 50 | 4 | 1 | 0.10, 99.80% | [12] |
| | | | 4 | 6 | 0.05, 99.90% | |
| | | | 4 | 20 | 0.05, 99.90% | |
| | | | 6 | 1 | 0.31, 99.38% | |
| | | | 6 | 6 | 0.22, 99.56% | |
| | | | 6 | 20 | 0.13, 99.74% | |
| | 1:1 (source: Lead-Battery Acid-Recycling (LBAR) | 3.61 (raw field) | | 15 min | <0.02, 99.4% | [13] |

Below the detection limit for ICP-OES: Pb= 0.02 ppm.

## 1.3 Introduction to Sensors

### 1.3.1 Sensor Classification

Sensors can be classified based on how a physical or chemical property is converted into a quantitative electrical signal.[33] (Figure 1-5)
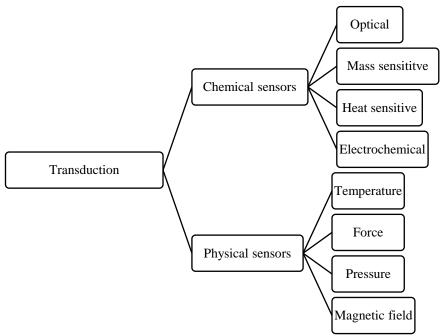


Figure 1-5. General classification of sensors.[34]

A physical sensor measures a physical quantity like temperature, pressure, magnetic field, etc., and converts it into a signal which can be read with the aid of an instrument. Chemical sensors convert a chemical (or physical) property of a specific analyte into a measurable signal.

### 1.3.2 Optical Chemical Sensors.

Research into optical sensors has increased in recent years, as they are found incredibly useful in many applications in biomedical, environmental monitoring, clinical, and process controlling.[35-38] The measured optical property can be absorbance, luminescence, polarization, Raman scattering, and reflectance.[39] Real-time optical sensors provide immediate quantification of an analyte.

An optical sensor consists of a recognition unit. Where a specific interaction and identification of the analyte takes place, a transducer converts the recognition process into a measurable optical signal, an optical device, and a detector that detects and converts, and amplifies the optical property into a readout.

### 1.3.3 Determination of Heavy Metal ions with Chromophores.

Heavy metals are brought to the environment by unprecedented pollution with industrialization and its consumption of energy. Because of the toxicity of these heavy metals, the development of selective and sensitive methods is needed. An ideal metal sensor responds to the presence of heavy metal ions selectively, sensitively, reversibly, and continuously.[40] Most heavy metal sensors use an indicator dye that changes color after metal complexation, following the reaction accompanied by a change of absorbance or fluorescence of the chelates. A commonly used dye is coumarin, functionalized with receptors that are sensitive to different metal ions.[41, 42]

However, many metal sensors cannot be used effectively as they require unfavorable analytical wavelengths, have low molecular absorptivity, poor photostability, and the need for additional reagents. Some of them are bound irreversibly, or only in

14

specific pH ranges making them useless at neutral pH values. Some undergo the appearance of one band along with the disappearance of another band, rather than the intensity change of a single band, these are called two-wavelength indicators.[43]

### 1.3.4   Determination of Heavy Metal ions with Fluorophores.

The fluorescent indicators are often "on" or "off" type. This means that only one of the species, either the complex or the non-complexed species, is fluorescent. Their improved sensitivity is crucial in sensory activity and selectivity. This is due to the low probability that the interfering species would have the same absorbance and emission as the analyte complex.

Fluorimetry is an effective analytical technique that offers a broad variety of spectroscopic techniques such as lifetime measurements, polarization, and energy transfer. Transition metals and heavy metals can be recognized as an important group of indicators based on the quenching of luminescence. In the quenching process, a static and/or dynamic quenching takes place in the ground state by making the non-fluorescent ground state complex. There is no change in the excited state lifetime. Whereas the dynamic "collisional" quenching refers to the interaction between the metal ion (quencher) and the excited state fluorophore and this leads to a reduction in both the emission intensity and lifetime of the excited state.[44] Hence, many transition metals particularly Fe(III), Co(II), and Ni(II) show decreased quenching efficiencies due to their numerous unpaired spins.

### 1.3.5 Fluorescent and Colorimetric Chemosensors for detection of Transition Metal Cations.

Recently, the design and development of molecular sensors to detect transition metal ions have attracted intense attention.[37, 45-47] Among these iron, zinc, copper, nickel, and cobalt have taken special attention because these are essential elements in the environment and biological systems but can cause severe damage to the environment and living systems when present in uncontrolled amounts.

### 1.3.5.1 Importance of Detecting Fe(III).

Most fluorescent probes exhibit quenching upon binding with transition metal ions.[33, 48] Pollution due to heavy metals and associated impacts are increased due to industrial and development activities. Iron is a heavy metal that is an important component of biological systems such as oxygen transport, a cofactor in enzyme reactions, and the electron transport chain. The deficiency of $Fe^{3+}$ causes liver damage, diabetes, Parkinson's disease, and cancer.[49] However, excessive $Fe^{3+}$ levels can cause oxidative stress and neurogenerative disease.[50] Therefore, it is important to regulate $Fe^{3+}$ levels in water systems. The maximum allowable level of $Fe^{3+}$ in drinking water by the Environmental Protection Agency (EPA) is 0.3 ppm (5.4 µM).[51] Sensors for typical transition metals like $Fe^{3+}$ are scarce, as $Fe^{3+}$ is a well-known fluorescence quencher due to its paramagnetic nature. Hence, it has been difficult to develop a fluorescence sensor for its detection. Therefore, the development of rapid, accurate, and feasible $Fe^{3+}$ detection methods is significantly important.

### 1.3.6 Fluorescence.

A molecule predominately is in the electronic ground state; however, the absorption of appropriate energy causes the promotion of an electron to a higher energy orbital $S_n$ (n = 1, 2….). This instantaneous process is called excitation which takes about $10^{-15}$ s. This optical transition excitation happens from the lowest vibrational level of the electronic ground state to an accessible vibrational level in an electronic excited level. The convenient representation of the excited state and relevant transitions is offered by the Jablonski diagram (Figure 1-6). When considering a polyatomic molecule, the electronically excited states are further classified based on their multiplicity. For example, the triplet state ($S_3$) has three forms, the multiplicity of three whereas the singlet state ($S_0$) has one form, thus the multiplicity is one. These electronic energy levels are typically separated by energy orders of 10000 $cm^{-1}$).

A fluorophore can exist in vibrational energy levels (sub-levels such as 0, 1, and 2... etc.) which are separated by about 100 $cm^{-1}$. The most crucial electronic transitions are between the Highest Occupied Molecular Orbital (HOMO) and the Lowest Unoccupied Molecular Orbital (LUMO) of the ground state configuration. Herein, $\pi \rightarrow \pi^*$ and n $\rightarrow \pi^*$ transitions are of particular importance.
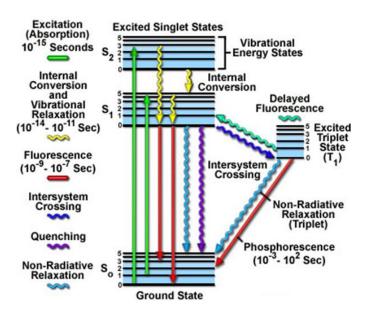
Figure 1-6. Jablonski diagram. Figure adapted from reference.[52]

After the excitation, the molecule quickly relaxes to the lowest vibrational level of the excited electronic state. Then, several processes could occur, such as an internal conversion (IC) to a higher vibrational level of $S_1$, then relaxing back to the lowest vibrational level of $S_1$. This process occurs in $10^{-12}$ s or less. Thereafter, the emission from the singlet state could happen, called "fluorescence". This emission occurs as the fluorophore decay from the singlet. This process typically occurs in $10^{-9}$ s. The emitted light is always of a longer wavelength than the incident, a characteristic of fluorescence emission known as Stokes shift.

However, if the singlet excited state changes spin multiplicity, an Intersystem Crossing (ISC) takes place. The subsequent emission from the triplet state is called "phosphorescence". The spin-forbidden process of ISC and formation of the triplet excited state is facilitated by the presence of $n\pi^*$ states or heavy atoms.

18

### 1.3.6.1   Fluorescent Chemosensors.

There are many traditional analytical methods for the detection of chemical species such as Atomic Absorption Spectroscopy (AAS), High-Performance Liquid Chromatography (HPLC) Inductively Coupled Plasma (ICP), etc. However, these methods require expensive instrumentation, and time-consuming sample preparation, with interference from the coexisting species being a  drawback. Fluorescence can be identified as the optimal signaling in sensing applications. This is an enormously sensitive technique, permitting the monitoring of both excitation and emission wavelengths. The most common type involves the cation or anion-selective chemosensors, which are capable of reporting the ion coordination process.

A chemosensor possesses selective binding between a specific receptor and analyte in the presence of another competing analyte. The receptor-analyte interactions transform into either optical or electrochemical forms. Especially, optical signals such as absorbance, fluorescence, phosphorescence, etc. are common. These methods are advantageous, as they are easily detectable with the naked eye, have low cost, and have simple instrumentation.

A chemosensor is a chemical sensor where the host molecule produces a signal when a guest is bound to the host. The device transforms chemical information, into an analytically useful signal. Compounds incorporating a binding site, a fluorophore, and a mechanism for communication between the two sites are called fluorescent chemosensors.[53, 54] A chemosensor interacts with specific target analytes in the presence of coexisting analytes. Generally, a chemical sensor consists of a receptor (binding subunit),

a spacer (or transducer), and a signaling (or read-out) subunit (Figure 1.7). Their fluorescence intensity depends on how the metal binds to the ligand (fluorophore). The fluorophore is the site for photonic transactions, the receptor is the site for both complexation and de-complexation, and the spacer holds both the fluorophore and the receptor close to each other.[55]
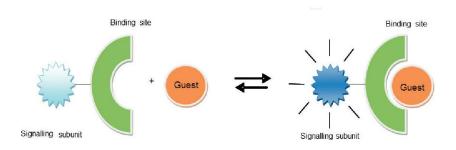


Figure 1-7.  Schematic presentation of chemosensor (signal = color, fluorescent or voltammetry, etc.) [56]

As a consequence of binding, fluorescence intensity shall increase called "turn-on" and the opposite is true for "turn-off". There are three types of fluorescent sensors, Class I; receptor (ionophore) and fluorophore are identical (e.g., 6-thienyllumazine), class II; has separate fluorophore and receptor linked with or without spacer, class III; based on fluorescence Resonance Energy Transfer (FRET).[57]

The receptor provides fast and reversible binding to the analyte of interest and the chemical is transformed into energy. The spacer is active unit properties change upon the interaction of the receptor with an analyte. Eventually, a spacer changes the geometry of the system and tunes the electronic interaction among the two former moieties.[58] Mostly, chemosensors are broadly categorized into optical, electrochemical, mass sensitive, and

heat-sensitive sensors based on the operating principle of the transducer.[59] The signaling

unit is the part responsible for reporting the binding event.

### 1.3.7 Optical Sensors.

These chemosensors exploit electromagnetic radiation as a source of the signal.

They are comprised of a molecular binding site, a chromophore or fluorophore, and a

mechanism for interaction between the two that change their optical properties. They can

be classified into two further categories as colorimetric chemosensor, and fluorescent

chemosensor.

### 1.3.7.1 Colorimetric Chemosensor.

A color change is used as a signaling activity upon the analyte binds with the

coordination sites of the sensor. Colorimetry is highly selective, sensitive, cheap, and direct

visual detection of color change. Most systems contain a system of conjugated bonds, it

was critical to determine the color of the dye by the energy difference between the ground

and the excited state of the molecule. In addition to conjugation, electron-donating groups

($-NH_2$, $-NR_2$, -NHR, -OH, -OMe, etc.), and electron-withdrawing groups ($-NO_2$, -COOH,

-CN, -C=O, $-SO_3H$, etc.) contribute to colorimetry. When both these groups were

introduced to the conjugated system of the molecule, a charge transfer band was observed.

### 1.3.7.2 Fluorescent Chemosensor.

The fluorescent chemosensor is capable of changing fluorescence properties in

response to the surrounding medium or through specific molecular recognition events.[60]

They usually measure the change in photophysical properties such as fluorescence

intensity, a shift in emission spectra, and a lifetime of the molecule on interacting with an analyte such as a cation, anion, or even neutral molecule. The fluorescent method is an overly sensitive, selective, cost-effective, and versatile method that offers detection of guest species. Therefore, they are often used in process control, food analysis, environmental monitoring, bio-medicinal science, and many more fields.[37, 53, 58, 61, 62] Fluorescent chemosensors often possess bind selectivity to the desired analyte in the presence of other coexisting analytes, toxicity should be minimized, and solubility in the desired medium.

### 1.3.7.3 Design principles of Fluorescent Chemosensors.

Fluorescence chemosensors generally consist of the fluorophore and a receptor unit. The fluorophore acts as the signaling unit, transforming information into an optical form. The receptor recognizes the analyte. The optical signal could be enhanced or quenching of fluorescence, or it may be the shifting of fluorescence wavelength. Here, the fluorophore and receptor unit can be attached in two different ways. There is a spacer between fluorophore and receptor that avoids the conjugation, and the other is the receptor directly attached to the fluorophore in a way that receptor is a part of the $\pi$ electron system of the fluorophore.[63]

### 1.3.7.4 Signaling Mechanisms for Chemosensor.

In this section, several conventional signaling mechanisms such as Photoinduced Electron Transfer (PET), Fluorescence Resonance Energy Transfer (FRET), excimer/exciplex formation, paramagnetic Fluorescence Quenching Mechanism, etc. are discussed.

Photoinduced Electron Transfer (PET) is a simple electron transfer process that occurs when a particular photoactive material interacts with light. This is one of the most important mechanisms for fluorescent sensing of cations and anions.[64] This method is widely used in most fluorescent sensors for the recognition of analytes.
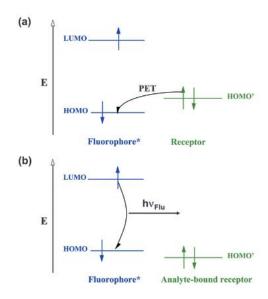


Figure 1-8. Molecular orbital diagrams for (a) in the absence of analyte and (b) in the presence of the analyte.[65]

The fluorescence in a molecule occurs when an excited electron in the LUMO (of the ground state $S_o$) goes to the HOMO (of the ground state $S_o$), releasing excess energy as light. In the absence of an analyte, the PET sensor absorbs energy, and the electron is promoted from HOMO of the fluorophore to LUMO of the fluorophore. (figure 1-8a).

However, in the presence of an orbital from another part of the same molecule (figure 1-8b) or from another molecule that has a lone pair and has an energy between that of HOMO and LUMO, and if this orbital is occupied (i.e., donor group), a PET from this

23

full orbital to the HOMO of the fluorophore can take place. This dropdown to the partially empty HOMO of the fluorophore prevents the excited electron from returning to the fluorophore HOMO (fluorescence quenching). However, if the donor and accepter are to be fixed within the same molecule, they must be separated by a spacer that is short enough for efficient electron transfer, but long enough to minimize the extent of electronic delocalization between partners.[57, 66]

### 1.3.7.4.2 PHOTOINDUCED CHARGE TRANSFER (PCT)/ INTRAMOLECULAR CHARGE TRANSFER (ICT)

Intramolecular Charge Transfer (ICT) or photoinduced Charge Transfer (PCT) takes place where push-pull chromophores are known as a donor- accepter molecules fluorophores contain electron-donating groups (such as $-NH_2$, $-NMe_2$, $-OCH_3$, conjugated with an electron-withdrawing group like $-C=O$, $-CN$ from the donor to acceptor upon excitation by light.[67] This leads to change in dipole moment, large stokes shift, etc.[68] When an electron donor group within the receptor interacts with a cation, the electron-donating ability of the receptor is reduced, resulting in a reduction in conjugation, and causing a blue shift of emission. Conversely, a cation interacts with the accepter group to enhance its electron-withdrawing character, leading to a redshift. These changes are accompanied by quantum yield and lifetime. And these photophysical effects depend on the charge and the size of the cation as well as the nature of the receptor.[69]

### 1.3.7.4.3 FLUORESCENCE RESONANCE ENERGY TRANSFER (FRET)
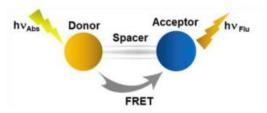


Figure 1-9. Representation of FRET.[70]

This is the most widely non-radiative process, involving the energy transfer of a donor fluorophore in an excited electronic state, to a nearby acceptor chromophore. This happens when both fluorophores are fluorescent and act as an energy donor and acceptor respectively linked together with a non-conjugated spacer (figure 1-9). For FRET to occur, donor and acceptor fluorophore must be nearby, the emission spectrum of donor fluorophore must overlap with the absorption spectrum of acceptor fluorophore, and the relative orientation of donor emission dipole moment and acceptor absorption moment must be parallel to each other.[38, 45, 46]

### 1.3.7.4.4 EXCIMER/EXCIPLEX FORMATION.

This phenomenon occurs when aromatic rings are not bound in the ground electronic state, but bound together through weak π-stacking interactions in the excited electronic state. Thus, an electronic interaction of one aromatic ring leads to an enhanced interaction with its neighbor ring, resulting in an excited dimer (excimer/exciplex). Excimer/exciplex formation is a reversible process involving the interaction of the excited state of a molecule with the nearby ground state of a molecule that emits fluorescence at a longer wavelength (red-shifted) than that of a monomer.[71, 72]

25

### 1.3.7.4.5 CHELATION ENHANCED FLUORESCENCE (CHEF)

This is the mechanism behind the fluorescence turn-on mechanism. This is common in ligands having heteroatoms with lone pairs of electrons such as nitrogen, oxygen, or sulfur. In the absence of metal ions, the ligand shows no fluorescence or very little intensity due to the PET effect. However, when a metal ion coordinates with the quenching lone pair, brings the energy of the lone pair below the fluorophore HOMO, blocking the quenching and restoring fluorescence.[57]

### 1.3.7.4.6 PARAMAGNETIC FLUORESCENCE QUENCHING MECHANISM (CHEQ).

This phenomenon is observed frequently in a large number of metal complexes, due to a half-filled electron of metal ion strongly interacting with $\pi$- electrons of the fluorophore and providing a pathway for Intersystem Crossing (ISC) from the energy of singlet excited states of the fluorophore to the states of higher multiplicity. The most common examples are transition metals like $Fe^{3+}$, $Cu^{2+}$, $Co^{2+}$, $Ni^{2+}$, etc. (figure 1-10)
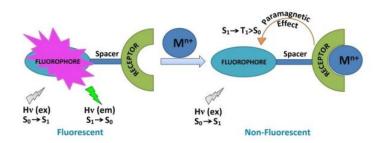


Figure 1-10. Schematic diagram showing paramagnetic fluorescence quenching.

Fluorescence spectrometry is utilized because it is a simple low-cost method that is both selective and highly sensitive. [73] A 'metal sensor' is described as a device that is

capable of responding to the presence of a heavy metal ion reversibly and continuously. Many indicators cannot be used in optical sensors because of unfavorable analytical wavelengths, poor photostability, low molar absorptivity, or the need for additional reagents. Upon binding with the metal ion, most indicators change color, with one band appearing as another disappears, rather than an intensity change of one single band leading to changes in the initial ligand. Some fluorophores display enhanced fluorescence due to a change in the fluorophore.

### 1.3.8 Pyridine-2,6-dicarboxamide scaffold-based sensors.

Pyridine-2,6-dicarboxamide scaffolds are noteworthy because they create an $N_3$ pincer cavity via two five-membered chelate rings between $N_{pyridine}$ and $N_{amide}$ groups, involve two anionic σ-donating groups $N_{amide}$ groups not only result in the formation of stable coordination complexes, but also endows such ligands towards the stabilization in their higher oxidation states, and the possibility of introducing appended functional groups. This helps either introduction of protecting groups, creating either sterically hindrance groups or secondary coordination environment adjacent to the metal ion coordinated within the $N_3$ pincer cavity.[74-76]

Many probes for iron exhibit a "turn off" fluorescence response towards its binding. However, the sensor must be able to distinguish between two oxidation states of Fe(II) and Fe(III) because of the propensity of Ferrous to oxidize into ferric. The following table 1-3 shows some examples of pyridine-based scaffold sensing activity all forming 1:1 complexes of ligand: metal.

In the first example, three pyridine-2,6-dicarboxamide based probes incorporated appended phenyl, naphthyl, and anthracenyl groups are present.[77]

Table 1-2. Pyridine ligands for metal sensing

| Structure | Metal | $K_a$ | LOD (µM) | Ref. |
|---|---|---|---|---|
|  | $Fe^{3+}$ | $3.31 \times 10^3$ | - | 77 |
|  | $Fe^{3+}$<br><br><br>$Al^{3+}$ | $4.24 \times 10^3$ ($L_1$),<br>$3.77 \times 10^3$ ($L_2$)<br><br>$2.16 \times 10^4$ ($L_1$)<br><br>$1.28 \times 10^3$ ($L_2$) | $1.43(L_1)$<br>$2.48(L_2)$<br><br><br>$1.14(L_1)$<br><br>$1.73(L_2)$ | 78 |
|  | $Pb^{2+}$<br><br><br>$Cu^{2+}$ | $5.65 \times 10^8$ $M^{-2}$<br><br>$8.89 \times 10^3$ $M^{-1}$ | 2.31<br><br><br>1.49 | 79 |

We chose the pyridine-based thiol molecule PB9 probe because of its excellent spectroscopic properties, high stability to light, favorable absorption and emission wavelength, high quantum yield, and large extinction coefficients. This recently developed pyridine-based thiol ligand is used as a colorimetric chemosensor for ferric ion detection in DMSO. PB9 was found to function as an excellent $Fe^{3+}$ sensor, while other common metals, particularly other transition metals, alkalis, and alkaline earth metals produce

28

minimal spectral change. Their synthesis, characterization, and optical properties will be discussed in a subsequent chapter.

## 1.4    Thiol - Functionalized Silica gels.

Silica gels have the advantage of surface modification through the silanol groups present on their surface. These can be modified through reactions with coupling agents to affect the physical and chemical properties of the silica gel's surface. They can also be tuned with various functional groups so that they act as solid support for chelating agents. Modified silica has gained much attention and uses in many applications such as the removal of copper, zinc, cadmium, lead, gold, and silver. [80-82] It is known that thiol groups in compounds have a strong affinity toward heavy metals and make strong bonds with heavy metals. Further, (solid) silica-supported cysteine has been used as an adsorbent of these heavy metals from aqueous systems. [83] In addition to these amino acids, ethylene sulfide immobilized on silica has shown improved removal of lead.[84]



Figure 1-11. Ethylene sulfide functionalized on silica.[84]

A certain adsorbent should possess good properties such as a high surface area, availability, easy preparation, and cheapness. Silica shows all these desirable properties for adsorption, as they are having a network of Si-O covalent bonds. The bond energy is relatively high for Si-O in this lattice of $SiO_2$ 452 kJ/mol with a higher melting at 1600 °C. Particle sizes can range from 500 to 800 $m^2/g$.[85]

A spacer molecule, such as aminopropyltriethoxysilane (APTS) is widely used for immobilization of thiol molecules on silica surface which then facilitates the introduction of various reactive groups onto the silica surface.[86] The carboxylic acid groups then, can be incorporated due to this coupling agent.

In the subsequent chapters the carboxylic acids groups in dithiol molecule AB9 were used to condense and form amide (-CONH-) linkages. The AB9 is a dithiol molecule 2,2'-(isophthaloylbis(azanediyl))bis(3-mercaptopropanoic acid (figure 2) designed with appended cysteine molecules (acidic version of B9).



Figure 1-12. The proposed molecular structure of AB9, 2,2'-(isophthaloylbis(azanediyl))bis(3-mercaptopropanoic acid.

AB9 is a good candidate for coordinating with metals through its amino, thiol, and also by carboxylic acid groups. pKa values of these groups are 8.17-8.78 ($NH_2$), 10- 11 (SH), and 1.62-2.44 (COOH). Cysteine is proven to interact with metals such as Hg, Cd, Pb, and several other metals, therefore they are used as model compounds for studying cysteine-containing proteins and peptides.[87, 88]

## 1.5    Thiol-Functionalized Magnetic Nanoparticles (MNP)

Nanoparticles are in a size range of 1- 1000 nm. Among them, MNP is a promising adsorbent material with a size range of 1-100 nm, high surface areas, high magnetization,

and high surface energy.[89-91] They have many applications in drug delivery, catalysis, adsorption studies, etc.[89, 92, 93] They can be tuned to prevent unwanted agglomeration and oxidation. The following description serves as a brief introduction to AB9-MNP synthesis and subsequent steps.

Magnetite ($Fe_3O_4$) is used to form the basis of MNP. Their magnetic properties are due to the double-exchange interactions. However, upon exposure to air, magnetite oxidizes to maghemite ($\gamma$- $Fe_2O_3$). A typical synthesis reaction of magnetite is illustrated below (equation 1).

$$FeO + Fe_2O_3 \rightarrow Fe_3O_4 \ (1)$$



Figure 1-13. Crystal structure of magnetite ($Fe_3O_4$).[94]

Magnetite is a crystalline material, having a cubic spinel structure (figure 1-13). Magnetite is a cubic spinel structure packed along the (1,1,1) plane, in which $Fe^{2+}$ and $Fe^{3+}$ occupy octahedral lattice voids and $Fe^{3+}$ tetrahedral lattice voids as illustrated in figure 3.[95] The conductivity arises from the electrons hopping on the octahedral sites between $Fe^{2+}$

and $Fe^{3+}$.[96] They show ferrimagnetism at the nanoscale level, which bulk magnetite does not have due to the spin magnetic moment of $Fe^{2+}$ and $Fe^{3+}$ ions.[91]

The stability of nanoparticles is a crucial aspect of their applications. Magnetite has a point zero charge (PZC) at pH 7-8.[97] Particles tend to sediment near the PZC. Thus, for magnetite, it is very close to neutral conditions which need to perform passivation to avoid agglomeration.

In this study, citric acid was used as a simple and inexpensive surface passivation surfactant molecule. It helps the formation of monodispersed nanoparticles.[98]

A common surface coating method called the Stober method can be used to prepare a nanometer-sized layer of silica through the hydrolysis and condensation of alkoxysilanes. However, the acid or base promoted synthesis often uses tetraethoxysilane (TEOS).[85, 86] This could lead to different kinds of surface silanols such as geminal, isolated, and vicinal with several hydration layers covering the surface.[99]

3-(aminopropyl)triethoxysilane (APTS) is commonly used to promote adhesion between silica substrates and organic or metallic materials. Thereafter, primary amines and thiol groups act as coupling agents. Dry toluene is often used for better loading and reproducibility.

The desired functionalities of nanoparticles can be added by further modification. For example, carboxylic acids, amines, thiols, phosphates, etc.

## 1.6    The goal of the current work.

The goal of current work can be assigned to three broad areas. The primary goal of the dissertation research is to explore the binding, the removal of Pb(II) using PB9 (which is a pyridine version of B9), containing two sulfur equivalents as terminal thiol groups, supported in a pyridine ring. In the first aspect, the thiophilic nature of Pb(II) and the relativistic effect were considered for the formation of PB9/Pb(II) compounds in a 1:1 and 1:2 ratio, examine their structures and subsequent Pb(II) sequestration. Here, the "complete" removal shall define the removal of Pb(II) well below the typical maximum contaminant level (15 ppb for lead), and irreversible refers to stable covalent bond formation between the Pb(II) and PB9.

In a second aspect, PB9 was employed for the higher selective, sensitive, and reversible sensor for the spectroscopic determination of $Fe^{3+}$ ions over many other elements present in a non-aqueous system.

As the third aspect, this dissertation also serves a focus on aqueous Pb(II) sequestration using a synthetic ligand AB9. And it is proven effective in chelating for "soft' metal ions. The ligand is proven of an effective remover for Pb(II) from aqueous solutions as a direct precipitation chelator. Thus, the AB9 ligand will be linked to magnetite nanoparticles or MNPs, and commercial silica after fabrication of the surface using established literature procedures and previous procedures used by a graduate student in the group. The goal of this study is to achieve a well below MCL (Maximum Contaminant Level) of Pb(II). Herein, magnetic nanoparticles and silica functionalized AB9 were used for the Pb(II) removal studies.

CHAPTER 2. SYNTHETIC PYRIDINE THIOL PB9 FOR PB(II) REMOVAL FROM WATER

## 2.1 Introduction.

Research on pollution of the aquatic environment has a long history focusing on heavy metal-containing industrial waste. Eventually, these are ingested by aquatic animals, plants, and crops into the human body. This approach has been influential in the field because these heavy metals are difficult to biodegrade.[100] Lead is seen as one of the major toxic chemicals of public health concern by the World Health Organization (WHO).[4] Lead is a toxic metal known for many coordination numbers and its amphoteric properties.[90] These properties lead to many issues when interacting with remediation systems. The different methods currently used are chemical precipitation such as sulfides and hydroxides, biological treatment, chelating ion exchange, electrolytic methods, and reverse osmosis.[29, 101] Chemical precipitation agents often require elevated doses, decompose to hazardous materials,[101] or form weak bonds upon binding leading to decomposition and release back into the environment. These are also often unstable under adverse pH conditions.

## 2.2 Pb(II) compounds formation with S/N Ligands

Lewis acids of p-block elements can adopt varying coordination geometries in compounds with the configuration depending on the metal and ligand involved. Pb(II) thiolates are considered unwilling to disproportionate and hydrolyze, and also suffer from insolubility in non-coordinating solvents preventing crystallization.[102, 103] Therefore, structural data is often limited. Geometries are similar in two- and three-coordinate Pb(II)-thiolates in compounds of [Pb($S_2N_2$), and [Pb($S_2N_2$)($NH_3$)] respectively except when in the presence of ammonium later.[104] Four-coordinated Pb in [Pb($SCH_2CH_2NH_2$)$_2$] and [Pb(3-

CF$_3$-PyS)$_2$] has pseudo-trigonal bipyramidal geometry.[105] However, a five-coordinated monomeric Pb(II)-thiolate, [Pb(bis(4-N-ethylthiosemicarbazone)-2,6-diacetylpyridine)(DMSO)], was found to have a distorted planar pentagonal geometry because of coordination with Pb(II).[106] The first five-coordinated Pb(II) with pentagonal geometry and equatorial positions occupied by the N$_3$S$_2$ donor set of the ligand was demonstrated in [Pb(bis(4-N-methylthiosemicarbazone)-2,6-diacetylpyridine)], Figure 2-1.[107]
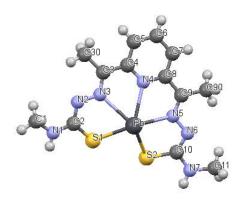


Figure 2-1. Molecular structure of [Pb(bis(4-N-methylthiosemicarbazone)-2,6-diacetylpyridine)] redrawn with Mercury software along the C axis.[107]

Heavy metals such as Pb show a high tendency to form complexes with nitrogen, sulfur- and oxygen-containing ligands of biological matter. Some macromolecules containing N$_3$S$_2$ are shown in Figure 2-2. L= ligand making [Pb(L)(MeOH)(H$_2$O)]$^+$. Here, the Pb(II) is surrounded by three nitrogen, two sulfur atoms, and solvent molecules (water and methanol) giving a *nido*-hexagonal bipyramid.[108]
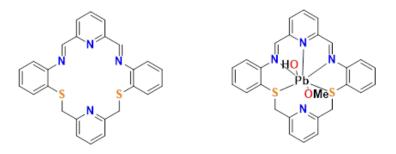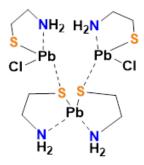
Figure 2-2. Structure of diimine (L) and [Pb(L)(MeOH)(H$_2$O)]$^+$.[108]

The complex [{PbCl(SCH$_2$CH$_2$NH$_2$)}$_2${Pb(SCH$_2$CH$_2$NH$_2$)$_2$}] (figure 2 -3) has Pb coordinated to S and Cl with having weaker interactions with N. With the stereochemically active lone pair, the compound exhibits a distorted pseudo- octahedral geometry.[21] The compound was prepared in a higher concentration of NaOH, which leads to deprotonate - NH$_3$ and subsequently allows the interactions for Pb$\cdots$N.



Figure 2-3. Structure of [{PbCl(SCH$_2$CH$_2$NH$_2$)}{Pb(SCH$_2$CH$_2$NH$_2$)$_2$}].[21]

Pb shows a high tendency to form complexes with nitrogen, sulfur- and oxygen-containing ligands of biological matter. We have investigated various thiol-containing molecules for the remediation of heavy metals, demonstrating the thiol group as a very reactive, functional organic group. The dithiol ligand B9, is shown in figure 2.4a [common name 1,3-benzenediamidoethanethiol, N, N′- bis(2-mercaptoethyl)isophthalamide], was

designed with the binding sites of metal cations in mind. The binding can be predicted using hard-soft acid-base theory (HSAB).[4, 109] Accordingly, soft metals interact with soft base ligands and vice versa. The interaction between hard acids and hard bases is ionic, whereas covalent interactions are observed for soft bases and soft acids. B9 behaves as a soft base (thiol) with soft acids (metals) like $Hg^{2+}$, $Cd^{2+}$, and $Pb^{2+}$. This produces an insoluble metal-ligand precipitate which can then be mechanically removed from the solution between the pH ranges of 0-14.[24] B9 irreversibly immobilizes Hg in gold mining effluent[27] under a variety of laboratory conditions, and it can reduce divalent metal concentrations in water and sediments to below EPA limits.[110]
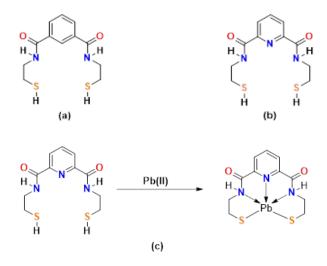


Figure 2-4. Structure of (a) B9; 1,3-benzenediamidoethanethiol, (b) PB9; 2,6-pyridinediamidoethanethiol, and (c) Reaction and the predicted molecular structure of Pb(II) with PB9

Pyridine-2,6-dicarboxamides are important molecular receptors, showing affinity towards d and f block metal cations.[111] Derivatives of pyridine-2,6-dicarboxamides with $Cr^{3+}$, $Mn^{3+}$, and $Cu^{2+}$ have been studied.[112] This ligand also can act as an anion receptor.[113] Moreover, 2,6-pyridinediamides have a strong preference for *syn-syn* conformations for

37

both amides, owing to the hydrogen bonding of pyridine nitrogen atom and lone pair repulsion in other confirmations.[113-115] Similar to B9, PB9 immediately forms insoluble precipitates with heavy metals. Our group previously has studied the efficiency of PB9 for the removal of Cd(II) and Cu(II).[32]

Here, we discuss the removal of Pb(II) from an aqueous solution using the pyridine-based dithiol compound PB9. This PB9 reduces the cost for treatment facilities with its quick reaction speed and removal of >99% of aqueous Pb(II). Moreover, PB9 is synthesized while keeping cost in mind.

## 2.3    Experimental Section.

## 2.3.1    Materials.

All the analytical grade materials for synthesis including cysteamine, triethylamine, and 2,6-pyridinediacid dichloride (Sigma Aldrich) were purchased from commercial suppliers and used without further purification.

## 2.3.2    Sample Preparation.

PB9 (A) and PB9/Pb(II)  solutions with ratios of 1:1 and 2:1, referred to as B and C, respectively, were prepared by dissolving PB9 in DMSO (0.1 and 0.2 mmol) and used a suitable further dilution in DMSO, followed by the addition of $Pb(CH_3COO)_2.3H_2O$ (0.1 mmol). These solutions (A-C) were used in UV-Vis spectroscopy. DMSO was used as the blank. A*-C* were used in the NMR study using $d_6$-DMSO. See below table 2-1.

Table 2-1. Compositions of PB9/Pb(II) solutions

| solution | PB9/Pb(II) | $C_{Pb(II)}$ (mM) | $C_{PB9}$ (mM) | solution | PB9/Pb(II) | $C_{Pb(II)}$ (mM) | $C_{PB9}$ (mM) |
|---|---|---|---|---|---|---|---|
| A | - | - | 20 | A* | - | - | 50 |
| B | 1.0 | 10 | 10 | B* | 1.0 | 25 | 25 |
| C | 2.0 | 10 | 20 | C* | 2.0 | 25 | 50 |

### 2.3.3    Characterization.

^{1}H NMR and ^{13}C NMR spectroscopic spectra were recorded at 300 K on a Bruker AV 500 NMR spectrometer. $d_6$-DMSO was used for solutions A*-C* and solid samples of PB9/Pb(II)= 1:1 and 2:1 were acidified with HCl due to their poor solubility in less coordinated solvents. Chemical shifts are expressed in parts per million (ppm) relative to internal $Me_4Si$. Electronic UV-Vis absorption spectra were measured at room temperature using a UV-Vis Agilent spectrophotometer. 2 mL samples were loaded into 1 cm quartz cells; DMSO was used as the blank. The Raman spectra for solids of crystals PB9, and solids PB9/Pb(II) in 1 and 2 were obtained using an XDR Smart Raman spectrometer. The IR spectra were obtained over the range of 500- 4000 cm$^{-1}$ with 2 cm$^{-1}$ resolution, using a NICOLET 6700 FT-IR spectrometer. Aqueous concentrations of Pb were determined with an Agilent 5110 SVDV inductively coupled argon plasma optical emission spectrometer (ICP-OES) with the detection limits for lead analyses as, 0.001 mg/L. Elemental analyses (C, H, and N) were carried out on a LECO CHN628 analyzer, Pb on an Agilent 7900 ICP-MS, and S in LECO S632. All pH measurements were made with a model Mettler Toledo.

The purity of all compounds was assessed by Reverse Phase (RP)-HPLC using an Agilent Technologies 1100 series HPLC instrument and an Agilent Phase Eclipse Plus C18 column (4.6 mm X 100 mm; 3.5 µm particle size). The powder XRD analyses on crystals of PB9 and PB9/Pb(II) in 1 and 2 solids were mounted on a glass slide and analyzed with 20 kV and 20 mA using Cu $K_{\alpha 1}$=1.540598 Å. ESI-MS was performed by dissolving solids in MeOH. A 1:10 dilution with a saturated solution of solids to prepare solutions for direct injection of 50% v/v $H_2O$. A 1 mM NaOH to the negative mode NaOH sample.

### 2.3.4 Synthesis of chelator PB9; pyridine-2,6-dicarboxylic acid, bis-[(2-mercapto-ethyl)-amide].

Cysteamine (111.2 mg in 10 mL $CHCl_3$) was stirred under nitrogen and 0.2732 mL of triethylamine was added. This reaction mixture was stirred for ~ 5 min and pyridine-2,6-diacid chloride (100 mg in 3 mL $CHCl_3$) was added dropwise. The reaction mixture was then stirred under $N_2$ for ~12 h and the resulting solution was extracted with 5% HCl, to a clear solution, next, rotation evaporated to obtain a white precipitate with a Yield of 89%. The crude material was recrystallized with ethanol to yield colorless needles (86%). Melting point (MP) of crystals 188- 190 ℃. Analytically calculated for $C_{11}H_{15}N_3O_2S_2$: C, 46.3; N, 14.72; H, 5.3; O, 11.2; S,22.5; Found: C, 47.43; N,14.69; H, 5.65. MS (+ESI, MeOH, *m/z*): 286.0682 ([PB9+ H]$^+$). The IR data confirmed the presence of the PB9 major functional groups. The confirmed wavenumbers of the functional groups included: secondary amine (νNH) 3266 cm$^{-1}$, aromatic (νCHs) on the pyridine ring 2979, 2933 cm$^{-1}$, sulfur–hydrogen (νSH) 2527 cm$^{-1}$, carbonyl (C=O) 1721, 1645 cm$^{-1}$, and the carbon-sulfur bond (C–S) 674 cm$^{-1}$. $^1$H-NMR (500 MHz, CDCl$_3$) δ:1.48 (t, **SH**, 2H), 2.89 (m, **CH₂**SH,

4H), 3.71 (m, NHC**H₂**, 4H), 8.05 (t, Py**H**. 1H), 8.23 (s, N**H**CH₂, 2H), 8.38 (d, Py**H**, 2H).

$^{13}$C-NMR ($d_6$-DMSO, ppm): 163.5(C=O), 148.9, 139.2, 125.1 (C$_{py}$), 42.2, 23.8 C$_{aliphatic}$).



Scheme 2-1. Synthesis of PB9.

## 2.3.5    Crystal structure determination.

X-ray quality crystals of PB9 were obtained in high yield by the recrystallization of crude PB9 in ethanol. X-ray diffraction data were collected on a Bruker D8 Venture diffractometer unit using Mo$K_\alpha$ radiation ($\lambda$= 0.71073 Å) from a crystal mounted with polyisobutene oil on a glass fiber at 90 K.



(a)                (b)
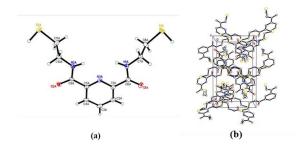
Figure 2-5. An ellipsoid plot of the non-disordered PB9 molecule (left) and a packing plot viewed down the c-axis of the crystal structure of PB9.

41

The crystal and structure refinement data for PB9 are summarized in Table 2 - 2. Crystallographic data were deposited in the Cambridge Crystallographic Data Centre (CCDC) [reference number 2129303]. The crystal structure of PB9 is twinned by non-merohedry[116] by a two-fold rotation about c* (Figure 2.5). There are two molecules in the asymmetric unit, one of which has a disorder of one of its thiol groups.

Table 2-2. X-ray Crystal Structure and Refinement Data for PB9.

| Empirical Formula | PB9 |
|---|---|
| | $C_{11} H_{15} N_3 O_2 S_2$ |
| Molecular Weight (g/mol) | 285.38 |
| Temperature (K) | 90.0(2) |
| X-ray radiation (Å) | Mo $K_\alpha$ (0.71073 Å) |
| Space Group | Monoclinic, $P2(1)/c$ |
| Unit Cell Dimensions (Å) (°) | a = 16.1069(10) Å     alpha = 90<br>b = 9.7387(5) Å     beta = 93.802(2)<br>c = 17.5526(10) Å     gamma = 90 |
| Volume | 2747.2(3) Å$^3$ |
| Z | 8 |
| Absorption Coefficient | 0.385 mm$^{-1}$ |
| F(000) | 1200 |
| Crystal Size (mm) | 0.240 x 0.080 x 0.060 |
| Theta Range | 2.326 to 27.538 |
| Completeness to Theta = 25.242 | 99.5% |
| F$^2$ | 1.140 |
| Final R indices [I>2sigma(I)] | $R_1 = 0.0409$, wR2 = 0.0972 |

### 2.3.6 Synthesis of PB9/Pb(II) = 1

2 g (7 mmol) of PB9 in 20 mL of methanol was stirred under $N_2$ and NaOH (0.28 g, 7 mmol) was added. The 2.66 g (7 mmol) of $Pb(CH_3COO)_2.3H_2O$ in 10 mL DI water was added dropwise. A yellow precipitate formed immediately and was refluxed under $N_2$ for 24 h. This was then filtered and washed with cold methanol, water, and vacuum dried. yield 2.34 g (69%). MP.>240 °C. IR (cm$^{-1}$): 3355s ($\nu$NH), 2983, 2881 [$\nu$CH(arom)], 1646 ($\nu$C=O). Raman (cm$^{-1}$): 306, 164 (Pb-S). Analytically Calculated for $C_{11}H_{13}N_3O_2S_2Pb$: C, 26.94; N, 8.57; H, 2.67; O, 11.2; S,22.5; Found: C, 27.73; N,8.51; H, 3.01; Pb, 37.2. The compound was found to be insoluble in the solvents normally found in the lab. ICP; Pb:S ratio = 605.13/249.16 = 2.43.

### 2.3.7 Synthesis of PB9/Pb(II) = 2

2 g (7 mmol) of PB9 in 20 mL of methanol and NaOH (0.28 g, 7 mmol) was added. Then 1.33 g (7 mmol) in 10 mL DI water was added dropwise and refluxed for 24 h. Yield 1.50 g (40%). Anallytically Calculated for $C_{11}H_{13}N_3O_2S_2Pb$: C, 26.94; N, 8.57; H, 2.67; O, 11.2; S,22.5; Found: C, 27.53; N,8.63; H, 2.84; Pb, 37.37. Mp; >240 °C. IR (cm$^{-1}$): 3314s ($\nu$NH), 2983, 2881 [$\nu$CH(arom)], 2887m [$\nu$CH(methylene)], 1654, 1532 ($\nu$C=O), 1535ss ($\delta$NH), 1277m [in- plane bending C-H(arom)], 693 [out-of-plane bending C-H(arom)]. Raman (cm$^{-1}$): 306, 164 (Pb-S). The compound was found to be insoluble in the same solvents as compound PB9/Pb(II) = 1. ICP; Pb:S ratio = 624.38/240.47= 2.6.

### 2.3.8 Computational methods.

Density functional theory (DFT) and time-dependent DFT (TD-DFT) calculations were carried out within the Gaussian16 (Revision A.03) software suite.[117] The ωB97XD

functional,[118] which includes long-range corrections and empirical dispersion, was employed with the 6-31G(d,p) Pople basis set for non-metals and LANL2DZ basis set for the transition metal.[59, 119, 120] Normal mode analyses were carried out for optimized geometries to ensure that no negative frequencies were present. The SMD implicit solvation model[121] was used to compute the fixed concentration intrinsic free energies of solvation in methanol.[122] The combination of computed free energies and gas-phase energies was employed to determine the intrinsic solvation free energy. All optimized geometries and Natural Transition Orbitals (NTOs) were visualized using GaussView 5.0.9. [123]

### 2.3.9   Pb(II) removal kinetics.

The initial Pb(II) concentration of 50.0 ppm in 39% ethanol/61% deionized water was used for all experiments. For metal removal kinetics studies, 6.88 mg and 13.76 mg (depending on stoichiometry) of PB9 were introduced to a 100 mL metal ion solution in an Erlenmeyer flask under $N_2$ (unopened to air), with vigorous agitating using a magnetic stirrer. A water bath was used to maintain the constant temperature (23 $^O$C). At desired time intervals at 15, 30, 45, 60, and 600 minutes, agitation was interrupted and aliquots of 10 mL were collected and filtered with 0.2 µm Nalgene syringe filters. Residual Pb(II) concentration was measured using the (ICP-OES, Agilent 5110 SVDV) with the detection limit of, 0.001 mg/L.

### 2.3.9.1 Dosage of PB9.

The initial dose of PB9 (6.88 mg) was based on a 1:1 stoichiometry with Pb(II). The second series of experiments were conducted with the ligand (13.76 mg) dose increased to 2:1 to increase the higher removal % of Pb(II).

Pb(II) metal removal % was determined as follows;

$$removal\ \% = \frac{(C_0 - C_t)}{C_0}\ X100 \quad (1)$$

where $(C_0)$ and $(C_t)$ are the initial and final Pb(II) metal ion concentrations (ppm), respectively.

The rate constants are derived from the model.

$$\Delta G = -RTLnK_c \text{ and } \Delta G = \Delta H - T\Delta S$$

$$-RTLnK_c = \frac{\Delta S}{R} - \frac{\Delta H}{RT} \text{ and } K_c = \frac{C_e}{C_o - C_e} \quad (2)$$

where $K_c$ is the equilibrium constant, $\Delta G$ is the Gibbs free energy (J/mol), $\Delta H$ the enthalpy (J/mol), $\Delta S$ the entropy (J/mol K), $T$ the absolute temperature (K), $C_o$ and $C_e$ are the initial and equilibrium concentration of adsorbate and R the gas constant (8.314 J/ mol K).
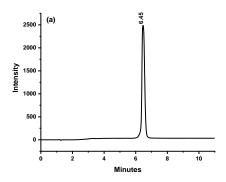
### 2.3.9.2 Leaching Studies.

Fifty mL of 500 ppm of metal Pb(II) salt solution was prepared using 39% ethanol/61% deionized water. The solution was then added to an equimolar amount of PB9 dissolved in 95% ethanol (~2-3 mL). The reaction mixtures were stirred for 5 h under $N_2$,

and the resulting precipitates were filtered under gravity and dried under vacuum for a day. The precipitates were transferred into Erlenmeyer flasks, followed by the addition of 100 mL of deionized water to each. 10 mL aliquots were transferred by syringe into tubes after 3, 7, and 10 days for metal concentration measurements. The metal concentrations of the Pb solutions were measured using ICP-OES.

## 2.4    Results and Discussion

PB9 was prepared in a simple synthetic procedure in the presence of triethylamine as the base in chloroform (Scheme 2.1). Pure PB9 was obtained with a yield of 86% after recrystallization in ethanol and was characterized by $^1$H NMR, $^{13}$C NMR, FT-IR, Raman, HPLC, and ESI-MS (figure 2.6). Attempts to obtain PB9/Pb(II) compounds in single crystals suitable for X-ray analysis failed; therefore, coordination modes are proposed based on spectral methods.
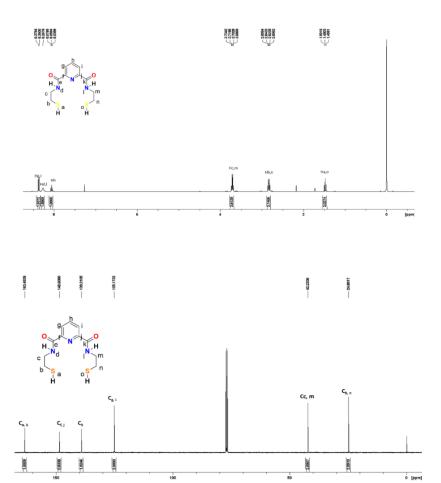
Figure 2-6. (a) HPLC, (d) $^1$H-NMR, and (e) $^{13}$C-NMR of PB9.

**FT-IR and Raman analysis of PB9, and PB9/Pb(II) precipitates.**

FT-IR analyses were performed in the range of 500- 4500 cm$^{-1}$, with a scan number of 264. The important peaks are shown in table 2.3. The amide part involvement was checked by using the A band (NH stretching) at 3500 cm$^{-1}$, the amide I band (C=O stretch at 1700- 1600 cm$^{-1}$, and the amide II band (C-N stretch coupled to NH bending) at 1550 cm$^{-1}$. A fingerprint region was also analyzed depending on the type of functionality engaged in bonding. The FT-IR spectrum of uncoordinated PB9 (figure 2.7) confirms the presence of major functional groups; carbonyl (-C=O) 1721 cm$^{-1}$, 1646 cm$^{-1}$, the (-C–S) 676 cm$^{-1}$ bond, the aromatic (CHs) on the pyridine ring 2977, 2936 cm$^{-1}$, and the secondary amine (-NH-) 3266 cm$^{-1}$ in the 3500- 3200 cm$^{-1}$ region[107], thiol (-SH) 2528 cm$^{-1}$ peak. In both PB9/Pb(II) compounds, the IR bands corresponding to the stretching modes of the amide A band (NH stretching) in the 3500- 3200 cm$^{-1}$ region[107] of are blue-shifted to 3355 cm$^{-1}$ and 3391 cm$^{-1}$ respectively, compared to the free PB9 which appears at 3266 cm$^{-1}$. The band shifting to a higher frequency is probably due to the interactions of Pb(II) with N-H and C-N groups of free ligand PB9. However, there is evidence of solvent present by having a broad peak in the higher wavenumber. Furthermore, the bands corresponding to $v$(C-N) mode appears slightly shifted in both Pb(II) solid precipitates, which is an indication of the metal binding to the pyridine nitrogen atoms. Further evidence for this coordination is supported by shifting pyridine band deformation bands to higher frequencies in the complexes.

The missing peak in both Pb(II) compounds was the -S-H bond, which was replaced by the expected metal–sulfur bond. The absence of bands in the 2600- 2800 cm$^{-1}$ region, suggests the absence of any thiol tautomer. No evidence of S-S stretching (500-

400 cm$^{-1}$)[124] or stretching S=O (1400- 1200 cm$^{-1}$) was observed, indicating oxidation of the product did not occur. The metal–sulfur bond is located at far IR wavelengths that are beyond the Nicolet-Avatar 320 FT-IR series spectrometer's detection limit of 500 cm$^{-1}$.
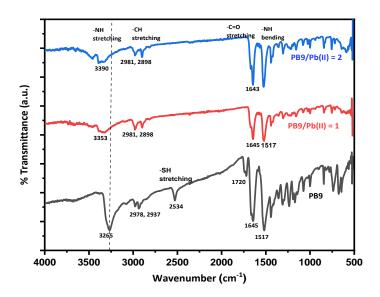


Figure 2-7. FT-IR spectra of solids PB9, and PB9/Pb(II) compounds.

Raman spectroscopy (figure 2-8) further confirms Pb- S contact by shifting the -C-S peak to a lower wavenumber from 664 cm$^{-1}$ for PB9 to 646 cm$^{-1}$ for both PB9/Pb(II) compounds. The band at 164 cm$^{-1}$ was assigned to $v$Pb-S. These values are similar to values for $v$Pb-S reported in the literature for tetrahedral lead compounds such as $(C_6H_5)_3PbSC_6H_5$.[110] These data suggest the coordination mode of PB9 is similar in both Pb(II) compounds, through the $N_3S_2$ environment, with coordination with nitrogen and covalent bonding with sulfurs.
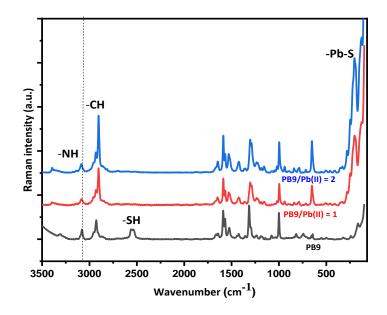
Figure 2-8. Raman spectra of solids PB9, and PB9/Pb(II) compounds.

Table 2-3. Selected vibrational bands with assignments for PB9, and PB9/Pb(II) compounds.

| Raman (cm⁻¹) | | | IR (cm⁻¹) | | | |
|---|---|---|---|---|---|---|
| **PB9** | **1** | **2** | **PB9** | **1** | **2** | **Assignment** |
| 3079 | 3087 | 3081 | 3266 | 3355 | 3391 | $\nu$(N-H) A band |
| 2560 | - | - | 2528 | - | - | $\nu$(S-H) |
| 1662 | 1647 | 1641 | 1721 | 1646 | 1646 | $\nu$(C=O) I amide |
| 1644 | | | 1645 | | | |
| 1588 | 1587 | 1587 | | 1589 | 1587 | $\nu$(C=N) |
| 1569 | 1566 | 1566 | 1518 | NA | 1571 | $\nu$(C=C) |
| 1525 | 1530 | 1530 | | 1525 | 1523 | $\delta$(N-H) in-plane bending |
| | | | | | | $\nu$(C-N) II amide |

### $^1$H-NMR and $^{13}$C-NMR studies.

$^1$H-NMR and $^{13}$C-NMR of the free ligand, PB9 (A*), and its Pb(II) complexes, PB9/Pb(II) = 1  (B*) and PB9/Pb(II) = 2 (C*), were recorded in $d_6$-DMSO at room temperature (Table 2.1.). A comparison of the spectra shows remarkable differences (figure 2-9)
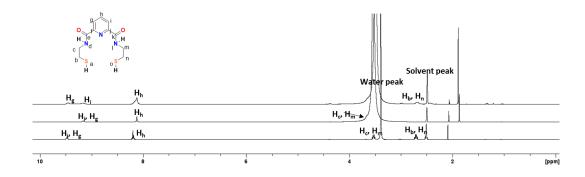


Figure 2-9.  Overlapped $^1$H NMR spectra in $d_6$-DMSO at room temperature for solution A* (free PB9, 20 mM), and in the presence of Pb(II) acetate (B*, C*) molar ratios of PB9:Pb(II) = 1 and 2 respectively at ambient temperature.

$^1$H NMR of PB9 (A*) at ambient temperature in CDCl$_3$ (figure 2.6) shows an assignment for the protons. The single peaks observed for the CH$_2$N and CH$_2$S groups, which are consistent with symmetrical structures in the solution, can be seen when using CDCl$_3$. Whereas when $d_6$-DMSO (figure 2-9) is used, NH and SH protons H-D exchange and hydrogen bond formation can cause signals from NH and SH to disappear from the $^1$H NMR spectrum.

In the presence of Pb(II), some of the signals lost their multiplicity and were observed as broadened peaks making them difficult to assign. This scenario can be

51

evidence of fast exchange in $d_6$-DMSO in the coordination sphere of the complexes or other conformational changes in the system upon complexation with Pb(II) metal. For solutions, B* and C*, the $^1$H- NMR spectra show the downfield shifts of protons for the above B* and C* solutions indicating that the $H_c$ and $H_m$ (covered with water peak) thiolate group is coordinated to the Pb(II) center. The coordination of the pyridine to the metal center is reflected in the shifting of aromatic signals. The signals corresponding to the aromatic pyridine protons $H_i$ and $H_g$ are displaced depicting free A* suggesting the coordination of the Pb(II) to the pyridine nitrogen atom,[106, 125] and their relative positions have been exchanged[126] with associated loss of multiplication and broadening of peaks. Unfortunately, the amide NH protons disappear when using $d_6$-DMSO causing the coordination of Pb(II) to become less evident in the spectra. Further evidence for interactions of pyridine N and Pb is supported by the $^{13}$C - NMR the presence of a Pb-S contact in B* and C* is evident by the de-shielded C attached to S (25 - 29 ppm). Similarly, deshielding was observed for C attached to N indicating the Pb-N contact.

The possibility of oxygen in carbonyl coordination with Pb(II) was not observed, though it scenario in some amides.[127] However, the predicted coordinated compound for Pb(II) with PB9, has enantiomeric and *syn* and *anti* diastereomeric structures with the presence of chiral nitrogens in the molecule.

These Pb(II) compounds are very stable in air, water, and light while also being insoluble in many common solvents/solvent systems (e.g. methanol, ethanol, ethyl acetate, THF, chloroform, etc.) found in the laboratory. $^1$H-NMR spectra were obtained for the solids dissolved in the $d_6$-DMSO but had poorly resolved signals because of their reluctance to solubilize even in coordinating solvents.

**Thermogravimetric, 1ˢᵗ Derivative Thermogravimetric, and DSC Analyses.**

The thermal stabilities of the PB9 and Pb(II) compounds were investigated by thermogravimetric analysis to evaluate their stability at high temperatures. The samples were heated from room temperature to 1000 °C at a rate of 10 °C min$^{-1}$ with a nitrogen purging rate of 20 mL min$^{-1}$. Moreover, the DSC from -90 to 550 °C were analyzed to obtain properties such as melting point temperature, decomposition temperature, enthalpy of decomposition, *etc.* (Overlaid graphs are shown in figure 2-10)

PB9 appears to be free from moisture and solvent, methanol which is also confirmed by FT-IR. No significant mass loss was observed for PB9 up to ~190 °C, and ~225 °C for Pb(II) compounds, indicating that metal compounds are more stable than PB9. The DSC results for Pb(II) compounds show dehydration of water (endothermic peaks) at 89 and 105 °C respectively. DSC also shows endothermic peaks at which is its melting temperature at 191 °C, 234 °C, and 248 °C corresponding to the melting ($T_m$) of PB9, and PB9/Pb(II) 1 and 2 compounds respectively, followed by sharp exothermic peaks at 298 and 283 °C which is associated with some decompositions, reductions, or phase transitions.
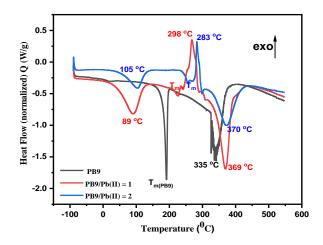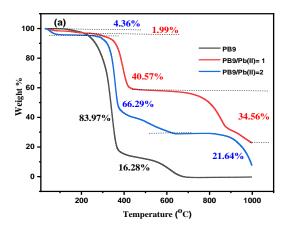
Figure 2-10. The DSC curves of crystals PB9, and lead complexes.

The TGA (figure 2-11a) curve for PB9 has two weight loss steps (decompositions), whereas Pb(II) compounds have four. PB9 does not have evidence for coordination/crystalline water. However, Pb(II) compounds show an initial small mass loss in the range of 40 – 117 °C which is associated with the loss of lattice/coordinated water (solvent) molecules. The DTG curves show corresponding (relatively smaller) peaks in the range of around 40 – 117 °C. The corresponding endothermic peaks were at 89 °C and 105 °C.

The next weight loss in TGA, of 83.97, 66.29, and 40.57% (between 180 and 376) corresponding to temperatures of 340 °C, 369 °C, and 357 °C, in DTA (figure 2-11b) curves show the decomposition. However, the presence of distinct plateaus in the thermogram suggests that when the compound decomposes it produces stable intermediates which can be used for structural feature determination.

54
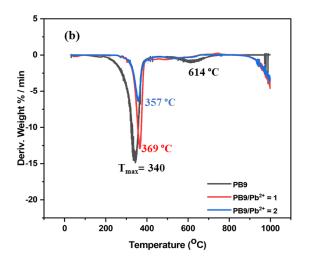
Figure 2-11. The TGA (a) and DTG (b) curves of crystals PB9, and lead complexes.

### Absorption Spectroscopy.

UV–Vis spectra for solutions A-C (prepared according to table 2.1 after dilution) shows in Figure 2-12. These absorption spectra were taken at room temperature for PB9 (solution A) in the aprotic solvent, DMSO. The PB9 spectrum shows transitions due to $\pi$ $\rightarrow\pi^*$ and $n \rightarrow \pi^*$.[128] In the presence of Pb(II) for both solutions B and C, electronic absorption spectra show two bands. An intense absorption at $\lambda_{max}$ = 274 nm ($\varepsilon$= 3199 M$^{-1}$

cm$^{-1}$) and a less intense peak at ~327 nm (B ($\varepsilon$=960 M$^{-1}$ cm$^{-1}$) C ($\varepsilon$= 1344)). These transitions contain both ligand-to-metal charge transfer LMCT (S$^-$ 3s $\rightarrow$ Pb$^{2+}$ 6p)[129] and intraatomic (Pb$^{2+}$ 6s $\rightarrow$ Pb$^{2+}$ 6p) transitions character (for Pb in $O_h$: $a_{1g}^{*}{}^{2} \rightarrow a_{1g}^{*}{}^{1} t_{1u}^{*}{}^{1}$.[130, 131] The two solutions appear yellow in color, which arises from relativistic effects.[132]
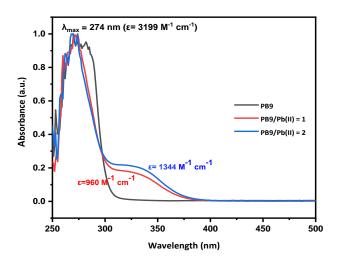


Figure 2-12. UV- vis spectra of PB9Pb(II) solutions A-C with $C_{Pb(II)}$ = 10 mM and mole ratios PB9/Pb(II) = 1.0 (B), and 2.0 (C) compared with free PB9 (A) in DMSO.

**Results of Pb(II) stoichiometry, removal, and leachate of Pb(II) as determined by ICP-OES.**

To examine the Pb(II) leachability (table 2-4) and subsequent stability of the metal complexes,  milliliter aliquots of the solutions were transferred by syringe into tubes after 3, 7, and 10 days for metal concentration measurements. Metal concentrations of the Pb solutions were measured using ICP-OES.  The influence of experimental parameters such as contact time, temperature, ligand dosage, and pH of the medium was studied.

Table 2-4. Results of Leaching studies.

| pH | Concentration/ppm | | |
|---|---|---|---|
| | 3d | 7 d | 10 d |
| 6 | 0.02 | 0.05 | 0.05 |
| 7 | 0.01 | 0.04 | 0.06 |

The highest Pb(II) removal was obtained at pH of 6 and 7, therefore the leaching was checked at pH 6 and 7 for PB9/Pb(II)= 1 compound (with 6.88 mg of PB9). The resulting extracts at pH of 6 and 7 exhibit very negligible Pb(II) content showing that PB9 is exceptionally stable, and leaching is negligible over the studied pH.

**Effects of temperature on removal of Pb(II).**

To study the influence of temperature on Pb(II) removal by PB9, the following temperatures were selected. 10, 20, 30, 40, and 50 °C for PB9/Pb(II)= 1 and 2 complexes are shown in Figure 2-13. It reveals that an increase in the temperature causes a slight increase in the metal removal, suggesting that the complexation of Pb(II) to PB9 is an endothermic process. For both PB9/Pb(II) = 1:1 and 2:1 stoichiometry was carried out under the conditions of a pH~6 and the quantity of PB9 used was 6.88 mg and 13.76 mg respectively depending on the stoichiometric ratio stirring for 6 hours. The residual Pb(II) concentration was measured using ICP-OES.
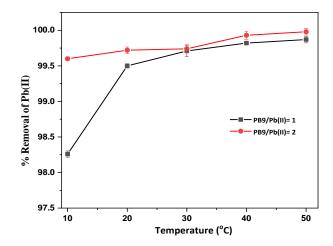
Figure 2-13. Removal % versus temperature (°C) using the model Pb(II) solution with a concentration of 50.0 ppm.

**Nature of interaction of PB9 with Pb(II).**

The thermodynamic parameters $\Delta H$ ($\Delta H$= slope X $R$) and $\Delta S$ ($\Delta S$ = intercept X $R$) were determined graphically from the Van't Hoff plots in Figure 2-14. The values of these parameters are reported in table 2-5. It is assumed that $\Delta H°$, $\Delta S°$ do not significantly change over the temperature range tested.
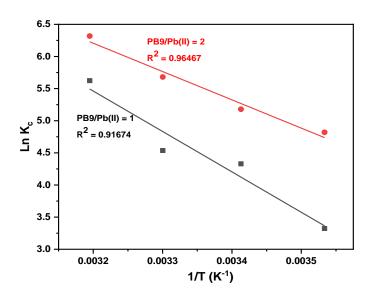
Figure 2-14. Van't Hoff plot.

As shown in Figure 2-14 and table 2-5, the positive values of $\Delta H$ for the two compounds confirmed that the adsorption of Pb(II) by PB9 is an endothermic process. It is also can be inferred that the formation of metal compounds is driven by entropy due to increasing chelation, and giving negative Gibbs free energy values, as the temperature increases.

Table 2-5. Thermodynamic parameters for Pb(II) removal by PB9.

| Material type | $\Delta H$ (kJ/ mol) | $\Delta S$ (kJ/mol K$^{-1}$) | $R^2$ | $\Delta G$(KJ/mol) | | |
|---|---|---|---|---|---|---|
| | | | | 25 °C | 40 °C | 50 °C |
| PB9/Pb(II)= 1 | 52.23 | 0.21 | 0.91674 | -10.35 | -13.50 | -15.60 |
| PB9/Pb(II)= 2 | 36.62 | 0.17 | 0.96467 | -14.04 | -16.59 | -18.29 |

**Effects of reaction time on Pb(II) removal**.

The effect of contact time for both PB9/Pb(II) = 1:1 and 2:1 stoichiometry was carried out under the conditions of a pH~6 and the quantity of PB9 used was 6.88 mg and 13.76 mg respectively depending on the stoichiometric ratio. Figure 2-15 reveals a shape characterized by a sharp increase in both stoichiometries by PB9 during the first minutes of contact between Pb(II) solution and PB9 from an initial 50.00 ppm to 0.30 ppm and 0.25 ppm, respectively. Thus, removal of > 99% within the first 15 min was achieved, followed by equilibrium. The necessary time to equilibrium is only about 15 minutes, after which no notable change was observed after stirring for 10 h.
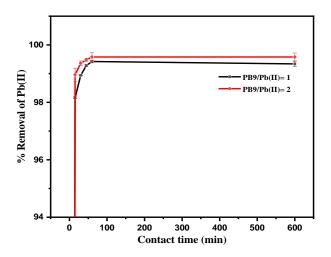


Figure 2-15. Effect on the removal of Pb(II) on the contact time of 50 ppm free Pb(II) solution at 1:1 and 2:1 stoichiometry of PB9/Pb(II).

**Effects of pH on Pb(II) removal.**

The effect of pH was studied after adding 6.88 mg and 13.76 mg for PB9/Pb(II) = 1 and 2, respectively, into 100 mL of 50 ppm Pb(II) solution at pH ranges of 2-8 at 298 K for 300 minutes. Free Pb(II) precipitated as white $Pb(OH)_2$ in alkaline solutions, therefore, this study was conducted at pH <8 to prevent the precipitation of metal hydroxide. The Pb(II) concentration of each sample before and after was determined by ICP. According to the analysis of residual Pb(II) in Figure 2-16, the removal of Pb(II) increases as the pH of the solution increases from 2-to 6, reaching its maximum at a pH of 6. The removal of Pb(II) is more than 96% even at lower pH values (pH=2), leading to >99% removal around neutral pHs. This displays that PB9 is suitable for the removal of Pb(II) in a wide range of acidic pH values.
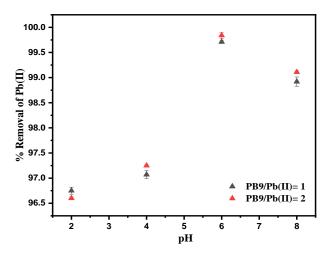


Figure 2-16. Effect on the removal of Pb(II) on the initial pH value of 50 ppm free Pb(II) solution at 1:1 and 2:1 stoichiometry of PB9/Pb(II).

**ESI-Mass Spectroscopy.**

ESI-mass spectrometry was used for the crystals of PB9 and crude metal samples to study the possible composition of Pb(II)- PB9. The ESI-MS of PB9 (Figure 2-17) shows $m/z$ (amu)= 286.0682 for the protonated $[PB9 + H^+]^+$ , $m/z$ (amu)= 308 $[PB9 + H^+ + Na^+]^+$
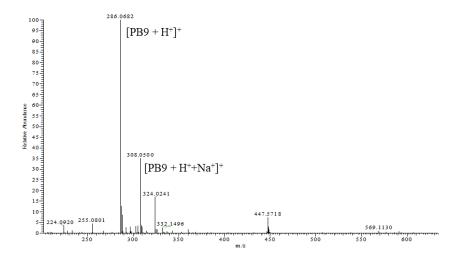


Figure 2-17. ESI-MS spectrum for 1 in positive ion mode.

For metal crude samples, the ESI-MS spectra exhibited only free PB9 with identical $m/z$ (amu) of 286.06. This indicates that metal compounds did not survive during the ESI ionization process. The positive ion mode for PB9/Pb(II) = 2 is shown in Figure 2-18 with free PB9 observed with no further evidence of Pb complexation.
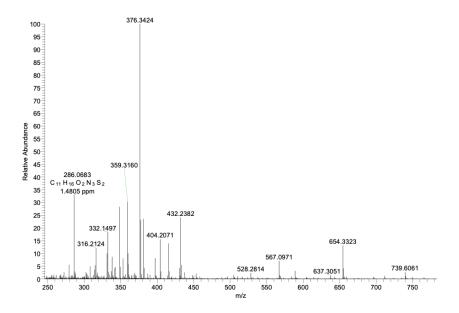
Figure 2-18. ESI-MS of PB9/Pb(II)= 2 in positive ion mode (free PB9 labeled).

Negative ion mode investigations were completed with and without NaOH. While the negative ion mode does produce some signals with Pb labels, metal compounds were not observed in the negative ion mode.
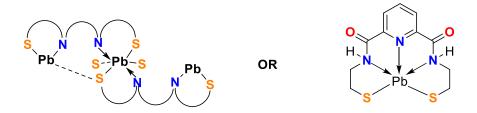


Figure 2-19. Possible oligomeric and predicted molecular structure for PB9/Pb(II).

The predicted molecular structure for PB9/Pb(II) compound is given in Figure 2-19. However, The amorphous XRD, broad melting point and insolubility of the Pb(II) compounds in common laboratory solvents and solvent systems show an oligomeric or polymeric nature.

A (collaborated) computational study was conducted to gain further insight into possible geometry PB9/Pb(II). DFT studies were carried out to explore the solvation of PB9/Pb(II) in methanol. The intrinsic free energy of solvation of PB9-Pb(II), $\Delta G_s^*$ is predicted to be −0.52 eV (−50.17 kJ/mol) via the following equation.

$$\Delta G_s^* = G_{soln}(R_l) - G_{gas}(R_g)$$

where, $R_l$ and $R_g$ are the respective solution- and gas-phase geometries and $G_{soln}(R_l)$ and $G_{gas}(R_g)$ are the respective free energies of the intermediate in the solution and gas phase; the '*' indicates quantities computed at standard states in solution at 1 mol $L^{-1}$. The intrinsic free energy of solvation of −0.52 eV suggests that the PB9-Pb(II) is stable in methanol.

$(CH_3COO)_2Pb_{(g)} + PB9_{(g)} \longrightarrow 2(CH_3COO)^-_{(g)} + PB9\text{-}Pb_{(g)}$

$\Delta G_s^* = -0.64$ eV $\qquad \Delta G_s^* = -0.52$ eV

$(CH_3COO)_2Pb_{(aq.)} + PB9_{(aq.)} \longrightarrow 2(CH_3COO)^-_{(aq.)} + PB9\text{-}Pb_{(aq.)}$

Scheme 2-2. Thermodynamic cycle depicting the intrinsic solvation free energy of PB9 and PB9/Pb(II).
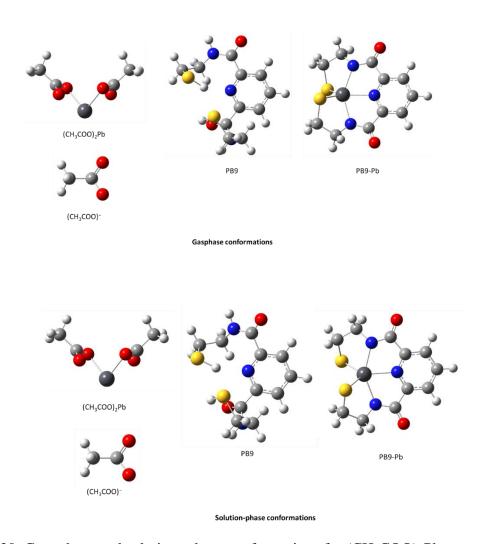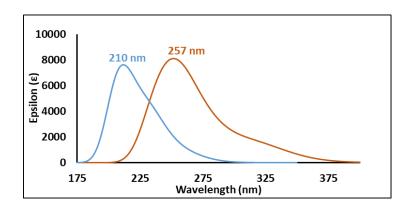
Figure 2-20. Gas- phase and solution- phase conformations for $(CH_3COO)_2Pb$, (CH3COO)-, PB9 and PB9/Pb(II) = 1 according to $\omega$B97XD/6-31G(d,p)/LANL2DZ level of theory.

The simulated UV-vis spectra for PB9 and PB9/Pb in methanol are shown in Figure 2-21, where the shifts in wavelength from PB9 to PB9/Pb(II)=1 are in good agreement with the experimental UV-vis spectra. Thus, the predicted structure for molecular PB9/Pb(II) is a possibility.
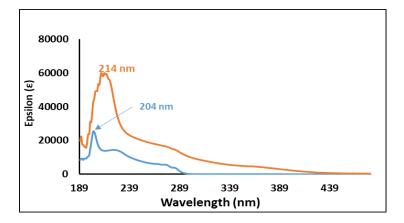
Figure 2-21. UV-vis spectra (a) simulated according to ωB97XD/6-31G(d,p)/LANL2DZ level of theory, and (b) obtained for PB9 (50 µM), and PB9/Pb(II)= 1 in methanol.

The simulated UV-Vis spectra from the TD-DFT calculations and the visualization of natural transition orbitals (NTOs) confirm the transitions seen in the experimental UV-vis. Two distinct transitions are observed for both PB9 and PB9-Pb in methanol as shown in the figures below.
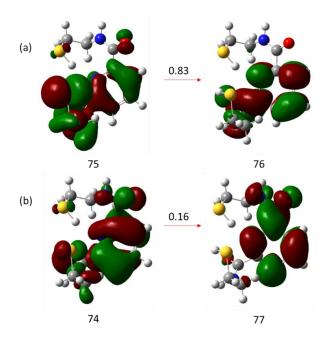
Figure 2-22. PB9 NTOs indicating the (a) primary and (b) secondary transitions according to ωB97XD/6-31G(d,p)/LANL2DZ level of theory



Figure 2-23. PB9-Pb NTOs indicating the (a) primary and (b) secondary transitions according to ωB97XD/6-31G(d,p)/LANL2DZ level of theory

From the NTOs for PB9 (Figure 2-22), it can be seen that the primary transition from structures 75 to 76 corresponds to the $\pi \rightarrow \pi^*$ transition and a second transition from 74 to 77 is associated with n $\rightarrow \pi^*$ observed in the experimental UV-Vis. For the case of PB9-Pb (Figure 2-23), the NTOs show a ligand-to-metal charge transfer in both primary and secondary transitions thus confirming the experimental observations.

## 2.5 Conclusion.

In summary, PB9 can be used as a complexing agent for Pb(II) in aqueous solutions. Notably, the complexation process is fast, with equilibrium reached at 15 minutes, and negligible leaching noted thereafter. It was also shown that the dependence of the residual Pb(II) in the solution on the molar ratio 1:1 and 2:1 is almost unchanged. Advantages of PB9 over other thiol ligands include ease of synthesis and no disulfide formation. PB9/Pb(II) compounds were characterized in solution and solid-state, with a possible structure evaluation. Nevertheless, the solids consisting of the same coordination even with different stoichiometric ratios were confirmed by elemental analysis. The existence of a cyclic oligomeric $(PB9)_4(Pb)_4$ or polymer $(PB9)_\infty(Pb)_\infty$ structure is evident by broad melting point, insolubility in most common solvents, and amorphous powder XRD. However, computational study depicts the possibility of molecular structure to be relatively stable in a dielectric medium of methanol. A higher concentration of PB9 may be required to achieve the EPA limit for drinking water of 15 ppb.

CHAPTER 3. PYRIDINE- FUNCTIONALIZED PB9 AS SENSITIVE AND SELECTIVE FLUORESCENT SENSOR FOR FE(III) ION

## 3.1 Introduction

The pollution due to heavy metals and associated impacts are increased due to industrial and development activities. Iron is a heavy metal that is an important component of biological systems such as oxygen transport, a cofactor in enzyme reactions, and the electron transport chain. The deficiency of $Fe^{3+}$ causes liver damage, diabetes, Parkinson's disease, and cancer.[49] However, excessive $Fe^{3+}$ levels can cause oxidative stress and neurogenerative disease.[50] Therefore, it is important to regulate $Fe^{3+}$ levels in environmental systems. The maximum allowance level of $Fe^{3+}$ in drinking water by the Environmental Protection Agency (EPA) is 0.3 ppm (5.4 µM).[51]

## 3.2 Importance of Detecting Fe(III)

The detection of potentially hazardous metals in ecosystems, which may affect human health, has driven work on fluorescent probes with "on/off" mechanisms recently.[2] Electrochemical, biochemical, and ion-exchange methods prove to be too difficult, expensive, time-consuming or involve extensive pre-treatment. On the other hand, the fluorescent method is a very sensitive, selective, cost-effective, and versatile method that offers detection of guest species. This technique is frequently used in process control, food analysis, environmental monitoring, bio-medicinal science, and many more fields owing to its simple, low cost, that is both selective and highly sensitive.[73]

## 3.3    The sensors

The sensors generally can be classified in many ways, however, the classification owing to the principle of operation of the transducer are classified into two main groups "physical" and "chemical" sensors. This is further subdivided into optical, electrochemical, mass sensitive, and heat sensitive. Also, the physical sensors into magnetic, thermometric, pressure, force, and electrical. Moreover, as having reversible or non-reversible concerning their applications or sizes.

### 3.3.1    The Fluorescent chemosensors

A fluorescent chemosensor is capable of changing fluorescence properties in response to the surrounding medium or through specific molecular recognition events.[60] They usually measure the change in photophysical properties namely fluorescence intensity, the shift in emission spectra, and the lifetime of molecules interacting with an analyte.    These analytes could be cations, anions, or even neutral molecules. These chemosensors often have specific binding and selectivity to the desired analyte in the presence of other coexisting analytes, their toxicity should be minimized, and should possess a desirable solubility in the desired medium. These 'metal sensors' are capable of responding to the presence of a heavy metal ion reversibly and continuously. Most of them bind with the metal ion irreversibly or only at low or high pH so they cannot be used for continuous sensing at near-neutral pH. Upon binding with the metal ion, most indicators change color, with one band appearing as another disappears, rather than an intensity change of one single band leading to changes in the initial ligand.

Here, the phenomenon called fluorescence quenching refers to the process of decreasing the fluorescence intensity of a given compound, the fluorophore, through

interaction with a specific chemical or physical agent, the quencher. This is frequently used in fluorescent chemical sensors, where a small trace of a specific analyte is revealed by a decrease in light emitted by the sensing material.[133, 134] The nature of the quenching effect is in two types: dynamic and static quenching. Dynamic quenching occurs due to collisional deactivation while the binding and formation of a stable non-fluorescent complex between the fluorophore and quencher are static quenching. Importantly, static quenching leads to a linear increase in quencher concentration as described by the Stern-Volmer equation.

### 3.3.2 Pyridine- Thiol as chemosensors

It is known that pyridine $\pi$-conjugated derivatives utilize their lone pair electrons to bind heavy metal atoms to act as sensors.[73, 135] Thus, the Intramolecular Charge Transfer (ICT) band can be tuned through modification of the pyridine $\pi$-conjugated derivative PB9. Spectroscopic responses lead to the use of this as a chemosensor for metal identification. Heavy metal ions are known to quench fluorescence emission via enhanced spin−orbit coupling or energy or electron transfer.[73] It is known that most fluorophores exhibit quenching upon the addition of paramagnetic transition metal ions [39, 136] while some report amplification. [80] One of the most important signaling mechanisms is Chelation Enhanced Fluorescent Quenching (CHEQ) appears due to the presence of empty or half-filled d-orbitals of appropriate energy, transition metals like $Fe^{3+}$, $Cu^{2+}$, $Co^{2+}$, $Ni^{2+}$, etc.[57] These can cause quenching of the fluorescence intensity of the fluorophore through the transfer of energy. This phenomenon is observed frequently in many metal complexes, due to half-filled electrons of metal ions strongly interacting with $\pi$- electrons of the fluorophore and

providing a pathway for Intersystem Crossing (ISC) from the energy of singlet excited states of the fluorophore to the states of higher multiplicity.

A pyridine-2,6-dicarboxamide creates an $N_3$ pincer cavity via two five-membered chelate rings between $N_{pyridine}$ and $N_{amide}$ groups, involving two anionic σ-donating groups $N_{amide}$ groups. These favorable properties not only result in the formation of stable coordination complexes, but also endows such ligands with the stabilization in their higher oxidation states, and the possibility of introducing appended functional groups. This helps either introduction of protecting groups, creating either sterically hindrance groups or secondary coordination environment adjacent to the metal ion coordinated within the $N_3$ pincer cavity.[74-76] Following are a few examples of pyridine-2,6-dicarboxamide scaffold-based sensors known today, used for sensing $Fe^{3+}$, $Pb^{2+}$, $Cu^{2+}$, Figure 3-1.



Figure 3-1. Pyridine-2,6-dicarboxamide scaffold-based chemosensors, drawn with ChemDraw (a)[77], (b)[79], (c)[137]

The fluorescence active sensor shown in (Figure 3-1a) becomes fluorescent inactive upon the binding of $Fe^{3+}$ in THF. Showing the 1:1 binding mode for ligand: $Fe^{3+}$ and an association constant ($K_a$) of $3.31 \times 10^3 \, M^{-1}$.[77] Whereas the sensor (figure 3-1b) is capable of detecting both $Pb^{2+}$ and $Cu^{2+}$ with an association constant of $5.65X10^8 \, M^{-2}$ and $8.89X10^3$ $M^{-1}$ respectively, with a Limit of Detection (LOD) of $2.31 \times 10^{-6}$ M and $1.49 \times 10^{-6}$ M.[79] And probe (Figure 3-1c) is used of sulfide and gaseous $H_2S$.[137]

Sensors for typical transition metals like $Fe^{3+}$ are scarce, as $Fe^{3+}$ is a well-known fluorescence quencher due to its paramagnetic nature. Therefore, the development of rapid, accurate, and feasible detection methods is significantly important. The pyridine-based thiol molecule; PB9 probe is having an excellent spectroscopic properties of high stability to light, favorable absorption and emission wavelength, high quantum yield, and large extinction coefficients. It has recently developed a pyridine-based thiol ligand for colorimetric chemosensors for ferric ion detection in DMSO. PB9 was found to function as an excellent $Fe^{3+}$ sensor, while other common metals, particularly other transition metals, alkalis, and alkaline earth metals produce minimal spectral change. We will discuss their synthesis, characterization, and optical properties of them as the discussion progresses.

## 3.4   EXPERIMENTAL

### 3.4.1   Materials and Instruments

All the materials for synthesis including cysteamine, triethylamine, and 2,6-pyridinediacid dichloride were purchased from commercial suppliers and used without further purification. The metal salts were received from commercial sources.  Electronic

UV-Vis absorption spectra were measured at room temperature using a UV- Vis Agilent spectrophotometer. 2 mL samples were loaded into 1 cm quartz cells; DMSO was used as the blank. Fluorescence measurements were taken at excitation provided at 274 nm, and emission was integrated from 284 to 524 nm with excitation and emission slit widths of both 15 nm and scan speed 200 nm/min. All pH measurements were made with a Mettler Toledo.

### 3.4.2 Solution preparations for UV Absorption and Emission Studies

The stock solution of metals 750 uM and 75 uM of PB9 were prepared in DMSO. Cationic metal salt nitrates; $Cd(NO_3)_2$, $Pb(NO_3)_2$ or chlorides; $NiCl_2$, $CrCl_3$, $CoCl_2$, $FeCl_2$, $FeCl_3$, $CuCl_2$, $BaCl_2$, $HgCl_2$, $SnCl_2$, $ZnCl_2$, $AgCl$ in DMSO were used. Fluorescence and UV absorption studies were performed using a 50 µM solution of the PB9 and appropriate amounts of analytes. The solutions were shaken for half a minute after each addition and allowed to stand for 3 minutes before measuring the fluorescence. All the measurements were carried out at ambient temperature.

### 3.4.3 Measurement procedure for metal ion sensing. [138]

The Benesi-Hildebrand equation[46] (1) was used to calculate the binding constants:

$$\left(\frac{1}{I-I_o}\right) = \frac{1}{\{K(I_{max}-I_o)[M^{x+}]^n\}} + \left(\frac{1}{[I_{max}-I_o]}\right) \qquad (1)$$

where $I_0$ is the fluorescence intensity of the sensor in the absence of metal (guest), $I$ is the fluorescence intensity upon the addition of the guest, $I_{max}$ is the fluorescence in the presence of added $[M^{x+}]_{max}$. And $K$ is the association constant. The $\frac{1}{I-I_o}$ was plotted against 1/ [M] and the association constant (K) was obtained by the ratio intercept/slope.

### 3.4.4   The detection limit

The detection limit was calculated based on fluorescence titration according to the literature.[139] Detection limit was obtained by the equation Detection limit $= \frac{3\sigma}{k}$ ; where $\sigma$ is the standard deviation in the absence of metal cation and determined by ten blank replicate measurements of PB9, $k$ is the slope obtained from plotting the fluorescence intensity *versus* metal ion concentration. The fluorescent emission was taken three times at each point to determine the standard deviation.

### 3.4.5   Quenching efficiency

The quenching/enhancing efficiency was calculated by Stern- Volmer constants.

$$\frac{I_o}{I} = 1 + K_{SV}[Q] \tag{2}$$

Where; $I_0$ is the fluorescence intensity in the absence of a quencher and $I$ is the fluorescence intensity in the presence of a quencher. $[Q]$ is the quencher concentration $K_{SV}$ is the Stern- Volmer constant for complex formation. Which is the slope of the curve.

### 3.5   Results and Discussion

#### Colorimetric detection of Fe(III) by the probe PB9

The colorimetric behavior of the PB9 probe in DMSO was studied. The binding properties of PB9, with a variety of cations, were investigated as shown in Figure 3-2a. In the absence of any metal ions, PB9 shows a signal at 274 nm ($\varepsilon$= 3199 $M^{-1}$ $cm^{-1}$) showing typical aromatic amino acid transition $\pi \rightarrow \pi^*$ and n$\rightarrow \pi^*$. There is no evidence for a

peptide bond around 220 nm.[140,79] However, after the addition of Fe(III) a drastic change

in the absorption spectrum was experienced, while no significant changes were observed

for the other cations used in the study.
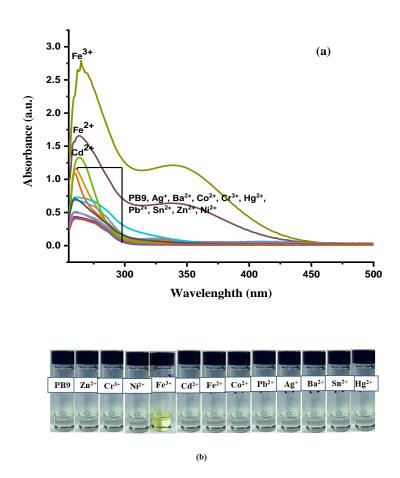


Figure 3-2. (a) UV-absorbance spectra of PB9 (50 μM) in the presence of 250 μM metal ions; (b) color changes of PB9 (50 μM) upon addition of various cations (5 equiv.) in DMSO solution.

Moreover, colorimetric sensing by the naked eye is a concise way to evaluate the

selectivity of probe PB9 to different cations. Figure 3-2b shows that upon the addition of

5 equiv. of Fe(III) to PB9, a significant color change from colorless to yellow occurred in

DMSO solution at room temperature. Whereas no remarkable changes were found with other tested metal ions. The visual color change can be used for the "naked eye" detection of Fe(III) in DMSO. Notably, the interaction of PB9 with Fe(III) resulted in a broad absorption band reaching the visible region leading to a color change from colorless to yellow indicating the sensing ability of PB9 for Fe(III) ions. It can be inferred that Fe(III) binds to PB9 in structurally preferred orientation as a receptive site.

**UV- vis titration and binding stoichiometry.**

UV-Vis study was utilized to investigate the interaction of Fe(III) with PB9. With the addition of different concentrations (0- 80 µM) of Fe(III), a new absorption band at 350 nm appeared (Figure 3-3). The intensity progressively increased with the gradual addition of Fe(III). Accordingly, the absorption variations of PB9 can be ascribed to a ligand to metal charge transfer (LMCT) transition.
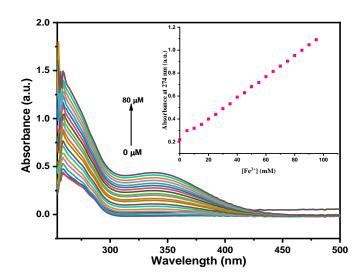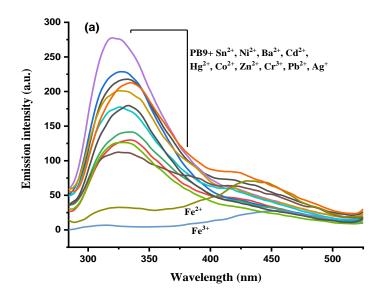


Figure 3-3. UV titrations of PB9 (50 µM) in the presence of varying Fe(III) (0- 80 µM).

**Fluorogenic detection of Fe(III) by the sensor PB9.**

To study the photophysical behavior of PB9 toward metal ions, the fluorescence response of PB9 for various metal ions $Sn^{2+}$, $Pb^{2+}$, $Ni^{2+}$, $Ba^{2+}$, $Cd^{2+}$, $Hg^{2+}$, $Co^{2+}$, $Cu^{2+}$ and $Zn^{2+}$ ions (0–5 equiv) was investigated (Figure 3-4a). The fluorescence spectrum of PB9 exhibits a strong emission at 323 nm when excited at 274 nm.

It can be found that the addition of $Ni^{2+}$ and $Hg^{2+}$ enhanced the fluorescence intensity at 323 nm however, $Cu^{2+}$, $Ag^+$, $Ba^{2+}$, $Cd^{2+}$ $Co^{2+}$, $Sn^{2+}$, $Cr^{3+}$ $Pb^{2+}$, $Fe^{2+}$ reduce the fluorescence intensity of PB9. The most notable decrease is for Fe(III) which quenches the emission intensity by about 400-fold (Figure 3-4b), which was in good agreement with findings of absorbance. It was also noticed that some "soft" metal ions such as $Hg^{2+}$, $Pb^{2+}$, and $Cd^{2+}$ hardly caused any fluorescence change and the bivalent state of iron ($Fe^{2+}$) does not significantly change the emission and UV-Vis profile of PB9. Under the ultraviolet (UV) at 365 nm, the Fe(III) ion presented fluorescence quenching showing an obvious "turn off".
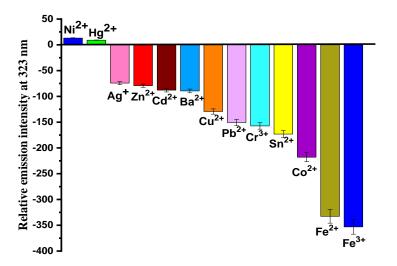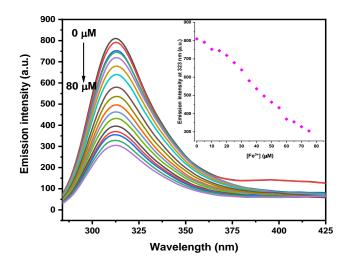
Figure 3-4. Emission spectra of probe PB9 (50 µM) in DMSO and after interaction with metal ions (250 µM). (b) Bar diagram representing the change in emission intensity at 323 nm of PB9 (50 µM) after the addition of metal ions (250 µM).

It is inferred that the fluorescence spectral changes for Fe(III) are due to the compatibility of ionic radii and the cavity creates an exact fitting of the guest analyte

leading to the strong interaction between host PB9 and guest Fe(III). The quenching behavior may arise from the paramagnetic nature of the Fe(III) ion. This promotes the spin-orbit interactions and consequently the intersystem crossing (ISC), leading to the chelation-enhanced quenching (CHEQ) effect.[141] Along with this, as well as the visually detectable changes in solution, were instantaneous upon binding to Fe(III) making PB9 a potential candidate for sensing device.

Similarly, the addition of 0- 1.5 equiv. of Fe(III) to a solution of PB9 (50 µM), resulting as shown in Figure 3-5a, in a quenching of fluorescence at 323 nm with an increasing Fe(III) amount with the quenching efficiency of 99% [$(I_O$-$I$/$I_O$ X 100]. The formally forbidden ISC becomes faster due to the presence of paramagnetic Fe(III) in the proximity of fluorophore. Sensor PB9 shows the CHEQ effect with Fe(III), implying the interruption of the ICT mechanism. This "paramagnetic effect" lead to the ISC by excitation, from $S_1$ to $T_1$ state of the fluorophore deactivated by the non-radiative process. This indicates that PB9 has high selectivity and excellent sensitivity for Fe(III) in DMSO.
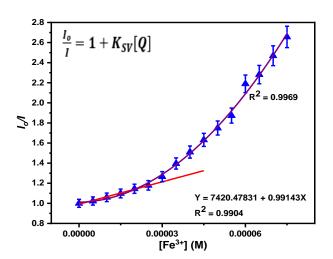
Figure 3-5. Change in emission intensity with the number of equivalents (0-1.5) of Fe(III) ion for PB9 (a) PB9 (50 µM) in DMSO, Inset: Change in emission intensity at 323 nm. (b) Stern-Volmer plot for the fluorescence quenching of PB9 (50 µM) in the presence of Fe(III).

In the concentration range studied, the quenching efficiency was quantitatively evaluated and interpreted by calculating Stern-Volmer constants ($K_{sv}$).[71] In the Stern-Volmer equation(2). $K_{SV}$ is the Stern-Völmer constant, which measures the efficiency of

quenching. According to the Stern-Volmer plot (Figure 3-5b), $K_{SV}$ of PB9 for Fe(III) was calculated as $(7.42 \pm 0.03) \times 10^3 \text{ M}^{-1}$. According to the Stern- Volmer plot, a linear growth at lower concentrations and a positive deviation (i.e., upward curvature) at higher values of Fe(III) concentration can be seen. The additional facts such as absorption spectra (Figure 3-7) support the static quenching originating from the formation of the stable ground-state complex. Thus, charge transfer from the excited PB9 to the electron-withdrawing Fe(III) ion would be the origin of the observed fluorescence quenching.[57] Even though dynamic quenching can be determined by lifetime measurements, the unavailability of a laser lamp precluded this study.
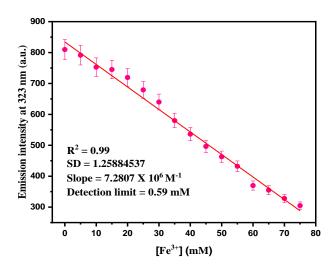


Figure 3-6. Determination of detection limit of PB9 in DMSO towards Fe(III) ion (concentration was linear from 0- 80 µM) ($\lambda_{ex}$= 274 nm, $\lambda_{em}$= 323 nm).

The lowest detection limit of PB9 for Fe(III) (using data available from fluorescence titration) was estimated in Figure 3-6, using equation 2 to be 0.59 µM. It was remarkable that this detection limit for Fe(III) is acceptable within the government

restrictions on the levels of drinking water (0.3 ppm). However, this study was conducted in DMSO, future research shall conduct in aqueous conditions.
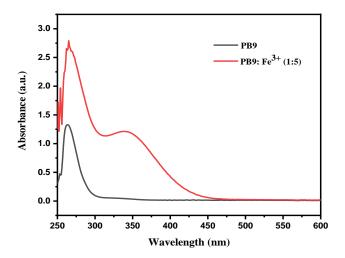


Figure 3-7. Changes in the absorption spectrum of receptor PB9 (50 µM) upon addition of Fe(III) (250 µM) in DMSO.

**Determination of binding constant and association constants.**

The binding stoichiometry for Fe(III) ions analysis was based on Job's plots and the association constant was calculated according to the Benesi- Hildebrand plots using fluorescence measurements.

The binding interactions between PB9 and Fe(III) were evaluated using Job's plot experiment. Various mole fractions of Fe(III), 0.1, 0.2, 0.3, 0.4, 0.5, 0.6, 0.7, 0.8, 0.9 and 1.0 were prepared and their fluorescence intensities were measured (Figure 3-8). The minimum fluorescence emissions intensity was identified at 323 nm when the mole fraction of Fe(III) reached 0.5, which is indicative of a 1:1 stoichiometric complex between PB9 and Fe(III).
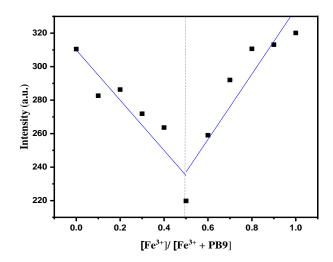
Figure 3-8. Job's plot indicates a 1:1 stoichiometry for PB9 and Fe(III), (the total concentration of PB9 and Fe(III) kept constant at 100 μM).

The association constant K of PB9 with Fe(III) was determined by the Benesi–Hildebrand equation and yielded the apparent binding constant value as $9.537 \times 10^3$ $M^{-1}$ ($R^2 = 0.972$) (Figure 3-9).
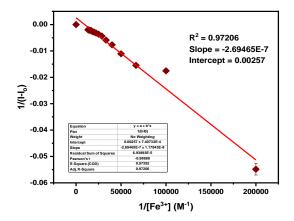


Figure 3-9. Benesi- Hildebrand plot. ($\lambda_{ex}$= 274 nm, $\lambda_{em}$= 323 nm).

**Reversibility of the binding process between sensor PB9 and Fe(III)**.

This was established by adding EDTA to the PB9+ Fe(III) complex (Figure 3-10). This allows Fe(III) to form an even more stable complex Fe-EDTA. After treatment with EDTA, the yellow solution of PB9-Fe(III) turned colorless. The disappearance of the yellow color suggests that the coordination of the sensor with Fe(III) is chemically reversible. Additional EDTA eliminated the color, indicating a complete shift of the equilibrium to the left.
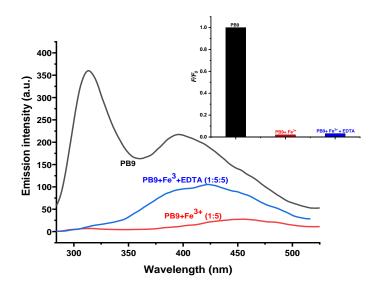


Figure 3-10. Emission spectra of PB9.Fe(III) upon addition of Na$_2$EDTA solution, relative intensities at 323 nm. Inset: relative intensities at 323 nm.

Moreover, the selectivity of PB9 for Fe$^{3+}$ ions was examined by determining the changes in fluorescence intensity in the presence of various interfering metal ions (Figure 3-11). Competitive binding studies were investigated in the presence of Cu$^{2+}$, Zn$^{2+}$, Cd$^{2+}$, Pd$^{2+}$, Ni$^{2+}$, Hg$^{2+}$, Pb$^{2+}$, Co$^{2+}$, Cr$^{3+}$, Sr$^{2+}$, and Mn$^{2+}$. The competitive experiments were conducted in the presence of 250 µM Fe(III) ion mixed with equimolarly of various cations.

The fluorescence quenching shown in the figure demonstrated that PB9 exhibited an excellent selectivity for Fe(III) in 50 µM DMSO media since no significant change was observed in emission spectra upon the addition of 250 µM of other metals. Furthermore, interference-free detection of Fe(III) was achieved in the presence of all other test metal ions.
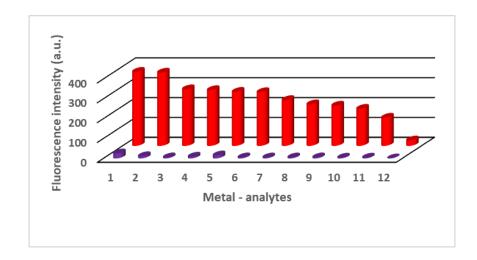


Figure 3-11. Representative bar chart showing fluorescence intensity at $\lambda = 323$ nm for PB9 (50 µM in DMSO), upon addition of 250 µM of metal-analytes (back row). The front row shows the addition of Fe(III). Excitation was provided at 274 nm. (1 = $Ni^{2+}$, 2 = $Hg^{2+}$, 3 = $Ag^{+}$, 4 = $Zn^{2+}$, 5 = $Cd^{2+}$, 6 = $Ba^{2+}$, 7 = $Cu^{2+}$, 8 = $Pb^{2+}$, 9 = $Cr^{3+}$, 10 = $Sn^{2+}$, 11 = $Co^{2+}$, 12 = $Fe^{2+}$.)

## 3.6   Conclusion.

The novel pyridine-based thiol molecule, PB9 acts as a selective and sensitive fluorescent probe for the detection of Fe(III). The Job's plot indicates the molar binding ratio of PB9 to Fe(III) is 1:1 with an apparent association constant of 9.537 x $10^3$ $M^{-1}$. A linear range of 0- 80 µM with a detection limit of 0.59 µM (0.003 ppm) was found. The obtained detection limit was much lower than the maximum allowance limit of Fe(III) (0.3 ppm) regulated by EPA in drinking water. Moreover, a colorimetric response from the PB9

permitted the detection of Fe(III) by the "naked eye" because of the development of yellow color when Fe(III) interacts with PB9 in DMSO. Theoretical Studies comprising Benesi-Hildebrand, Stern- Volmer, and studies such as Job's plots, and detection limits illustrate higher sensing abilities. Stern-Volmer plots suggest that the quenching mechanism is likely to contain both static and dynamic elements
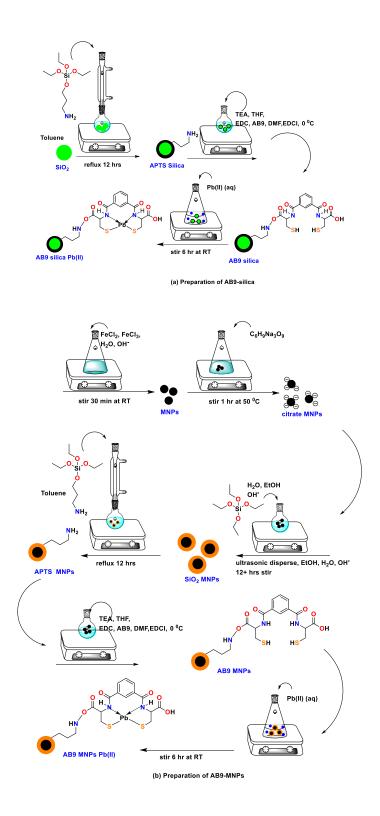
This rationally designed new pyridine scaffold molecule is easily prepared in one step, and we have demonstrated that these compounds could be used as highly effective fluorescent sensors for the sensitive and selective recognition of Fe(III) with fast response and regenerative action in DMSO. Importantly, this selectivity is suitable for the detection of Fe(III) by simple visual inspection and is retained even in the presence of an excess of other metal ions. Furthermore, we elucidate the mechanism, disclosing that coordination of the Fe(III) destabilizes the electron push-pull system of the sensor in the complexation process and thus results in fluorescence quenching based on the ICT signaling mechanism by the CHEQ mechanism. It can be inferred that, in this study, the fluorophore is quenched by both collisions and by complex formation with the quencher as is seen by the characteristic feature of the Stern -Volmer is having the upward curvature (concave towards the y- axis) and absorption spectra. We believe that these conclusions would be potentially useful for monitoring Fe(III) concentrations in a practical system.

CHAPTER 4. **THIOL-FUNCTIONALIZED SILICA (AB9-SILICA) AND MAGNETIC NANOPARTICLES (AB9- MNPS) TO REMOVE PB(II) FROM WATER**

## 4.1 INTRODUCTION

Heightened awareness of dangers posed by the release of heavy metals has increased research into the removal of these materials from the environment.[90] There are several methods for Pb(II) ion removal from the water such as sorbent materials incorporated into nanostructures." However, these materials suffer from the transport of large volumes of water through these materials. Ideally, an easily dispersible sorbent with a larger surface area would be very effective in the removal of heavy metals. Currently, the development of an efficient adsorbent with lower cost, high selectivity, and capacity depending on adsorption sites is still a challenge.[142]

In this chapter, effective methods to capture and separate Pb(II) from water utilizing a new sulfhydryl compound appended to the surface of silica (AB9-Silica) and magnetic nanoparticles (AB9-MNPs) are described. This new approach utilizes a synthetic sulfhydryl compound, AB9, with a high affinity for Pb(II) and easy preparation. AB9 (2,2'-(isophthaloybis(azanediyl))bis-3-mercaptopropanoic acid), can make strong covalent Pb-S bonds with Pb(II). AB9 is a derivative of B9, N, N'-bis(2-mercaptoethyl)isophthalamide, which has an established ability to precipitate soft heavy metals such as aqueous Pb, Cd, As and Hg, to below detectable limits (0.05 ppb).[28, 110, 143] Here, the carboxylic acid groups (the origin of "A" in AB9) will be coupled to the terminal amine groups present on the surface of silica and/or MNPs to functionalize both materials for aqueous Pb(II) removal as shown in Scheme 4-1.

Scheme 4-1. Synthetic routes for (a) AB9-silica, (b) AB9-MNP, and Pb(II)  ion removal.

The two forms of AB9 were synthesized according to Scheme 4-1. Magnetite (Fe$_3$O$_4$) was synthesized by co-precipitating Fe(II) and Fe(III) salts treated with NH$_4$OH.[144] The nanoparticles tend to sediment and agglomerate near to Point of Zero Charge (PZC).[145] During this process, the citrate coating on the MNPs reduced agglomeration, altering the PZC. This helps to form monodispersed MNPs by avoiding agglomeration and reducing the surface area to volume ratio at the nanoscale.[146] Subsequently, silica-coated MNPs were prepared using the Stober method, which produces high-quality monodispersed silica nanoparticles with subsequent hydrolysis and subsequently. Here, Tetraethyl orthosilicate (TEOS, Si(OEt)$_4$) is hydrolyzed in alcohol in the presence of ammonia as a catalyst.[85]

The organosilane precursor, silica-coated MNP or commercial silica particles, was then treated with 3-(aminopropyl)triethoxysilane (APTS) allowing further functionalization due to the primary amine present. The advantage of using APTS was its stability towards polymerization reactions,[147] while in this process, toluene allowed reproducible loading.[148] Next step involves the surface stabilization of the APTS-silica and/or APTS-MNP simultaneous attachment to AB9. This thiol is expected to bind with Pb(II) in participating in Pb-S bond formation for Pb(II) removal.

Magnetic nanoparticles have been used in many areas such as drug delivery, catalysis, biomedical applications, separations, and adsorption media. This material can be considered ideal for large-scale production because of its low cost, utilization of -earth-abundant elements, established synthesis, and ease of controlling particle size. Additionally, MNPs offer the ability to magnetically separate them from media after use. Therefore, MNPs of sizes 1-100 nm were used in this project.[149, 150] This material can be considered as an ideal combination of large-scale production and its valuable usage with

low cost, utilization of earth-abundant elements, established synthetic procedures, and simple condition changes to control particle size. Moreover, an added advantage of MNP, over silica is the ability to magnetically isolate the material after use.

This research is a relatively new area that has emerged from AB9 coupled to the surface of functionalized silica and also onto the core-shell magnetite nanoparticles (MNPs). These approaches have been significant because of unique features such as the formation of covalent M-S bonds, stability in aqueous and atmospheric environments, and no initial deactivation of AB9 through the formation of disulfide S-S bonds. These attributes combine with the intrinsic advantages of MNPs comprised of silica and magnetite to result in a lead-removal system that could be scaled up to provide lead-free drinking water to at-risk and expanding global populations.

This work focuses on the preparation and evaluation of AB9-modified magnetic nanoparticles and silica with efficient removal of Pb(II) evaluation of important factors including medium pH, temperature, contact time, adsorbent amount, as well as thermodynamic parameters. Additionally, the easy regeneration of the magnetite nano adsorbents was carried out using diluted HCl at a pH of 2. [151] Thus, this chapter will explore the chemistry, and synthesis of AB9 fabricated magnetite ($Fe_3O_4$) nanoparticles and silica. Moreover, the same experimental procedure was used for the fabrication of AB9 on silica, thus, it is not mentioned in the experimental section.

## 4.2    Experimental

### 4.2.1    Materials

The following reagents and solvents were obtained commercially and used without further purification; L-cysteine hydrochloride, triethylamine, ferrous chloride ($FeCl_2 \cdot 4H_2O$), sodium citrate tribasic dihydrate, tetraethyl orthosilicate (TEOS), ($Na_2$ N-(3-dimethylaminopropyl)-N′-ethylcarbodiimide hydrochloride (EDCI), (3-aminopropyl)triethoxysilane (APTS), sodium chloride (NaCl), sodium nitrate ($NaNO_3$), sodium sulfate ($Na_2SO_4$), sodium bicarbonate ($NaHCO_3$) and isophthaloyl chloride, dithiothreitol from Sigma-Aldrich; ferric chloride ($FeCl_3 \cdot 6H_2O$); Omnitrace hydrochloric acid (HCl), nitric acid ($HNO_3$), and ammonium hydroxide ($NH_4OH$) from EMD; DMSO-$d_6$ (99.9%)

### 4.2.2    Analytical Techniques

Fourier Transform infrared spectroscopy (FT-IR) spectra were performed on samples using a Nicolet 6700 FT-IR spectrometer in the 500- 4000 $cm^{-1}$ range with 2 $cm^{-1}$ resolution. $^1$H NMR of AB9 was produced in DMSO-$d_6$ using tetramethylsilane (TMS) as an internal standard on a Varian INOVA instrument at room temperature at an operating frequency of 399.78 MHz with a pulse of 71.2 deg.  The aqueous concentrations of Pb(II) were determined with an Agilent 5110 SVDV inductively coupled argon plasma optical emission spectrometer (ICP-OES) with the detection limits for lead analyses as Pb, 0.001 mg/L. Melting points were obtained on a MEL-TEMP instrument from Laboratory Devices. Zeta Potential and dynamic light scattering were measured with a Brookhaven ZetaPALS Zeta Potential Analyzer. Zeta Potential measurements were recorded in 4 runs

with 30 read cycles for each measurement. Stock solutions were made with 3 mg of MNP with 20 mL of the pH solutions and sonicated for 5 min before analysis. Magnetic separation was achieved using computer hard drive magnets. Specific Brunauer-Emmett-Teller (BET) and external nanoparticle surface areas were measured by nitrogen adsorption and desorption at 77 K, performed using a Micrometrics Tri-Star instrument, and the average pore size was determined by Barrett-Joyner-Halenda (BJH) model. The total pore volume was evaluated from nitrogen uptake at a relative pressure of 0.97. The elemental analysis (CHNO) was obtained at the Center for Advanced Energy Research Facility at the University of Kentucky. The crystallographic phase was determined by X-ray powder diffraction (XRD) using a Bruker-AXS D8 Discover Diffractometer from 10° to 80° (2θ) with step increments of 0.100° at 25 °C using monochromatized X-ray beam with CuKα radiation (λ = 1.5406 A). Scanning Electron Microscope (SEM) observations were performed on Hitachi S4300 field-emission SEM operated at 10 kV. Sample powders were loaded on double side carbon tape attached to aluminum stages, which were further performed with sputter coating of a thin Au-Pd layer to improve sample electrical conductivity for better SEM imaging quality. Transmission Electron Microscopy (TEM) observations were performed on ThermoScientific F200X TEM operated at 200 kV. A little amount (< 1mg) of sample powders were dispersed into de-ionized water (1 mL) by sonication for 10 minutes, then transferred on thin lacey carbon films supported on copper grids.

### 4.3 Synthesis

### 4.3.1 AB9 Synthesis

Triethylamine (40.15 mL, 29.20 g, 288.90 mmol, TEA) was added slowly to a stirring solution of L-cysteine (35.00 g, 288.90 mmol) in DI water (300 mL) under a flow of nitrogen. After 5 min, isophthaloyl chloride (27.97 g, 137.76 mmol) in THF (300 mL) was added dropwise to the clear stirring reaction mixture. After 12 h of stirring under $N_2$, the solution was extracted with ethyl acetate (100 mL) and the ethyl acetate layer was dried over anhydrous $Na_2SO_4$ before the solvent was removed under vacuum to produce AB9 as a light-yellow solid (24.33 g, 61.5 % yield). IR: 3303 (broad, acid OH and secondary NH), 3063 (m, aromatic C-H), 2931 (m, methylene C-H), 2556 (m, S-H), 1718 (s, acid (C=O)), 1628 (s, amide (C=O)), 1522 (NH); $^1$H-NMR ($d_6$-DMSO, 400 MHz): δ (ppm) ; 2.51 (t, 2H, SH), 2.93 (m, 4H, $CH_2$), 4.55 (m, 4H, CH), 7.63 (t, 1H, $C_6H_4$), 8.06 (d, 2H, $C_6H_4$), 8.41 (s, 1H, $C_6H_4$), 8.90 (d, 2H, NH); $^{13}$C - NMR δ (ppm); 172, 166, 134, 130, 128, 127, 56, 25.

### 4.3.2 Synthesis of Magnetic Nanoparticles (MNP) by Coprecipitation Method

$FeCl_2 \cdot 4H_2O$ (0.994 g, 5 mmol) and $FeCl_3 \cdot 6H_2O$ (2.703 g, 10 mmol) were dissolved in 120 mL of deoxygenated water. 20 mL of $NH_4OH$ was added after complete dissolution. This rapid addition causes the formation of the black precipitate. This solid was stirred for an additional 30 minutes. The resulting magnetite nanoparticles were washed with deoxygenated water and anhydrous methanol five times each to neutralize the alkalinity of the medium. The suspension was separated magnetically and then dried under a vacuum at room temperature. IR: 3500-3000 cm$^{-1}$ (3142 broad, -$H_2O$), 570 cm$^{-1}$ (s, Fe-O); XRD: all Bragg planes indexed to cubic inverse spinel $Fe_3O_4$ ($2^θ$ = 30, 36, 43, 54, 56, 63, 74).

### 4.3.3 Preparation of Citrate Coated Magnetic Nanoparticles (Citrate-MNPs)

$FeCl_2 \cdot 4H_2O$ (0.9941 g, 5 mmol) and $FeCl_3 \cdot 6H_2O$ (2.703 g, 10 mmol) were dissolved in 120 mL of deoxygenated water. After complete dissolution, 20 mL of ammonium hydroxide was added rapidly, precipitating a black solid, and stirred for an additional 30 minutes. After decanting the initial volume 60 mL of 0.1 mM trisodium citrate dihydrate (17.6 mg, 60.0 μmol) was added to the magnetite precipitate and stirred at 50 °C for one hour. The citrate-coated magnetite nanoparticles were washed with deoxygenated water five times and anhydrous methanol five times. The suspension was separated magnetically and dried under vacuum at room temperature for 12 h. IR: 3170 $cm^{-1}$ (broad, $-H_2O$), 1615 $cm^{-1}$ and 1352 $cm^{-1}$ (s, $CO_2^{-1}$).

### 4.3.4 Preparation of Silica Core-Shell Nanoparticles ($SiO_2$-MNPs)

Silica-coated $Fe_3O_4$ nanoparticles were obtained by hydrolysis of tetraethylorthosilicate (TEOS) on the surfaces of the $Fe_3O_4$ nanoparticles. Citrate-coated magnetite (0.5g) was ultrasonically dispersed in a solution containing 240 mL ethanol, 60 mL water, and 5 mL ammonium hydroxide. Tetraethylorthosilicate (0.9 mL, 0.8 g, 7.38 mmol) was added dropwise to the suspension over six hours followed by stirring for 12 h. The coated magnetite nanoparticles were washed successively with deoxygenated water and anhydrous methanol and filtered by magnetic separation, and then vacuum dried at 80 °C for 12h. IR: 3560-2900 $cm^{-1}$(broad, $H_2O$); 1068 $cm^{-1}$ (s, Si-O), 935 $cm^{-1}$ (w, Si-OH), 799 $cm^{-1}$ (w, Si-OH);XRD: broad Bragg peaks for amorphous silica phase occur at 18-20 $2^\theta$ and $2^\theta = 30, 36, 43, 54, 56, 63, 74$ indexed to cubic inverse spinel $Fe_3O_4$;

95

### 4.3.5  Preparation of APTS-SiO₂ Magnetic Nanoparticles (APTS-MNPs)

Amine-functionalized silica-coated magnetite nanoparticles were prepared by condensation of 3-(aminopropyl)triethoxysilane on the silica surface. The silica-coated magnetite nanoparticles (0.500 g) were dispersed into 300 mL of dry toluene under nitrogen protection. 3-(Aminopropyl)triethoxysilane (APTS) (1.1 mL, 1 g, 4.52 mmol) was added dropwise to the mixture and refluxed for 12 h. The free amine-terminated composite was isolated by magnetic filtration, successively washed with toluene followed by anhydrous methanol, and vacuum dried at 80 °C for 12 h. IR: 3600-2700 cm$^{-1}$(broad, H$_2$O); 2981 cm $^{-1}$ (w, sp$^3$ C-H), 2978 cm$^{-1}$, 1554 cm$^{-1}$ (w, N-H scissor), 1033 cm$^{-1}$ (s, Si-O), 808 cm$^{-1}$ (w, Si-OH); 4192021. XRD:  broad Bragg peaks for the amorphous silica phase occur at 18-20 2$^θ$ and 2$^θ$ = 30, 36, 43, 54, 56, 63, and 74 indexed to cubic inverse spinel Fe$_3$O$_4$.

### 4.3.6  Preparation of AB9-MNP

APTS MNP (0.5 g, 0.5785 mmol APTS) were combined with 3 equivalents of triethylamine (175 mg, 0.242 mL, 1.74 mmol) in THF (30mL) and stirred for 1 h. The material was isolated magnetically followed by vacuum drying at room temperature for 6 h. APTS MNP, AB9(225 mg, 0.601 mmol), and 4-(dimethylamino)pyridine (73.31 mg, 0.601 mmol) were combined in DMF (100 mL) at 0 °C under nitrogen. 1-Ethyl-3-(3-dimethylaminopropyl)carbodiimide hydrochloride (185 mg, 0.965 mmol) was slowly added to the mixture and stirred for 6 hours. The material was isolated by magnetic filtration and stirred in neutral water with dithiothreitol (10 mM) for 1 hour. The isolated materials were washed with 200 mL water and 200 mL ethanol and then dried under vacuum at 50 °C for 12 h. IR: 3600-2700 cm$^{-1}$(broad, H$_2$O); 3042 cm $^{-1}$ (w, sp$^3$ C-H), 2556

cm$^{-1}$ (w, S-H), 1737 cm$^{-1}$ (w, acid, (C=O)), 1646 cm$^{-1}$ (m, amide (C=O)) 1217 cm$^{-1}$ (w, N-H scissor), 950 cm$^{-1}$ (w, Si-OH), 852 cm$^{-1}$ (w, Si-OH); XRD: broad Bragg peaks for amorphous silica phase occur at 18-20 $2^{\theta}$ and $2^{\theta}$ = 30, 36, 43, 54, 56, 63, and 74 indexed to cubic inverse spinel Fe$_3$O$_4$.

### 4.3.7   Batch adsorption Experiments

The adsorption capacities of the nanoparticle adsorbents were evaluated under the conditions of various solution pH, dosage (mg), reaction time (t, min), and reaction temperature (T, K). The adsorption studies of Pb(II) ions on raw silica, AB9-silica, raw MNPs, and AB9-MNPs were performed. For the effect of solution pH, a 100 mL solution containing lead (II) ions with initial concentration (C$_o$, 50.0 ppm) was added into the Erlenmeyer flask and then adjusted to the desired pH values with 0.1 M HCl or NaOH solutions. The experimental conditions were fixed in the dosage of 5.0 mg, T= 298 K, and t= 6 h under various pH values of 2-8. The effect of dosages on the adsorption, T= 298 K, t= 6 h, pH= 7, C$_o$= 50 ppm, and V= 100 mL with dosages of 3, 6, 9, 12, 15 mg was used. The amount of Pb(II) adsorbed by a unit mass of adsorbent in the equilibrium state was calculated using the following equation:

$$K_d = \frac{(C_o - C_f)V}{C_f\,M} \quad (1)$$

Where $K_d$(mL/g) is the distribution coefficient, $C_o$ and $C_f$ are the initial and final concentrations in solution (mg L$^{-1}$) of Pb(II) determined by ICP-OES.V is the volume of

solutions (mL) and $M$ (g) the mass (adsorbent dosage) of sorbent applied during the experiment.[152]

## 4.4    Results and Discussion

Characterization of Magnetic Nanoparticles

The $Fe_3O_4$ magnetic nanoparticles were prepared by co-precipitation. The reported reaction for the formation of $Fe_3O_4$ particles is shown in equation 2.[153]

$$Fe^{2+} + 2Fe^{3+} + 8NH_3.H_2O \rightarrow Fe_3O_4 + 8NH_4^+ + 4H_2O \quad (2)$$

The surface morphology was evaluated using SEM for raw (commercial) silica, AB9-Silica, MNPs, and AB9-MNPs and are shown in Figure 4-1. According to the SEM data, the surface of MNPs, silica, and AB9-MNPS shows spherical shapes, while AB9-silica a rough and contains many particles that are irregular in shape and size. However, many agglomerated particles on the surface of these materials could be attributed to nanostructures and magnetic properties, which contribute to a tendency for agglomeration and aggregation. The SEM images show that as-synthesized AB9 functionalized silica and MNP are free of other impurities.
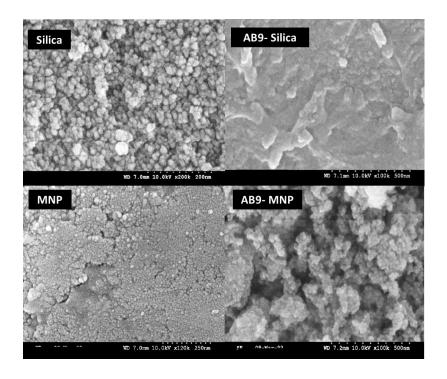
Figure 4-1. Scanning Electron Microscopic (SEM) images of (a) silica, (b) AB9-silica, (c) MNP, (d) AB9-MNP.

Only MNPs and AB9-MNPs were used for TEM, as they showed crystalline nature in powder XRD. The Transmission Electron Microscopy (TEM) for MNPs and AB9-MNPs is shown in Figures 4-2 and 4-3 respectively. The elemental analysis of the prepared MNPs and AB9-MNPs was carried out by using a Scanning Electron Microscopy equipped with Energy-Dispersive X-ray Spectroscopy (EDS) mapping. The sample was analyzed for iron, and oxygen content of MNPs as seen in Figure 4-2, the elements are relatively homogeneously distributed. The ($Fe_3O_4$) MNP were nanometer-sized spherical particles with a typical size of approximately 10–16 nm, in good agreement with the size calculated from the PXRD analysis. The MNPs are agglomerated due to the involvement of the hydroxyl groups in the extract, generating mesopores in the material.
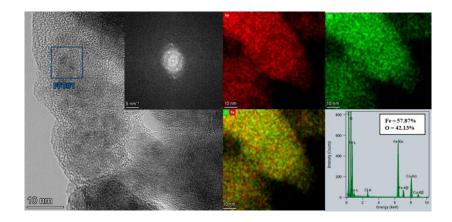
Figure 4-2. Representative (a) TEM image (HR-TEM image of Fast Fourier Transform (FFT) pattern (inset) of MNPs. (b-d) EDS mapping of Fe, and O, (e) EDS spectrum for MNPs.

The following figure (Figure 4-3) shows the TEM and HR-TEM images of AB9-MNPs. This sample was also analyzed towards iron, silica, sulfur, oxygen, and nitrogen content as seen from the figure; all elements are relatively homogeneously distributed for AB9- MNPs.
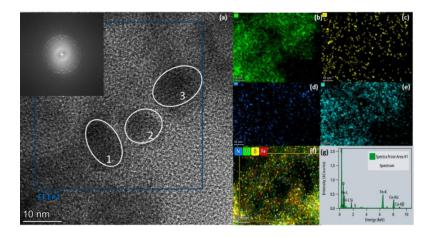


Figure 4-3. Representative (a) TEM image (HR-TEM image of Fast Fourier Transform (FFT) pattern (inset) of AB9-MNPs. (b-f) EDS mapping of O, S, N, Si and obtained (g) EDS spectrum for AB9-MNPs.

In addition, the corresponding HR-TEM, FFT is shown in the insets of Figure. 4-2 and 4.3 display the crystallinity nature of samples. These results match the PXRD data, indicating the nano-crystalline character of the selected area. EDS of AB9-MNPs demonstrates the presence of iron, carbon, oxygen, nitrogen, and sulfur atoms, consistent with the presence of AB9 on the $Fe_3O_4$ surface.

The powder XRD patterns for MNP and AB9-MNP are shown in Figure 4-4. However, Silica showed amorphous nature for the AB9-silica sample, therefore not provided here. The XRD pattern obtained shows that all diffraction peaks at $2\theta = 18$(*hkl*s), 30 (220), 36 (311), 43 (400), 54 (422), 56 (511), and 63 (440), 72 (620) and 74 (533), which matches with the crystal planes of cubic inverse spinel phase of $Fe_3O_4$ and agree with JCPDS card no. 79-0417. [154]
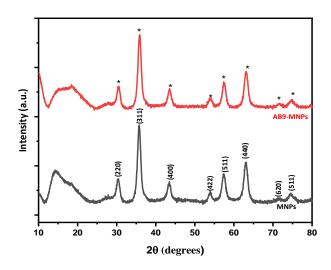


Figure 4-4. Powder XRD spectrum of prepared MNPs.

Moreover, no other significant peaks were observed, which indicates the synthesized MNPs do not contain any other crystallite impurities. The peaks in XRD show

some broad change in intensity, indicating nanosized particles.[152] Moreover, the main

peaks in as-synthesized AB9-MNPs are consistent with those MNPs. This reveals that the

introduction of thiol groups has no effect on the as-synthesized MNP particles and AB9

successfully has been incorporated on the surface of MNPs. For this product in the

synthetic scheme, the XRD indexed to the cubic inverse spinel $Fe_3O_4$ with slight

broadening $2^\theta = 20$ from amorphous silica. In addition, The AB9 anchoring does not induce

any phase changes in the MNP surface. The results can also be proved via SEM images.

The corresponding FT-IR spectra of the silica, AB9-silica, MNPs, and AB9-MNPs

in the region of 500–4000 cm$^{-1}$ are presented in Figure 4-5, employed to study the

performance and change of functional groups on the surface of materials.
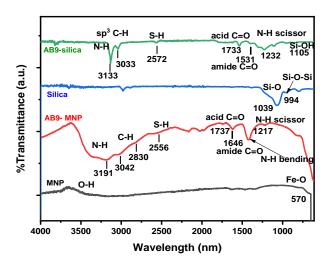


Figure 4-5. FTIR spectra of raw silica, AB9-silica, raw MNP, and AB9-MNPs.

The FT-IR spectrum of MNPs shows a characteristic band around 3500 cm$^{-1}$ which

is attributed to the stretching mode for OH originating from OH groups on the MNPs

surface. The band at 570 cm$^{-1}$ is attributed to the Fe-O bond of bulk magnetite. The FT-IR

spectrum of AB9-MNP (clearly showing) exhibited broad bands at 3500- 3000 cm$^{-1}$ attributable to O–H stretching and O–H bending vibration from physisorbed water molecules with $H_2O$ deformation band (bending H-O-H groups) at 1635 cm$^{-1}$ and around 3430 cm$^{-1}$ is attributed to the N-H stretching in amino groups of AB9 molecule.[155] The presence of N-H is also evidenced by the presence of a peak for N-H bending ~1515 cm$^{-1}$. The bands at 570 are related to the Fe–O stretching frequency attached to the iron. The raw silica shows 1039 cm$^{-1}$ due to Si-O, and 906 cm$^{-1}$ due to Si-OH stretching. Similar values can be seen in AB9-MNP and AB9-silica. The bands in both AB9-silica and AB9-MNPs around 3133- 3000 cm$^{-1}$ are attributed to the C–H stretching vibration of hydrocarbon chains. The FT-IR diagram of both AB9 functionalized silica and AB9 show a weak absorption peak at 2572 cm$^{-1}$ and 2556 cm$^{-1}$ respectively which is due to the introduction of SH.[93] The C=O shows weak signals at 1400- 1600 cm$^{-1}$ which are also convoluted by contamination of the $CO_2$ stretching bands from the background.[89] Thus, IR shows the subsequent preparations retained S-H, though it is an unusual shift from (opposed to 2550 cm$^{-1}$ for normal thiols), presumably due to thiol aggregation and perhaps hydrogen bonding effects. However, this proves that thiol preparation worked well on the MNP and silica surfaces.

These materials have a high surface area, which allows their use in multiple applications. This inherent property can be tuned by varying sizes, shapes, and morphology. The effectiveness of such materials depends on the micro and mesostructured, which allow active molecules to disperse on the large internal surface, thereby improving the activity, as poor accessibility will limit their applications when significant mass transport is vital.[156, 157]

The porosity of the synthesized MNPs was characterized by $N_2$ adsorption analysis at 77 K (Figure 4-6).
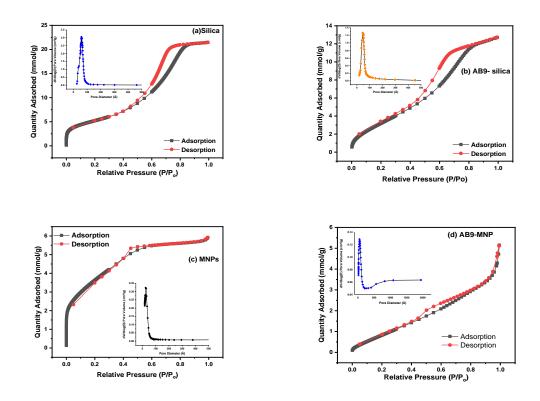


Figure 4-6. $N_2$ adsorption desorption for (a) raw silica, (b) AB9-silica, (c) MNP, and (c) AB9-MNPs (pore size distribution inset).

The nitrogen adsorption isotherm of the samples is a type IV isotherm. The isotherm does level off in the vicinity of the relative pressure ($P/P_o$) of 1, pointing to the existence of mesopores. The appearance of a type $H_3$ hysteresis loop in the $P/P_o$ range of 0.5- 1.0 is usually associated with capillary condensation in mesopore structures.

Physical properties such as surface area, pore-volume, and average pore radius of as and the Brunauer−Emmett−Teller (BET) analysis of the silica, and prepared AB9-silica, MNPs, and AB9-MNPs are tabulated in Table 4-1. These data revealed a relatively higher

surface area for AB9-silica (307.18 $m^2\ g^{-1}$) than AB9- MNPs (96.97 $m^2\ g^{-1}$) and the total

pore volume calculated using the single-point adsorption value at $P/P_o = 0.9972$ were 0.44

and 0.17 $cm^3g^{-1}$ respectively.

The pore size distribution calculated using the Barrett–Joyner–Halenda (BJH)

method shows a uniform mesoporosity of the materials with a pore size of 7.02, 5.74, 2.74,

and 7.29 nm respectively (Figure 4-6 insets). In addition, the condensation at high values

of $P/P_0$ may suggest the presence of macro-pores. The presence of mesopore and

macropores in these materials can be useful for the adsorptive removal of heavy metal

Pb(II).

Table 4-1. Structure parameters of Raw MNP, Citrate-MNP, Silica-MNP, APTS-MNP, Covalent MNP, and Ionic-MNP.

| Material type | Pore size (nm)[a] | Pore volume ($cm^3g^{-1}$)[b] | BET surface Area ($m^2g^{-1}$) |
|---|---|---|---|
| Silica | 7.02 | 0.74 | 434.32 |
| AB9-silica | 5.74 | 0.44 | 307.18 |
| MNP | 2.74 | 0.20 | 299.29 |
| AB9- MNP | 7.29 | 0.17 | 96.97 |

A.Pore size was calculated by BET. b Pore volume determined by BJH.

There is not much decrease in surface area and pore size of silica and MNPs to

AB9-silica and AB9-MNPs. This is probably due to disruption in the aggregation after

surface modification. In addition, this decrease in the surface area is possible due to the

presence of a layer of AB9 on the silica and MNP surface.

Specific surface area determinations measure the external surface area and open

pores of macroporous and mesoporous materials. The mesoporous is in pore sizes 2 to 50

nm, whereas microporous is in pore sizes up to 2 nm. Mesoporous pores also provide effective transport pathways to the interior cavities. Moreover, all material shows the type IV isotherms, proving the presence of mesopores according to the BET classification unlike previously reported nonporous structures of magnetite and silica.

**Adsorption study.**

The distribution coefficient ($K_d$) is a measure of the chemical binding affinity of a sorbent. Generally, higher $K_d$ values $10^3$ mg/L are considered good, above $10^4$ mg/L outstanding.[158] Some other facts affecting the ability are; the pH of the solution, metal ion capacity to undergo hydrolysis, stability constant of ligand-metal complex, and p$K_a$ of the ligand.[159]
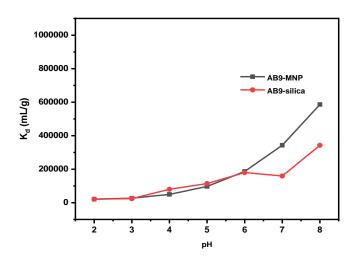


Figure 4-7. Effect of pH on the $K_d$ values.

According to Figure 4-7, affinities are higher in AB9-silica and AB9-MNP and increase when pH increases. This might be due to p$K_a$ of AB9 (p$K_{a, COOH}$ of 2.71 and 3.43

106

and $pK_{a, SH}$ of 9.65)[160] the functional groups remain protonated. Thus, reducing affinities for metal Pb(II) at lower pH. However, larger $K_d$ values are even possible at lower pH. Moreover, retention of higher $K_d$ even in highly acidic conditions implies that both AB9-functionalized silica and MNP are suitable for direct usage for toxic heavy metals.
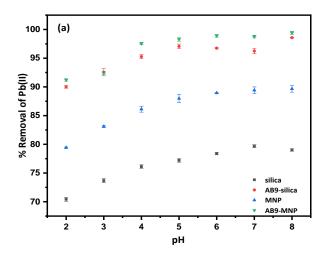
**Effect of pH on metal ion adsorption.**

The pH of the solution acts as the fundamental controlling parameter of the rate of sorption of the chemistry of the metal in the solution and active sites. Different initial pH values (2-8) were prepared using 0.1 M NaOH and 0.1 M HCl and treated with 5 mg of samples at $25 \pm 0.5$ °C for 6 h. As can be seen in figure 4.8a, the increase in the pH leads to an increase in the removal efficiency until pH ~5, beyond which remains almost constant. One reason may be at lower pH, H⁺ is higher in the medium making higher competition between H⁺ and Pb(II) thus providing fewer active sites for Pb(II) ions.[161] Another reason may be the amphoteric nature of the surface of MNP.[153]

At lower pH, protonation of thiol group binding sites are generally protonated or positively charged by the $H_3O^+$ ions in the medium, thus repulsion occurs between positively charged Pb(II) ions and the adsorbent. While at higher pH values, thiol binding sites start deprotonating making them more accessible for Pb(II) binding.

The figure reveals that the removing efficiency of Pb(II) ions is pH-dependent and the utmost efficiency occurred at pH = 8 for AB9-silica (98.58%), MNP (89.66%), AB9-MNPs (99.42%), and pH = 7 for silica (79.68%). This implies that higher pH values are favorable for the deprotonation of sorbent surface, and this increment raises the sites with negatively charged, enhancing attractive forces between Pb(II) and the surface of sorbents.

Whereas, in lower pHs repulsion between them occurs. However, in any of these cases, metal hydroxide was not observed, which may reduce the final discoverable Pb(II) in the solution.
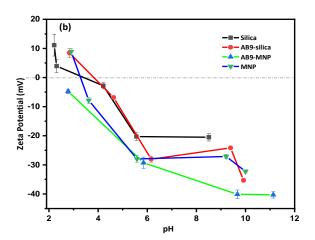


Figure 4-8. (a) Effect of pH on the removal of Pb(II) ions by silica, AB9-silica, MNP, and AB9-MNPs at 25 C. (b) Effect of solution pH on the zeta potential of each adsorbent.

To understand further charged species and the impact of pH, the zeta potential (Figure 4-8b) was analyzed on as-prepared silica and MNPs using a zeta potential analyzer at room temperature. The measurement of ZPC was conducted by adjusting the pH of a 50 mL sample with 0.01 M HCl or 0.01 M NaOH solution to a value between 2 and 12. The adsorbent materials surface of either silica or MNPs represent zeta potential decrease with gradual increase of pH and continue to increase to the negative side as the pH further increases. After grafting with AB9 thiol, the surface of MNPs (AB9-MNPs) is completely negatively charged. The potential of zero charges (ZPC where the total charge is considered zero) of the MNPs is 3.98, consistent with the literature.[151] Whereas, AB9-silica has a ZPC at pH= 4. The potentials of AB9 MNP seem to be higher than the initial steps' potentials, as the thiol is a soft base.[93] Thus, these electrochemical properties of the surface prove that the adsorption properties depend on the surface potential and the AB9-MNP has the highest adsorption of all the materials. When the pH was higher than the ZPC, the net surface charge was negative, which was beneficial for cation Pb(II) adsorption promoting metal ions' electrostatic attractions. In most of these materials when the pH range is below 3, the net surface charge would be positive, which was not favorable for metal ion adsorption promoting electrostatic repulsion between Pb(II) and adsorbent. This is well illustrated by obtained metal removal graphs (Figure 4-8a) illustrating weaker removal in lower pH values. Nevertheless, after pH = 8, Pb(II) might precipitate as Pb(OH)$_2$ at 25 °C ($k_{sp}$ = 1.43 × 10$^{-20}$). However, no hydroxide formation was witnessed during the removal process. The precipitation might add some uncertainty but luckily it was not the case here. However, a neutral pH was used for removal experiments.

.

**Effect of adsorbent dosage on removal percentage of Pb(II).**

Generally, when the adsorbent dose increases, the sorption of metal increases because more active sites on the adsorbent become available.[162]
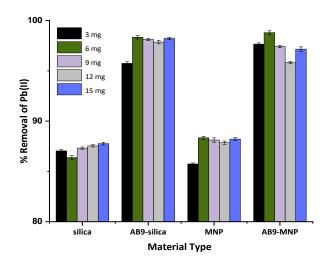


Figure 4-9. Effect of adsorbent dose (mg) on removal percentage of Pb(II) by adsorbent (initial metal concentration = 50 mg/L, adsorbent weight, 3, 6, 9, 12,1, and 15 mg and pH=5 under ambient room temperature for 6 hours).

The influence of dosages on adsorption is shown in Figure 4-9 which implies that generally increasing the quantity of sorbent (mg), caused the percent of Pb(II) a higher removal. The highest removal of Pb(II) was observed for AB9-MNP at 6 mg. At this amount of sorbent nanoparticles, about 99% were removed. For silica, AB9-silica, and MNP the removal was 86.38, 98.34, and 88.34 % respectively. Thus, it was considered that 5-6 mg is the optimum dosage. This behavior can be explained by the increasing number of binding sites with the increased amount of absorbent. Thus, leading to a higher sorption capacity ascribed by nano-scale particle size giving access to the larger surface area.

**Adsorption isotherm analysis.**

These isotherms describe how metals interact with adsorbents, having clarification of the adsorption mechanism and equilibrium adsorption capacity. The Langmuir, Freundlich, Temkin, and Dubinin - Radushkevish (D-R) models were selected to fit equilibrium data from batch adsorption studies.

The room temperature adsorption capacities of Pb(II) were calculated to evaluate liquid/solid interphase at equilibrium during adsorption. The Langmuir adsorption was applied assuming monolayer adsorption onto the surface with a finite number of identical sites.[163] The Langmuir adsorption expressed (equation 4) as:

$$\frac{C_e}{q_e} = \frac{C_e}{q_m} + \frac{1}{q_m\,b} \qquad (4)$$

The dimensionless constant called the equilibrium parameter (equation 5), is called the essential characteristic of the Langmuir isotherm, which is defined by the following equation. The value of $R_L$ indicates whether the adsorption is unfavorable for $R_L > 1$, linear for $R_L = 1$, and favorable for $0 < R_L < 1$ or reversible $R_L = 0$.

$$R_L = \frac{1}{1+K_L C_O} \qquad (5)$$

Langmuir isotherm suggests that adsorption occurs at specific homogeneous sites within the adsorbent. while the Freundlich isotherm describes non-ideal heterogenous multilayer adsorption assuming the increasing concentration of the adsorbate on the adsorbent surface as the adsorbate concentration increases. (equation 6).

$$\text{Freundlich equation; } Ln\ q_e = lnK_f + \frac{1}{n}\ lnC_e \qquad (6)$$

Where; $q_e = \dfrac{C_i - C_e}{m} V$

Where $q_e$ is the amount of adsorbed metal ions at equilibrium (mg/g), $C_i$ and $C_e$ are the initial and equilibrium concentrations of metal ions in solution (mg/L). m is the mass of adsorbent (mg), and V is the volume of the metal solution (L). In the Langmuir equation, $q_m$ (mg/g) is the measure of monolayer adsorption (maximum) capacity, and $b$ is the equilibrium constant related to the adsorption energy. These values can be obtained by plotting a graph $C_e/q_e$ against $C_e$. Whereas, Freundlich isotherm gives the parameter n, which is an indication of adsorption intensity and bond energies between the metal ion and the adsorbent. $K$ is the Freundlich constant with multilayer adsorption related to bond strength-giving by the plot $Ln \, q_e$ against $Ln \, C_e$

The Temkin,

$$q_e = \frac{RT}{b_t} \ln \alpha_t + \frac{RT}{b_t} \ln C_e \qquad (7)$$
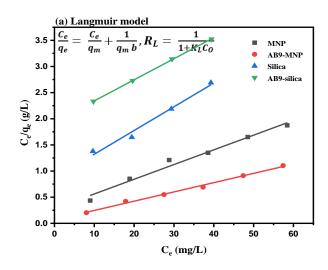
and D-R isotherm equations are;

$$ln q_e = ln q_{max} - B\varepsilon^2 \qquad (8)$$

$$\varepsilon = RT \ln\left(1 + \frac{1}{C_e}\right)$$

Where $q_{max}$ (mg/g) is the monolayer saturation adsorption capacity; $C_e$ (mg/g) is the concentration of metal ions at equilibrium; $K_L$ (L/mg) is the Langmuir constant related to the adsorption capacity; the value $R_L$ indicates the nature of isotherm as unfavorable ($R_L > 1$), linear (($R_L = 1$), favorable ($0 < R_L < 1$), irreversible ($R_L = 0$); $K_f$ is the

Freundlich constant, $1/n$ is the value used to indicate the heterogeneity of the interface; qe (mg/g) is the adsorption capacity at equilibrium; R is the ideal gas constant [8.314 J/(mol K)]; T (K) is the absolute temperature of the adsorption process; $\alpha_t$ (L/g) and bt (J/mol) are Temkin isotherm constants; B is the D–R constant, and $\varepsilon$ is the Polanyi potential, which can be calculated from Eq.
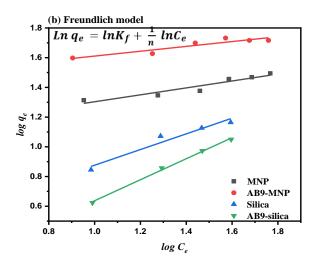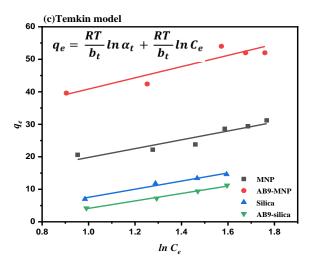


Figure 4-10. The fit of data for Pb(II) sorption on silica, AB9-silica, MNP, and AB9-MNP to (a) Langmuir isotherm, and (b) the Freundlich isotherm.

The experimental data were fitted using these four models and the results are shown in the figure. Obtained parameters with respective correlation coefficients ($R^2$) for Langmuir and Freundlich models are shown in Table 4.2. From the $R^2$ values for the Langmuir isotherm model, it is determined that the Langmuir isotherm fits well within the experimental data for Pb(II) ions in both AB9-silica and AB9-MNP.

**(c)Temkin model**

$$q_e = \frac{RT}{b_t} \ln \alpha_t + \frac{RT}{b_t} \ln C_e$$

MNP
AB9-MNP
Silica
AB9-silica

**(d) D-R model**

$$\ln q_e = \ln q_{max} - B\varepsilon^2, \; \varepsilon = RT \ln\left(1 + \frac{1}{C_e}\right)$$

MNP
AB9-MNP
Silica
AB9-silica
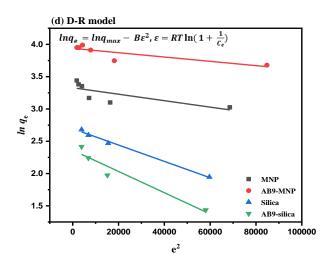
Figure 4-11. The fit of data for Pb(II) sorption on silica, AB9-silica, MNP, and AB9-MNP to (a) Temkin isotherm and (b) the D-R model.

114

Table 4-2. The parameters and correlation coefficients of the adsorption isotherm models for the adsorption of Pb(II) ions from aqueous solution using silica, AB9-silica, MNP, and AB9-MNP adsorbents.

| | Langmuir | | | Freundlich | | | Temkin | | | Dubinin−Radushkevich | | |
|---|---|---|---|---|---|---|---|---|---|---|---|---|
| | $q_{max}$ (mg/g) | $K_L$ (L/mg) | $R^2$ | $K_f$ (mg/g) | $1/n$ | $R^2$ | $\alpha t$ | $b_t$ (J/mol) | $R^2$ | B (mol$^2$/J$^2$) | $q_{max}$ | $R^2$ |
| Silica | 22.05 | 0.05 | 0.9738 | 1.41 | 0.53 | 0.9245 | 0.67 | 198.35 | 0.9691 | $1.65 \times 10^{-5}$ | 14.80 | 0.9890 |
| AB9-silica | 24.80 | 0.02 | 0.9996 | 0.93 | 0.71 | 0.9954 | 0.53 | 216.35 | 0.9897 | $1.27 \times 10^{-5}$ | 10.61 | 0.9075 |
| MNP | 35.57 | 0.10 | 0.9744 | 2.92 | 0.23 | 0.8840 | 1.58 | 182.70 | 0.8576 | $5.00 \times 10^{-6}$ | 27.9 | 0.4846 |
| AB9-MNP | 56.40 | 0.26 | 0.9924 | 4.25 | 0.16 | 0.8311 | 3.92 | 143.57 | 0.8173 | $3.34 \times 10^{-6}$ | 51.32 | 0.6500 |

This shows the monolayer adsorption capacity ($q_{max}$) found to be 24.80 mg/g for AB9-silica and a very high value of 56.40 mg/g for AB9-MNP. These values are normally higher than known functionalized 3-mercaptopropyl-groups functionalized silica[82], and thiol (49.1 mg) MNP.

The value of equilibrium parameter $K_L$ for the Langmuir isotherm was found to be 0.05, 0.02, 0.1, and 0.26 respectively for silica, AB9-silica, MNP, and AB9-MNP. which was consistent with the requirement for a favorable adsorption process under the conditions used during this study, while the adsorption parameters obtained within the Freundlich adsorption model showed the unfavourability of adsorption and represented difficult adsorption characteristics.

**Magnetic Separation and Recycling Study**.

The recycling efficiency was investigated for AB9-MNP, as AB9-MNP was showing the highest removal of Pb(II) in the study. Considering the pH study, the percentage of adsorbed Pb(II) was smaller at low pH because of desorption from the

organic functional groups. Therefore, an acidic medium was used for the regeneration of Pb(II)-loaded AB9-MNP.
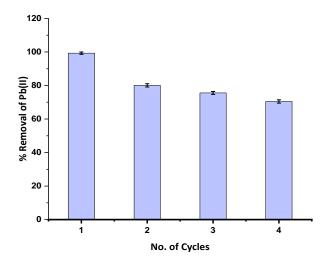


Figure 4-12. Recycling efficiency of AB9-MNP for Pb(II) adsorption during cyclic experiments.

The recycling efficiency (Figure 4-12) of the MNP was studied by cycling between adsorption under optimum adsorption conditions (pH 6 and initial Pb(II) concentration: 50 mg/L) and desorption under acidic conditions (washing AB9-MNP using HCl at pH 2). After each adsorption and desorption cycle, the MNP was thoroughly washed with DI water. As shown in the figure although a slight decrease in the removal efficiency of Pb(II) was observed after successive cycles, from 99.98% to 80.09%, 75.57%, and then 70.47%, the removal efficiency was higher than 70% even after four cycles. The slight decrease in removal efficiency may be due to the loss of the organic capping ligand during Pb(II) desorption using an acidic solution. Therefore, it can be reasoned that the Pb(II) removal efficiency of AB9-MNP can be enhanced by the incorporation of the AB9, and as-

synthesized AB9-MNP can be easily recycled through several applications without any significant loss in efficiency.

## 4.5    Conclusion.

AB9 -MNP, and AB9-silica show a high affinity towards Pb(II)    due to the selective nature of "soft" sulfhydryl groups. There is a higher removal by AB9-MNP, than AB9-silica, with an added advantage of magnetical separation. However, the adsorption reactivity depends on particle size, agglomeration, etc. The exploiting of covalent Pb(II)-S bonds and with recycling ability shows that the MNP are recyclable without losing their Pb(II) removal ability.

CHAPTER 5. CONCLUSION AND FUTURE DIRECTIONS

Even though centuries of research have passed, finding solutions to minimize the threat to humans from exposure to heavy metals via a low-cost and easy-to-handle method remains a challenge. This research study sought to address above mentioned issues while establishing a series of dithiol molecules. PB9 was applied as a precipitation agent for Pb(II), and as a selective and sensitive sensor for Fe(III) ions. This study of the structural chemistry and reactivity of lead and Iron-thiolate is important because of their toxicity.

PB9, a ligand capable of binding divalent Pb(II) efficiently, was synthesized and characterized. The resulting PB9/Pb(II) of 1:1 and 2:1 metal compounds displayed stability, non-reversible nature, and broad melting points, and their thermal analysis showed that they are thermally stable and do not contain coordinated water in their molecules. The insolubility in common solvents implies their polymeric or oligomeric nature due to bridging S-M····S groups. However, metal-ligand compounds are stable and show negligible leaching over time.

Herein, this dissertation also discusses the study of PB9 as a low-cost, portable, simple-to-use, accurate optical chemical sensor for the detection of Fe(III) in DMSO. PB9 acts as a fluorescent "turn-off" probe for Fe(III). This displayed fluorescence quenching is more likely due to the binding of the paramagnetic Fe(III) metal ion. The fluorescence emission of the PB9 may be diminished by the paramagnetic nature of the Fe(III) resulting in chelation enhanced quenching (CHEQ). Intersystem crossing (ISC) becomes faster due to the presence of a paramagnetic metal atom in the proximity of the fluorophore which results in fluorescence quenching. However, in natural water, the matrix effect should be

considered. There are many competitive complexed ions of water constituents (such as inorganic and organic ligands) that may have with metal ions, thus making competition for binding to the ligand.

The applicability of attaching AB9, containing carboxylic acid group, on a solid support such as silica and MNP through the formation of amide linkages was explored. The AB9 functionalized $Fe_3O_4$ nanoparticles and silica were inexpensive and efficient. The AB9-MNP were found to have a higher removal efficiency as high as 99.9% for Pb(II) with a maximum adsorption capacity of 49.1 mg/g, which compared to commonly used sorbent materials, the magnetic property of the suspended MNP allows their easy separation from large-volume samples using an external magnetic field instead of centrifugation or filtration, which simplifies and accelerates the isolation process. Furthermore, the prepared material not only shows a better Pb (II) adsorption capacity than other reported materials but also proves easy recyclability without significant loss of Pb(II) removal efficiency. Therefore, it is expected that these findings may supply new insight into the design and tailoring of high-performance Pb(II) adsorbents by eco-friendly methods. It should be mentioned here that AB9 is moisture sensitive, but with solid support lasts for a longer time, with an effective Pb(II) removal.

These reactivities of PB9 and AB9 are based on the reactivity of sulfhydryl groups, with appended cysteamine or cysteine respectively. Both these bidentate sulfhydryl ligands show high affinities for Pb(II); for removal and Fe(III); for sensing action. I hope that the above-discussed scenarios in this dissertation will encourage more laboratories to exploit coordination chemistry as a sensitive means of biasing the Pb(II) removal and sensing. The design of powerful luminescent sensors with less toxicity will then be

accelerated. These will be useful solutions in monitoring problems in a variety of contexts. The latter should create interesting possibilities for molecular information handling.

Application of dissolved or metallated PB9 in batch remediation scenarios will be useful in municipal water treatment systems, and a toxicity study shall help utilize this molecule in environmental systems. However, portable, lightweight column, film, or set up for use in homes or any affected areas by Pb(II) require alternative methods for ligand applications. Alternatively, the ligand could apply as a sodium or potassium salt making sure no disulfide product formation. Moreover, hydrophobicity shall be considered here, otherwise, aqueous solutions may not pass through the ligand. Thus, further research shall proceed with finding a way to attach the PB9 to make it immobilize into solid support.

Molecules that supply optical and electrochemical signals are ideal for the development of dual signal transductions in addition to color change. For this purpose, a Differential Pulse Voltammetry (DPV) can be employed to measure the change in electrochemical signals of PB9 with Fe(III) upon addition of Fe(III) the shifts in the potentials, current flow would also act as a confirmation of Fe(III) binding to the PB9. Thus, this cost-effective miniaturized PB9 devise supplies a rapid, automated, advancement in optical sensor technology. Given the difficulty of designing fluorescent sensors for paramagnetic Fe(III) ions, the PB9 compounds may inspire the further development of more sophisticated sensing constructs for the detection of transition metal ions. This is not only because of their inherent excellent properties including operational simplicity, low cost, and real-time monitoring but also their advantages of significant application in biological and environmental.

PB9 provided the opportunity to study the advantage of the aqueous chemistry of $d^{10}$ metal ion, Pb(II). The study of this S/N ligand PB9 and AB9 could make it suitable for studying these kinds of metals leading to future applications of studying metallothionein. It is known that part of the toxicity of Pb(II) is due to its competition with Zn(II) in liver alcohol dehydrate and zinc-finger proteins.[164] The Pb(II) compounds reported here with having either $N_3S_2$ or $N_2S_2$ around the metal center might be useful as a biological model for Zn(II) containing metalloenzymes, as the ratio of Pb(II) and Zn(II) bound to a site is determined by the relative affinities.[129] The pathways described here for the formation of metal-thiol compounds might be useful in understanding the behavior of metal thiolates in solutions, eventually helping understand the metal chemistry in biological systems.

Future research shall be done using environmental waste for eco-friendly removal. Additionally, future studies should be directed at preparing a water-soluble analog of these thiol molecules. Challenging work should be performed to change reaction conditions to gain single-crystal structures. Otherwise, XAFS should establish the coordination environment of metal in ligands.

REFERENCES

1. Tchounwou, P. B.; Yedjou, C. G.; Patlolla, A. K.; Sutton, D. J., Heavy Metal Toxicity and the Environment. In *Molecular, Clinical and Environmental Toxicology: Volume 3: Environmental Toxicology*, Luch, A., Ed. Springer Basel: Basel, **2012**; pp 133-164.

2. Tchounwou, P. B.; Yedjou, C. G.; Patlolla, A. K.; Sutton, D. J., Heavy Metal Toxicity and the Environment. In *Experientia Supplementum*, Springer Basel: **2012**; pp 133-164.

3. Abadin, H.; Ashizawa, A.; Stevens, Y.-W.; Llados, F.; Diamond, G.; Sage, G.; Citra, M.; Quinones , A.; Bosch, S. J.; Swarts , S. G. *Toxicological Profile for Lead*; Agency for Toxic Substances and Disease Registry (ATSDR) Toxicological Profiles: Atlanta (GA): Agency for Toxic Substances and Disease Registry (US), **2007**.

4. Bjørklund, G.; Crisponi, G.; Nurchi, V. M.; Cappai, R.; Buha Djordjevic, A.; Aaseth, J., A Review on Coordination Properties of Thiol-Containing Chelating Agents Towards Mercury, Cadmium, and Lead. *Molecules* **2019,** *24* (18), 3247.

5. Oudijk, G., The Rise and Fall of Organometallic Additives in Automotive Gasoline. *Environmental Forensics* **2010,** *11* (1-2), 17-49.

6. Patrick, L., Lead toxicity, a review of the literature. Part 1: Exposure, evaluation, and treatment. **2006, March,** *11(1)*, 2-22.

7. Triantafyllidou, S.; Edwards, M., Lead (Pb) in Tap Water and in Blood: Implications for Lead Exposure in the United States. *Critical Reviews in Environmental Science and Technology* **2012,** *42:13*, 1297-1352.

8. Jacobs, D. E.; Clickner, R. P.; Zhou, J. Y.; Viet, S. M.; Marker, D. A.; Rogers, J. W.; Zeldin, D. C.; Broene, P.; Friedman, W., The prevalence of lead-based paint hazards in U.S. housing. *Environmental Health Perspectives* **2002,** *110* (10), a599-a606.

9. Ure, A. M.; Davidson , C. M., *Chemical Speciation in the Environment*. 1 ed.; Chapman and Hall, London, **1995**.

10. Fan, J.; Cai, C.; Chi, H.; Reid, B. J.; Coulon, F.; Zhang, Y.; Hou, Y., Remediation of cadmium and lead polluted soil using thiol-modified biochar. *Journal of Hazardous Materials* **2020,** *388*, 122037.

11. Erten-Unal, M.; Wixson, B. G.; Gale, N.; Pitt, J. L., Evaluation of toxicity, bioavailability and speciation of lead, zinc and cadmium in mine/mill wastewaters. *Chemical Speciation & Bioavailability* **1998,** *10* (2), 37-46.

12. Matlock, M. M.; Howerton, B. S.; Atwood, D. A., Irreversible precipitation of mercury and lead. *Journal of Hazardous Materials*, **2001**; Vol. 84, pp 73-82.

13. Matlock, M. M.; Howerton, B. S.; Atwood, D. A., Chemical Precipitation of Lead from Lead Battery Recycling Plant Wastewater. *Industrial & Engineering Chemistry Research* **2002,** *41* (6), 1579-1582.

14. Drake, R. F., Introduction to Environmental Chemistry (Bunce, Nigel). *Journal of Chemical Education* **1996,** *73* (11), A278.

15. Lovering, T. G., Lead in the environment. Washington : U.S. Dept. of the Interior, Geological Survey : for sale by the Supt. of Docs., *U.S. Govt. Print. Off.*, **1976**.

16. Smith, J. D., Inorganic chemistry of main group elements. *Journal of Organometallic Chemistry* **1996,** *508* (1-2), 281.

17.      Cotton, A. F.;  Wilkinson, G.;  Murillo, C. A.; Bochmann, M., Advanced Inorganic Chemistry. 6 ed.; *John Wiley & Sons, Inc*: **1999**.

18.      Giraldo, L.; Moreno-Piraján, J., Pb2+ adsorption from aqueous solutions on activated carbons obtained from lignocellulosic residues. *Brazilian Journal of Chemical Engineering* **2008,** *25* (1), 143-151.

19.      Shahid, M.;  Khalid, S.;  Abbas, G.;  Shahid, N.;  Nadeem, M.;  Sabir, M.;  Aslam, M.; Dumat, C., *Heavy metal stress and crop productivity*. **2015**; pp 1-25.

20.      Pearce, J. M., Burton's line in lead poisoning. *Eur Neurol* **2007,** *57* (2), 118-9.

21.      Fleischer, H.; Schollmeyer, D., Synthesis of and Structural Studies on Lead(II) Cysteamin Complexes. *Inorganic Chemistry* **2004,** *43* (18), 5529-5536.

22.      Bharara, M. S.;  Kim, C. H.;  Parkin, S.; Atwood, D. A., Synthesis and X-ray crystal structures of dinuclear hydrogen-bonded cadmium and lead 2-aminoethanethiolates. **2005**; Vol. 24, pp 865- 871.

23.      Guerrero, M.;  Pons, J.;  Ros, J.;  Font-Bardia, M.; Branchadell, V., Anion Influence on the Structure of N,O-Hybrid Pyrazole ZnII, CdII, and HgII Complexes. Synthesis, Characterization, and Theoretical Studies. *Crystal Growth & Design* **2012,** *12* (7), 3700-3708.

24.      Pearson, R. G., Hard and Soft Acids and Bases. *J. Am. Chem. Soc.* **1963,** *85* (22), 3533-3539.

25.      Matlock, M., Aqueous leaching properties and environmental implications of cadmium, lead and zinc Trimercaptotriazine (TMT) compounds. *Water Research* **2001,** *35* (15), 3649-3655.

26.      Matlock, M. M.;  Howerton, B. S.;  Van Aelstyn, M. A.;  Nordstrom, F. L.; Atwood, D. A., Advanced Mercury Removal from Gold Leachate Solutions Prior to Gold and Silver Extraction:  A Field Study from an Active Gold Mine in Peru. *Environmental Science & Technology* **2002,** *36* (7), 1636-1639.

27.      Matlock, M. M.;  Howerton, B. S.;  Robertson, J. D.; Atwood, D. A., Gold Ore Column Studies with a New Mercury Precipitant. *Industrial & Engineering Chemistry Research* **2002,** *41* (21), 5278-5282.

28.      Matlock, M. M.;  Howerton, B. S.; Atwood, D. A., Chemical precipitation of heavy metals from acid mine drainage. *Water Research* **2002,** *36* (19), 4757-4764.

29.      Matlock, M. M.;  Howerton, B. S.;  Aelstyn, M. V.;  Henke, K. R.; Atwood, D. A., Soft metal preferences of 1,3-benzenediamidoethanethiol. *pubmed* **2003,** *37* (3), 579-584.

30.      Burriss, D.;  Zou, W.;  Cremer, D.;  Walrod, J.; Atwood, D., Removal of Selenite from Water Using a Synthetic Dithiolate: An Experimental and Quantum Chemical Investigation. *Inorganic Chemistry* **2014,** *53* (8), 4010-4021.

31.      Alexie, M.;  Dumitru, F.;  Razvan, A.;  Pasare, L.; Guran, C., New Membranes with Mercapto –2,6–pyridinediamides as Anion Recognition Fixed Sites. *Revista de Chimie -Bucharest- Original Edition-* **2010,** *12*, 1197-1201.

32.      M  Matlock , M.;  S  Howerton , B.;  R  Henke , K.; A  Atwood , D., A pyridine-thiol ligand with multiple bonding sites for heavy metal precipitation. *Journal of Hazardous Materials* **2001,** *82* (Issue 1), 55-63.

33.      Weng, Y.-Q.;  Yue, F.;  Zhong, Y.-R.; Ye, B.-H., A Copper(II) Ion-Selective On−Off-Type Fluoroionophore Based on Zinc Porphyrin−Dipyridylamino. *Inorganic Chemistry* **2007,** *46* (19), 7749-7755.

34. Zhou, Y.; Yoon, J., Recent progress in fluorescent and colorimetric chemosensors for detection ofamino acids. *Chem. Soc. Rev.* **2012,** *41* (1), 52-67.

35. Bao, X.; Shi, J.; Nie, X.; Zhou, B.; Wang, X.; Zhang, L.; Liao, H.; Pang, T., A new Rhodamine B-based 'on–off' chemical sensor with high selectivity and sensitivity toward Fe3+ and its imaging in living cells. *Bioorganic & Medicinal Chemistry* **2014,** *22* (17), 4826-4835.

36. Carlson, E. S.; Magid, R.; Petryk, A.; Georgieff, M. K., Iron deficiency alters expression of genes implicated in Alzheimer disease pathogenesis. *Brain Research* **2008,** *1237*, 75-83.

37. Chen, X.; Hong, H.; Han, R.; Zhang, D.; Ye, Y.; Zhao, Y.-F., A New bis(rhodamine)-Based Fluorescent Chemosensor for Fe3+. *Journal of Fluorescence* **2012,** *22* (3), 789-794.

38. Chen, W.-D.; Gong, W.-T.; Ye, Z.-Q.; Lin, Y.; Ning, G.-L., FRET-based ratiometric fluorescent probes for selective Fe3+ sensing and their applications in mitochondria. *Dalton Transactions* **2013,** *42* (28), 10093.

39. Murphy, C. B.; Zhang, Y.; Troxler, T.; Ferry, V.; Martin, J. J.; Jones, W. E., Probing Förster and Dexter Energy-Transfer Mechanisms in Fluorescent Conjugated Polymer Chemosensors. *The Journal of Physical Chemistry B* **2004,** *108* (5), 1537-1543.

40. Oehme, I.; Wolfbeis, O. S., Optical sensors for determination of heavy metal ions. *Mikrochimica Acta* **1997,** *126* (3-4), 177-192.

41. De Acha, N.; Elosúa, C.; Corres, J.; Arregui, F., Fluorescent Sensors for the Detection of Heavy Metal Ions in Aqueous Media. *Sensors* **2019,** *19* (3), 599.

42. Wu, G.; Li, M.; Zhu, J.; Lai, K. W. C.; Tong, Q.; Lu, F., A highly sensitive and selective turn-on fluorescent probe for Pb(ii) ions based on a coumarin–quinoline platform. *RSC Advances* **2016,** *6* (103), 100696-100699.

43. Wolfbeis, O. S., Fiber-Optic Chemical Sensors and Biosensors. *Analytical Chemistry* **2006,** *78* (12), 3859-3874.

44. Fraiji, L. K.; Hayes, D. M.; Werner, T. C., Static and dynamic fluorescence quenching experiments for the physical chemistry laboratory. *Journal of Chemical Education* **1992,** *69* (5), 424.

45. Fu, L.; Mei, J.; Zhang, J.-T.; Liu, Y.; Jiang, F.-L., Selective and sensitive fluorescent turn-off chemosensors for Fe3+. *Luminescence* **2013,** *28* (4), 602-606.

46. Das, S.; Aich, K.; Goswami, S.; Quah, C. K.; Fun, H.-K., FRET-based fluorescence ratiometric and colorimetric sensor to discriminate Fe3+ from Fe2+. *New Journal of Chemistry* **2016,** *40* (7), 6414-6420.

47. Maity, P.; Naskar, B.; Goswami, S.; Prodhan, C.; Chaudhuri, T.; Chaudhuri, K.; Mukhopadhyay, C., Pyrrolo[3,4-c]pyridine-Based Fluorescent Chemosensor for Fe3+/Fe2+ Sensitivity and Their Application in Living HepG2 Cells. *ACS Omega* **2018,** *3* (12), 18646-18655.

48. Tan, S. S.; Kim, S. J.; Kool, E. T., Differentiating between Fluorescence-Quenching Metal Ions with Polyfluorophore Sensors Built on a DNA Backbone. *Journal of the American Chemical Society* **2011,** *133* (8), 2664-2671.

49. Chaston, T. B.; Richardson, D. R., Iron chelators for the treatment of iron overload disease: Relationship between structure, redox activity, and toxicity. *American Journal of Hematology* **2003,** *73* (3), 200-210.

50. Jaishankar, M.; Tseten, T.; Anbalagan, N.; Mathew, B. B.; Beeregowda, K. N., Toxicity, mechanism and health effects of some heavy metals. *Interdisciplinary Toxicology* **2014,** *7* (2), 60-72.

51. Ji, W.; Zhu, Z.; Dong, S.; Nie, J.; Du, B., Optical Detection of Fe3+ Ions in Aqueous Solution with High Selectivity and Sensitivity by Using Sulfasalazine Functionalized Microgels. *Sensors* **2019,** *19* (19), 4223.

52. Frackowiak, D., The Jablonski diagram. *Journal of Photochemistry and Photobiology B: Biology* **1988,** *2* (3), 399.

53. Czarnik, A. W., Chemical Communication in Water Using Fluorescent Chemosensors. *Accounts of Chemical Research* **1994,** *27* (10), 302-308.

54. Wu, D.; Sedgwick, A. C.; Gunnlaugsson, T.; Akkaya, E. U.; Yoon, J.; James, T. D., Fluorescent chemosensors: the past, present and future. *Chemical Society Reviews* **2017,** *46* (23), 7105-7123.

55. Valeur, B., Design principles of fluorescent molecular sensors for cation recognition. *Coordination Chemistry Reviews* **2000,** *205* (1), 3-40.

56. M. Costero, A.; Parra, M.; Gil, S.; Gaviña, P., BODIPY Core as Signaling Unit in Chemosensor Design. *BODIPY Dyes - A Privilege Molecular Scaffold with Tunable Properties* **2019**.

57. Afaneh, A. T.; Schreckenbach, G., Fluorescence Enhancement/Quenching Based on Metal Orbital Control: Computational Studies of a 6-Thienyllumazine-Based Mercury Sensor. *The Journal of Physical Chemistry A* **2015,** *119* (29), 8106-8116.

58. Bissell, R. A.; De Silva, A. P.; Gunaratne, H. Q. N.; Lynch, P. L. M.; Maguire, G. E. M.; Sandanayake, K. R. A. S., Molecular fluorescent signalling with 'fluor–spacer–receptor' systems: approaches to sensing and switching devices via supramolecular photophysics. *Chem. Soc. Rev.* **1992,** *21* (3), 187-195.

59. Hariharan, P. C.; Pople, J. A., The influence of polarization functions on molecular orbital hydrogenation energies. *Theoretica Chimica Acta* **1973,** *28* (3), 213-222.

60. De Silva, A., Combining luminescence, coordination and electron transfer for signalling purposes. *Coordination Chemistry Reviews* **2000,** *205* (1), 41-57.

61. Dujols, V.; Ford, F.; Czarnik, A. W., A Long-Wavelength Fluorescent Chemodosimeter Selective for Cu(II) Ion in Water. *Journal of the American Chemical Society* **1997,** *119* (31), 7386-7387.

62. Dodani, S. C.; He, Q.; Chang, C. J., A Turn-On Fluorescent Sensor for Detecting Nickel in Living Cells. *Journal of the American Chemical Society* **2009,** *131* (50), 18020-18021.

63. Rurack, K.; Resch-Genger, U., Rigidization, preorientation and electronic decoupling—the 'magic triangle' for the design of highly efficient fluorescent sensors and switches. *Chemical Society Reviews* **2002,** *31* (2), 116-127.

64. Kim, S. K.; Yoon, J., A new fluorescent PET chemosensor for fluoride ions Dedicated to the memory of D. J. Cram. *Chemical Communications* **2002,** (7), 770-771.

65. De Silva, A. P.; Moody, T. S.; Wright, G. D., Fluorescent PET (Photoinduced Electron Transfer) sensors as potent analytical tools. *The Analyst* **2009,** *134* (12), 2385.

66. Bartwal, G.; Aggarwal, K.; Khurana, J. M., An ampyrone based azo dye as pH-responsive and chemo-reversible colorimetric fluorescent probe for Al3+ in semi-

aqueous medium: implication towards logic gate analysis. *New Journal of Chemistry* **2018,** *42* (3), 2224-2231.

67.	Panja, S. K.;  Dwivedi, N.; Saha, S., Tuning the intramolecular charge transfer (ICT) process in push–pull systems: effect of nitro groups. *RSC Advances* **2016,** *6* (107), 105786-105794.

68.	Grabowski, Z. R.; Dobkowski, J., Twisted intramolecular charge transfer (TICT) excited states: energy and molecular structure. *Pure and Applied Chemistry* **1983,** *55* (2), 245-252.

69.	Marchioro, A.;  Teuscher, J.;  Friedrich, D.;  Kunst, M.;  Van De Krol, R.;  Moehl, T.;  Grätzel, M.; Moser, J.-E., Unravelling the mechanism of photoinduced charge transfer processes in lead iodide perovskite solar cells. *Nature Photonics* **2014,** *8* (3), 250-255.

70.	Sivakumar, R.; Lee, N. Y., Paper-Based Fluorescence Chemosensors for Metal Ion Detection in Biological and Environmental Samples. *BioChip Journal* **2021,** *15* (3), 216-232.

71.	Hirayama, F.; Lipsky, S., Excimer Fluorescence of Benzene and Its Alkyl Derivatives—Concentration and Temperature Dependence. *The Journal of Chemical Physics* **1969,** *51* (5), 1939-1951.

72.	Yip, W. T.; Levy, D. H., Excimer/Exciplex Formation in van der Waals Dimers of Aromatic Molecules. *The Journal of Physical Chemistry* **1996,** *100* (28), 11539-11545.

73.	Feng, X. J.;  Tian, P. Z.;  Xu, Z.;  Chen, S. F.; Wong, M. S., Fluorescence-Enhanced Chemosensor for Metal Cation Detection Based on Pyridine and Carbazole. *The Journal of Organic Chemistry* **2013,** *78* (22), 11318-11325.

74.	Harrop, T. C.; Mascharak, P. K., Fe(III) and Co(III) Centers with Carboxamido Nitrogen and Modified Sulfur Coordination:  Lessons Learned from Nitrile Hydratase. *Accounts of Chemical Research* **2004,** *37* (4), 253-260.

75.	Marlin, D. S.; Mascharak, P. K., Coordination of carboxamido nitrogen to tervalent iron: insight into a new chapter of iron chemistry. *Chemical Society Reviews* **2000,** *29* (1), 69-74.

76.	Marlin, D. S.;  Olmstead, M. M.; Mascharak, P. K., Structure−Spectroscopy Correlation in Distorted Five-Coordinate Cu(II) Complexes:  A Case Study with a Set of Closely Related Copper Complexes of Pyridine-2,6-dicarboxamide Ligands. *Inorganic Chemistry* **2001,** *40* (27), 7003-7008.

77.	Kumar, P.;  Kumar, V.; Gupta, R., Arene-based fluorescent probes for the selective detection of iron. *RSC Advances* **2015,** *5* (118), 97874-97882.

78.	Sudheer;  Kumar, V.;  Kumar, P.; Gupta, R., Detection of Al3+ and Fe3+ ions by nitrobenzoxadiazole bearing pyridine-2,6-dicarboxamide based chemosensors: effect of solvents on detection. *New Journal of Chemistry* **2020,** *44* (31), 13285-13294.

79.	Rahimi, H.;  Hosseinzadeh, R.; Tajbakhsh, M., A new and efficient pyridine-2,6-dicarboxamide-based fluorescent and colorimetric chemosensor for sensitive and selective recognition of Pb2+ and Cu2+. *Journal of Photochemistry & Photobiology, A: Chemistry* **15 February 2021,** *407* (1010-6030).

80.	Teolato, P.;  Rampazzo, E.;  Arduini, M.;  Mancin, F.;  Tecilla, P.; Tonellato, U., Silica Nanoparticles for Fluorescence Sensing of ZnII: Exploring the Covalent Strategy. *Chemistry - A European Journal* **2007,** *13* (8), 2238-2245.

81.     Yantasee, W.; Rutledge, R. D.; Chouyyok, W.; Sukwarotwat, V.; Orr, G.; Warner, C. L.; Warner, M. G.; Fryxell, G. E.; Wiacek, R. J.; Timchalk, C.; Addleman, R. S., Functionalized Nanoporous Silica for the Removal of Heavy Metals from Biological Systems: Adsorption and Application. *ACS Applied Materials & Interfaces* **2010,** *2* (10), 2749-2758.

82.     Košak, A.; Baumana, M.; Padežnik-Gomilšeka, J.; Lobnik, A., Lead (II) complexation with 3-mercaptopropyl-groups in the surface layer of silica nanoparticles: Sorption, kinetics and EXAFS/XANES study. *ScienceDirect: Journal of Molecular Liquids*, **2017**; Vol. 229, pp 371-379.

83.     Makkuni, A.; Bachas, L.; Varma, R.; Sikdar, S.; Bhattacharyya, D., Aqueous and vapor phase mercury sorption by inorganic oxide materials functionalized with thiols and poly-thiols. *Clean Technologies and Environmental Policy* **2005,** *7*, 87-96.

84.     Sousa, K.; Filha, V.; Pinto, V.; Fonseca, M.; Espínola, J.; Arakaki, L., Chemisorption of divalent cations on a silica gel surface modifield with thioglycolic acid: pH influence and ionic strength. *Química Nova* **2007,** *30*, 528-534.

85.     Stöber, W.; Fink, A.; Bohn, E., Controlled growth of monodisperse silica spheres in the micron size range. *Journal of Colloid and Interface Science* **1968,** *26* (1), 62-69.

86.     An, Y.; Chen, M.; Xue, Q.; Liu, W., Preparation and self-assembly of carboxylic acid-functionalized silica. *J Colloid Interface Sci* **2007,** *311* (2), 507-13.

87.     Autry, H. A.; Holcombe, J. A., Cadmium, copper and zinc complexes of poly-L-cysteine. *The Analyst* **1995,** *120* (10), 2643.

88.     Jalilehvand, F.; Mah, V.; Leung, B. O.; Mink, J.; Bernard, G. M.; Hajba, L., Cadmium(II) Cysteine Complexes in the Solid State: A Multispectroscopic Study. *Inorganic Chemistry* **2009,** *48* (9), 4219-4230.

89.     Jun, Y.-W.; Huh, Y.-M.; Choi, J.-S.; Lee, J.-H.; Song, H.-T.; Kim, S.; Yoon, S.; Kim, K.-S.; Shin, J.-S.; Suh, J.-S.; Cheon, J., Nanoscale Size Effect of Magnetic Nanocrystals and Their Utilization for Cancer Diagnosis via Magnetic Resonance Imaging. *Journal of the American Chemical Society* **2005,** *127* (16), 5732-5733.

90.     Yantasee, W.; Warner, C. L.; Sangvanich, T.; Addleman, R. S.; Carter, T. G.; Wiacek, R. J.; Fryxell, G. E.; Timchalk, C.; Warner, M. G., Removal of Heavy Metals from Aqueous Systems with Thiol Functionalized Superparamagnetic Nanoparticles. *Environmental Science & Technology* **2007,** *41* (14), 5114-5119.

91.     Ganapathe, L. S.; Mohamed, M. A.; Mohamad Yunus, R.; Berhanuddin, D. D., Magnetite (Fe3O4) Nanoparticles in Biomedical Application: From Synthesis to Surface Functionalisation. *Magnetochemistry* **2020,** *6* (4), 68.

92.     Rajput, S.; Pittman, C. U.; Mohan, D., Magnetic magnetite (Fe3O4) nanoparticle synthesis and applications for lead (Pb2+) and chromium (Cr6+) removal from water. *Journal of Colloid and Interface Science* **2016,** *468*, 334-346.

93.     Chen, K.; Zhang, Z.; Xia, K.; Zhou, X.; Guo, Y.; Huang, T., Facile Synthesis of Thiol-Functionalized Magnetic Activated Carbon and Application for the Removal of Mercury(II) from Aqueous Solution. *ACS Omega* **2019,** *4* (5), 8568-8579.

94.     Damiri, F.; Bachra, Y.; Grouli, A.; Ouaket, A.; Bennamara, A.; Knouzi, N.; Berrada, M., A Novel Drug Delivery System Based on Nanoparticles of Magnetite Fe3O4 Embedded in an Auto Cross-Linked Chitosan. **2020**; pp 1-24.

95.     Sun, S.-N.; Wei, C.; Zhu, Z.-Z.; Hou, Y.-L.; Venkatraman, S. S.; Xu, Z.-C., Magnetic iron oxide nanoparticles: Synthesis and surface coating techniques for biomedical applications. *Chinese Physics B* **2014,** *23* (3), 037503.

96.     Sun, S.; Zeng, H., Size-controlled synthesis of magnetite nanoparticles. *J Am Chem Soc* **2002,** *124* (28), 8204-5.

97.     Urbina, M. C.; Zinoveva, S.; Miller, T.; Sabliov, C. M.; Monroe, W. T.; Kumar, C. S. S. R., Investigation of Magnetic Nanoparticle−Polymer Composites for Multiple-controlled Drug Delivery. *The Journal of Physical Chemistry C* **2008,** *112* (30), 11102-11108.

98.     Guo, Y.; Wang, Z.; Shao, H.; Jiang, X., Hydrothermal synthesis of highly fluorescent carbon nanoparticles from sodium citrate and their use for the detection of mercury ions. *Carbon* **2013,** *52*, 583-589.

99.     Ek, S.; Root, A.; Peussa, M.; Niinistö, L., Determination of the Hydroxyl Group Content in Silica by Thermogravimetry and a Comparison with 1H MAS NMR Results. *Thermochimica Acta* **2001,** *379*, 201-212.

100.    Houari, B.; Louhibi, S.; Tizaoui, K.; Boukli-Hacene, L.; Benguella, B.; Roisnel, T.; Dorcet, V., New synthetic material removing heavy metals from aqueous solutions and wastewater. *Arabian Journal of Chemistry* **2019,** *12* (8), 5040-5048.

101.    Pohl, A., Removal of Heavy Metal Ions from Water and Wastewaters by Sulfur-Containing Precipitation Agents. *Water, Air, & Soil Pollution* **2020,** *231* (10).

102.    Leininger, S.; Olenyuk, B.; Stang, P. J., Self-Assembly of Discrete Cyclic Nanostructures Mediated by Transition Metals. *Chemical Reviews* **2000,** *100* (3), 853-908.

103.    Moulton, B.; Zaworotko, M. J., From Molecules to Crystal Engineering: Supramolecular Isomerism and Polymorphism in Network Solids. *Chemical Reviews* **2001,** *101* (6), 1629-1658.

104.    Harrison, P. G., Elements of group 4. *Coordination Chemistry Reviews* **1986,** *75*, 200-296.

105.    Wächtler, E.; Gericke, R.; Kutter, S.; Brendler, E.; Wagler, J., Molecular structures of pyridinethiolato complexes of Sn(II), Sn(IV), Ge(IV), and Si(IV). *Main Group Metal Chemistry* **2013,** *36* (5-6).

106.    Pedrido, R.; González-Noya, A. M.; Romero, M. J.; Martínez-Calvo, M.; Vázquez López, M.; Gómez-Fórneas, E.; Zaragoza, G.; Bermejo, M. R., Pentadentate thiosemicarbazones as versatile chelating systems. A comparative structural study of their metallic complexes. *Dalton Transactions* **2008,** (47), 6776.

107.    Pedrido, R.; Bermejo, M. R.; Romero, M. J.; Vázquez, M.; González-Noya, A. M.; Maneiro, M.; Rodríguez, M. J.; Fernández, M. I., Syntheses and X-ray characterization of metal complexes with the pentadentate thiosemicarbazone ligand bis(4-N-methylthiosemicarbazone)-2,6-diacetylpyridine. The first pentacoordinate lead(ii) complex with a pentagonal geometry. *Dalton Trans.* **2005,** (3), 572-579.

108.    Hii, K. K.; Kee, T. P., Chapter 6. Nitrogen, phosphorus, arsenic, antimony, and bismuth. *Annual Reports Section "A" (Inorganic Chemistry)* **1994,** *91*, 67.

109.    Alhazmi, H., FT-IR Spectroscopy for the Identification of Binding Sites and Measurements of the Binding Interactions of Important Metal Ions with Bovine Serum Albumin. *Scientia Pharmaceutica* **2019,** *87* (1), 5.

110.    Zaman, K. M.; Blue, L. Y.; Huggins, F. E.; Atwood, D. A., Cd, Hg, and Pb Compounds of Benzene-1,3-diamidoethanethiol (BDETH2). *Inorganic Chemistry* **2007,** *46* (6), 1975-1980.

111.    Kumar, P.; Gupta, R., The wonderful world of pyridine-2,6-dicarboxamide based scaffolds. *Dalton Transactions* **2016,** *45* (47), 18769-18783.

112.    Leung, W.-H.; Ma, J.-X.; Yam, V. W.-W.; Che, C.-M.; Poon, C.-K., Syntheses, electrochemistry and reactivities of pyridine amide complexes of chromium(III) and manganese(III). *Journal of the Chemical Society, Dalton Transactions* **1991,** (4), 1071.

113.    Chmielewski, M. J.; Jurczak, J., Anion Recognition by Neutral Macrocyclic Amides. *Chemistry - A European Journal* **2005,** *11* (20), 6080-6094.

114.    Malone, J. F.; Murray, C. M.; Dolan, G. M.; Docherty, R.; Lavery, A. J., Intermolecular Interactions in the Crystal Chemistry of N,N'-Diphenylisophthalamide, Pyridine-2,6-dicarboxylic Acid Bisphenylamide, and Related Compounds. *Chemistry of Materials* **1997,** *9* (12), 2983-2989.

115.    Graphical Abstract(Angew. Chem. Int. Ed. Engl. 6/1992). *Angewandte Chemie International Edition in English* **1992,** *31* (6), NA-NA.

116.    Parkin, S. R., Practical hints and tips for solution of pseudo-merohedric twins: three case studies. *Acta Crystallographica Section E Crystallographic Communications* **2021,** *77* (5), 452-465.

117.    Frisch, M. J.; Trucks, G. W.; Schlegel, H. B.; Scuseria, G. E.; Robb, M. A.; Cheeseman, J. R.; Scalmani, G.; Barone, V.; Petersson, G. A.; Nakatsuji, H.; Li, X.; Caricato, M.; Marenich, A. V.; Bloino, J.; Janesko, B. G.; Gomperts, R.; Mennucci, B.; Hratchian, H. P.; Ortiz, J. V.; Izmaylov, A. F.; Sonnenberg, J. L.; Williams; Ding, F.; Lipparini, F.; Egidi, F.; Goings, J.; Peng, B.; Petrone, A.; Henderson, T.; Ranasinghe, D.; Zakrzewski, V. G.; Gao, J.; Rega, N.; Zheng, G.; Liang, W.; Hada, M.; Ehara, M.; Toyota, K.; Fukuda, R.; Hasegawa, J.; Ishida, M.; Nakajima, T.; Honda, Y.; Kitao, O.; Nakai, H.; Vreven, T.; Throssell, K.; Montgomery Jr., J. A.; Peralta, J. E.; Ogliaro, F.; Bearpark, M. J.; Heyd, J. J.; Brothers, E. N.; Kudin, K. N.; Staroverov, V. N.; Keith, T. A.; Kobayashi, R.; Normand, J.; Raghavachari, K.; Rendell, A. P.; Burant, J. C.; Iyengar, S. S.; Tomasi, J.; Cossi, M.; Millam, J. M.; Klene, M.; Adamo, C.; Cammi, R.; Ochterski, J. W.; Martin, R. L.; Morokuma, K.; Farkas, O.; Foresman, J. B.; Fox, D. J. *Gaussian 16 Rev. C.01*, Wallingford, CT, 2016.

118.    Chai, J.-D.; Head-Gordon, M., Long-range corrected hybrid density functionals with damped atom–atom dispersion corrections. *Physical Chemistry Chemical Physics* **2008,** *10* (44), 6615.

119.    Petersson, G. A.; Bennett, A.; Tensfeldt, T. G.; Al-Laham, M. A.; Shirley, W. A.; Mantzaris, J., A complete basis set model chemistry. I. The total energies of closed-shell atoms and hydrides of the first-row elements. *The Journal of Chemical Physics* **1988,** *89* (4), 2193-2218.

120.    Petersson, G. A.; Al-Laham, M. A., A complete basis set model chemistry. II. Open-shell systems and the total energies of the first-row atoms. *The Journal of Chemical Physics* **1991,** *94* (9), 6081-6090.

121.    Marenich, A. V.; Cramer, C. J.; Truhlar, D. G., Universal Solvation Model Based on Solute Electron Density and on a Continuum Model of the Solvent Defined by the Bulk Dielectric Constant and Atomic Surface Tensions. *The Journal of Physical Chemistry B* **2009,** *113* (18), 6378-6396.

122.     Pereyaslavets, L.; Kamath, G.; Butin, O.; Illarionov, A.; Olevanov, M.; Kurnikov, I.; Sakipov, S.; Leontyev, I.; Voronina, E.; Gannon, T.; Nawrocki, G.; Darkhovskiy, M.; Ivahnenko, I.; Kostikov, A.; Scaranto, J.; Kurnikova, M. G.; Banik, S.; Chan, H.; Sternberg, M. G.; Sankaranarayanan, S. K. R. S.; Crawford, B.; Potoff, J.; Levitt, M.; Kornberg, R. D.; Fain, B., Accurate determination of solvation free energies of neutral organic compounds from first principles. *Nature Communications* **2022,** *13* (1).

123.     Dennington, R.; Keith, T. A.; Millam, J. M., GaussView, Version 5.0.9. Semichem Inc.: *Shawnee Mission: KS*, **2009**.

124.     Nafees, M.; Ikram, M.; Ali, S., Thermal stability of lead sulfide and lead oxide nano-crystalline materials. *Applied Nanoscience* **2017,** *7* (7), 399-406.

125.     Pedrido, R.; Romero, M. J.; Bermejo, M. R.; González-Noya, A. M.; García-Lema, I.; Zaragoza, G., Metal-Catalysed Oxidation Processes in Thiosemicarbazones: New Complexes with the LigandN-{2-([4-N-Ethylthiosemicarbazone]methyl)phenyl}-p-toluenesulfonamide. *Chemistry - A European Journal* **2008,** *14* (2), 500-512.

126.     Pedrido, R.; Romero, M. J.; Bermejo, M. R.; González-Noya, A. M.; Maneiro, M.; Rodríguez, M. J.; Zaragoza, G., Influence of the metal size in the structure of the complexes derived from a pentadentate [N3O2] hydrazone. *Dalton Trans.* **2006,** (44), 5304-5314.

127.     Gryko, D. T.; Pęcak, A.; Koźmiński, W.; Piątek, P.; Jurczak, J., 1H, 13C, 15N NMR and X-Ray Diffractometry in Structural Studies of Macrocyclic Lactams Containing Pyridine Moiety. *Supramolecular Chemistry* **2000,** *12* (2), 229-235.

128.     Wagner-Wysiecka, E.; Łukasik, N.; Okuniewski, A.; Galiński, B., Ion recognition properties of new pyridine-2,6-dicarboxamide bearing propeller-like pendant residues: multi-spectroscopic approach. *Monatshefte für Chemie - Chemical Monthly* **2020,** *151* (3), 331-343.

129.     Payne, J. C.; Ter Horst, M. A.; Godwin, H. A., Lead Fingers:  Pb2+ Binding to Structural Zinc-Binding Domains Determined Directly by Monitoring Lead−Thiolate Charge-Transfer Bands. *J. Am. Chem. Soc.* **1999,** *121* (29), 6850-6855.

130.     Magyar, J. S.; Weng, T.-C.; Stern, C. M.; Dye, D. F.; Rous, B. W.; Payne, J. C.; Bridgewater, B. M.; Mijovilovich, A.; Parkin, G.; Zaleski, J. M.; Penner-Hahn, J. E.; Godwin, H. A., Reexamination of Lead(II) Coordination Preferences in Sulfur-Rich Sites: Implications for a Critical Mechanism of Lead Poisoning. *Journal of the American Chemical Society* **2005,** *127* (26), 9495-9505.

131.     Mah, V.; Jalilehvand, F., Lead(II) Complex Formation with Glutathione. *Inorganic Chemistry* **2012,** *51* (11), 6285-6298.

132.     Pyykko, P., Relativistic effects in structural chemistry. *Chemical Reviews* **1988,** *88* (3), 563-594.

133.     Liu, Z.-C.; Yang, Z.-Y.; Li, T.-R.; Wang, B.-D.; Li, Y.; Qin, D.-D.; Wang, M.-F.; Yan, M.-H., An effective Cu(ii) quenching fluorescence sensor in aqueous solution and 1D chain coordination polymer framework. *Dalton Transactions* **2011,** *40* (37), 9370.

134.     Thakur, A.; Patwa, J.; Pant, S.; Sharma, A.; Flora, S. J. S., Interaction study of monoisoamyl dimercaptosuccinic acid with bovine serum albumin using biophysical and molecular docking approaches. *Scientific Reports* **2021,** *11* (1).

135.    Hu, J.;  Zhang, D.; Harris, F. W., Ruthenium(III) Chloride Catalyzed Oxidation of Pyrene and 2,7-Disubstitued Pyrenes:  An Efficient, One-Step Synthesis of Pyrene-4,5-diones and Pyrene-4,5,9,10-tetraones. *The Journal of Organic Chemistry* **2005,** *70* (2), 707-708.

136.    Wang, X.;  Qin, C.;  Wang, E.;  Li, Y.;  Hao, N.;  Hu, C.; Xu, L., Syntheses, Structures, and Photoluminescence of a Novel Class of d10Metal Complexes Constructed from Pyridine-3,4-dicarboxylic Acid with Different Coordination Architectures. *Inorganic Chemistry* **2004,** *43* (6), 1850-1856.

137.    Kumar, P.;  Kumar, V.;  Pandey, S.; Gupta, R., Detection of sulfide ion and gaseous H2S using a series of pyridine-2,6-dicarboxamide based scaffolds. *Dalton Transactions* **2018,** *47* (28), 9536-9545.

138.    Geng, T.-M.;  Guo, C.;  Dong, Y.-J.;  Chen, M.; Wang, Y., Turn-on fluorogenic and chromogenic detection of cations in complete water media with poly(N-vinyl pyrrolidone) bearing rhodamine B derivatives as polymeric chemosensor. *Polymers for Advanced Technologies* **2016,** *27* (1), 90-97.

139.    Zhang, Y.;  Ye, A.;  Yao, Y.; Yao, C., A Sensitive Near-Infrared Fluorescent Probe for Detecting Heavy Metal Ag+ in Water Samples. *Sensors* **2019,** *19* (2), 247.

140.    Teale, F. W. J.; Weber, G., Ultraviolet fluorescence of the aromatic amino acids. *Biochemical Journal* **1957,** *65* (3), 476-482.

141.    Formica, M.;  Fusi, V.;  Giorgi, L.; Micheloni, M., New fluorescent chemosensors for metal ions in solution. *Coordination Chemistry Reviews* **2012,** *256* (1-2), 170-192.

142.    Manyangadze, M.;  Chikuruwo, N. H. M.;  Narsaiah, T. B.;  Chakra, C. S.;  Radhakumari, M.; Danha, G., Enhancing adsorption capacity of nano-adsorbents via surface modification: A review. *South African Journal of Chemical Engineering* **2020,** *31*, 25-32.

143.    Zou, W.;  Filatov, M.;  Atwood, D.; Cremer, D., Removal of Mercury from the Environment: A Quantum-Chemical Study with the Normalized Elimination of the Small Component Method. *Inorganic Chemistry* **2013,** *52* (5), 2497-2504.

144.    Laurent, S.;  Forge, D.;  Port, M.;  Roch, A.;  Robic, C.;  Vander Elst, L.; Muller, R. N., Magnetic Iron Oxide Nanoparticles: Synthesis, Stabilization, Vectorization, Physicochemical Characterizations, and Biological Applications. *Chemical Reviews* **2008,** *108* (6), 2064-2110.

145.    Atta, A.;  Al-Lohedan, H.; Al-Hussain, S., Functionalization of Magnetite Nanoparticles as  Oil Spill Collector. *International Journal of Molecular Sciences* **2015,** *16* (12), 6911-6931.

146.    Wu, W.;  He, Q.; Jiang, C., Magnetic Iron Oxide Nanoparticles: Synthesis and Surface Functionalization Strategies. *Nanoscale Research Letters* **2008,** *3* (11), 397-415.

147.    Ek, S.;  Iiskola, E. I.;  Niinistö, L., Gas-Phase Deposition of Aminopropylalkoxysilanes on Porous Silica. *Langmuir* **2003,** *19* (8), 3461-3471.

148.    Pasternack, R. M.;  Rivillon Amy, S.; Chabal, Y. J., Attachment of 3-(Aminopropyl)triethoxysilane on Silicon Oxide Surfaces: Dependence on Solution Temperature. *Langmuir* **2008,** *24* (22), 12963-12971.

149.    Ling, D.;  Lee, N.; Hyeon, T., Chemical Synthesis and Assembly of Uniformly Sized Iron Oxide Nanoparticles for Medical Applications. *Accounts of Chemical Research* **2015,** *48* (5), 1276-1285.

150.    Mahmoudi, M.; Hofmann, H.; Rothen-Rutishauser, B.; Petri-Fink, A., Assessing the In Vitro and In Vivo Toxicity of Superparamagnetic Iron Oxide Nanoparticles. *Chemical Reviews* **2012,** *112* (4), 2323-2338.

151.    Fato, F. P.; Li, D.-W.; Zhao, L.-J.; Qiu, K.; Long, Y.-T., Simultaneous Removal of Multiple Heavy Metal Ions from River Water Using Ultrafine Mesoporous Magnetite Nanoparticles. *ACS Omega* **2019,** *4* (4), 7543-7549.

152.    Venkateswarlu, S.; Yoon, M., Rapid removal of cadmium ions using green-synthesized Fe3O4 nanoparticles capped with diethyl-4-(4 amino-5-mercapto-4H-1,2,4-triazol-3-yl)phenyl phosphonate. *RSC Advances* **2015,** *5* (80), 65444-65453.

153.    Giraldo, L.; Erto, A.; Moreno-Piraján, J. C., Magnetite nanoparticles for removal of heavy metals from aqueous solutions: synthesis and characterization. *Adsorption* **2013,** *19* (2-4), 465-474.

154.    Ma, W.; Ebadi, A. G.; Sabil, M. S.; Javahershenas, R.; Jimenez, G., One-pot synthesis of 2-amino-4H-chromene derivatives by MNPs@Cu as an effective and reusable magnetic nanocatalyst. *RSC Advances* **2019,** *9* (23), 12801-12812.

155.    Du, X.; He, J., Amino-functionalized silicananoparticles with center-radially hierarchical mesopores as ideal catalyst carriers. *Nanoscale* **2012,** *4* (3), 852-859.

156.    Lebeau, B.; Galarneau, A.; Linden, M., Introduction for 20 years of research on ordered mesoporous materials. *Chemical Society Reviews* **2013,** *42* (9), 3661.

157.    Kresge, C. T.; Roth, W. J., The discovery of mesoporous molecular sieves from the twenty year perspective. *Chemical Society Reviews* **2013,** *42* (9), 3663.

158.    Fryxell, G. E.; Lin, Y.; Fiskum, S.; Birnbaum, J. C.; Wu, H.; Kemner, K.; Kelly, S., Actinide Sequestration Using Self-Assembled Monolayers on Mesoporous Supports. *Environmental Science & Technology* **2005,** *39* (5), 1324-1331.

159.    Schubert, J., Chelating Agents in Biological Systems. **1981,** *40*, 227.

160.    Crisponi, G.; Diaz, A.; Nurchi, V. M.; Pivetta, T.; Tapia Estévez, M. A. J., Equilibrium study on Cd(II) and Zn(II) chelates of mercapto carboxylic acids. *Polyhedron* **2002,** *21* (14-15), 1319-1327.

161.    Palin, D.; Rufato, K. B.; Linde, G. A.; Colauto, N. B.; Caetano, J.; Alberton, O.; Jesus, D. A.; Dragunski, D. C., Evaluation of Pb (II) biosorption utilizing sugarcane bagasse colonized by Basidiomycetes. *Environmental Monitoring and Assessment* **2016,** *188* (5).

162.    Block, E.; Gernon, M.; Kang, H.; Ofori-Okai, G.; Zubieta, J., Coordination chemistry of sterically hindered thiolate ligands. Preparation and structural characterization of the oligomeric homoleptic complexes [o-trimethylsilylbenzenethiolato]copper dodecamer and [o-trimethylsilylbenzenethiolato]silver octamer and a. *Inorganic Chemistry* **1989,** *28* (7), 1263-1271.

163.    Langmuir, I., THE ADSORPTION OF GASES ON PLANE SURFACES OF GLASS, MICA AND PLATINUM. *Journal of the American Chemical Society* **1918,** *40* (9), 1361-1403.

164.    Lipscomb, W. N.; Sträter, N., Recent Advances in Zinc Enzymology. *Chemical Reviews* **1996,** *96* (7), 2375-2434.

VITA

**Education:**

B.Sc. Chemistry: University of Peradeniya, Sri Lanka, 2010- 2014

**Scholastic and professional honors:**

Outstanding Graduate Teaching Assistant 2021, Outstanding graduate teaching assistant award in excellence in teaching.

Max Steckler Fellowship 2018, Outstanding Oral Qualifier award for the performance in the oral qualification exam

**Professional publications:**

Bandara, S.N.; Moore M.; Parkin S; Atwood D.A.;" PB9 Synthetic Pyridine Thiol PB9 for Pb(II) Removal from Water*", Inorganic Chemistry, (manuscript near submission)*

Bandara, S.N.; Moore M.; Parkin S; Atwood D.A.;" *Pyridine- Functionalized PB9 as Sensitive and Selective Fluorescent Sensors for $Fe^{3+}$ ion, (manuscript near submission)*

Bandara, H.K.M.S.N., Perera, A.D.L.C.; Kottegoda, N.; *"Preliminary study on the use of activated coconut coir as an adsorbent for $Cl^-$ and $F^-$ Proceedings of the Peradeniya University International Research Sessions, Sri Lanka".* IPURSE 2015/2016

Shashika Nadishani Bandara